NASA Technical Memorandum 4516

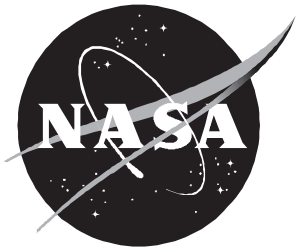

Piloted Simulation Study of an ILS Approach of a Twin-Pusher Business/Commuter Turboprop Aircraft Configuration

Donald R. Riley, Jay M. Brandon, and Louis J. Glaab

January 1994

NASA Technical Memorandum 4516

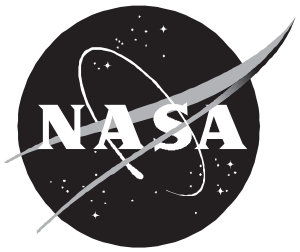

Piloted Simulation Study of an ILS Approach of a Twin-Pusher Business/Commuter Turboprop Aircraft Configuration

Donald R. Riley and Jay M. Brandon
Langley Research Center • Hampton, Virginia

Louis J. Glaab
Lockheed Engineering & Sciences Company • Hampton, Virginia

National Aeronautics and Space Administration
Langley Research Center • Hampton, Virginia 23681-0001

January 1994

Summary

A six-degree-of-freedom nonlinear simulation of a twin-pusher turboprop business/commuter aircraft configuration representative of the Cessna ATPTB (Advanced Turboprop Test Bed) was developed for use in piloted studies and then used for examining the performance and handling qualities during an ILS (instrument landing system) approach and missed-approach task with the Langley General Aviation Simulator. Simulation predictions over a reasonable portion of the aircraft flight envelope were compared with flight test data obtained by the Cessna Aircraft Company for simulation validation. Six test subjects consisting of two research pilots, the principal ATPTB company test pilot, and three general aviation pilots participated in the study. Simulation flights were performed in the presence of moderate turbulence, varying horizontal winds, and engine-out conditions. Results of the study indicated successful ILS approaches and missed-approach maneuvers were performed by each of the 6 pilots for the 16 different test conditions presented. All pilots commented on the difficulty of the high workload task, which was compounded by the presence of pitch coupling with power because of the high engine location and by the low directional damping of the configuration. The vehicle was considered to be in the certifiable range under the present Federal Air Regulations.

Introduction

Recently, industry has shown considerable interest in applying the advanced turboprop technology developed for commercial airline aircraft to general aviation business/commuter aircraft. Consequently, NASA has developed a research program to examine various aspects of this potential application. In support of this effort, a cooperative program was initiated between NASA and the Cessna Aircraft Company in which NASA developed a piloted simulation of a turboprop aircraft modeled after the Cessna ATPTB (Advanced Turboprop Test Bed). The purpose of this study was twofold: first, to generate a viable math model applicable over the flight envelope of the ATPTB aircraft for use in this study as well as future studies, and second, to examine the handling qualities of the configuration during an approach-to-landing task. To validate the math modeling, simulation results were compared with measured flight data. To study the handling qualities, an instrument landing system (ILS) approach and missed approach were performed in the presence of moderate turbulence, varying horizontal winds, and engine-out conditions. This simulation permitted examining vehicle flying characteristics under adverse weather conditions for which flight operations of this one-of-a-kind test-bed aircraft were not permitted by the company. This paper presents the math model and associated information, the ILS task performance results, and the pilots' evaluations of the handling qualities of the simulated aircraft. Simulation results are compared with Cessna flight test measurements in appendix A.

Background

The increasing congestion at the metropolitan hub airports of the major airlines has generated considerable interest in the aviation community in the possible use of small business/commuter aircraft as a means to alleviate congestion and provide greater flexibility for the airline traveler to reach smaller regional airports. (See ref. 1.) The use of turboprop power units for business/commuter aircraft reflects the desire to exploit the advanced turboprop technology of increased fuel efficiency and performance gains developed for larger airline aircraft. (See refs. 2–4.) Toward this end, studies of possible aircraft designs have examined different airplane component arrangements, such as aft-mounted tractor or pusher engine arrangements, engines located over the wings, engines located over the horizontal tail, and three surface arrangements. (See refs. 5–13.) Also, several flight vehicles have been built to verify the benefits associated with the unconventional designs. The Cessna Aircraft Company constructed the ATPTB aircraft for such a purpose. The configuration with its aft-fuselage-mounted turbine engines and pusher propellers has served as a baseline for a number of wind tunnel studies, which generated a database sufficient to permit a simulator math model to be developed.

Acknowledgment

The authors are indebted to the Cessna Aircraft Company, a number of its personnel, the two NASA research pilots, and the simulator support employees of The Unisys Corporation without whose efforts and assistance this study could not have been undertaken.

Nomenclature

Moment data are referred to a center of gravity (c.g.) located in the plane of symmetry and positioned longitudinally at 25 percent of the wing mean aerodynamic chord. Transfer equations were used to shift the c.g. to new longitudinal locations. The body-axis system shown in figure 1 was used for motion calculations.

a_Z	acceleration along Z body axis due to combined aerodynamic and propeller forces, ft/sec^2 (see appendix C)
B	compressibility factor, $\sqrt{1-M^2}$
b	wingspan, ft
$C_{D,s}$	stability-axis drag coefficient, $\frac{-F_{X,s}}{q_\infty S_w}$
C_h	hinge-moment coefficient
$C_{L,\max}$	maximum lift coefficient
$C_{L,s}$	lift coefficient, $\frac{-F_{Z,s}}{q_\infty S_w}$
$C_{l,b}$	rolling-moment coefficient, about X_B, $\frac{L_b}{q_\infty S_w b}$
$C_{m,b}$	pitching-moment coefficient, about Y_B, $\frac{M_b}{q_\infty S_w \bar{c}_w}$
$C_{n,b}$	yawing-moment coefficient, about Z_B, $\frac{N_b}{q_\infty S_w b}$
C_T	thrust coefficient, $\frac{T}{q_\infty S_w}$
$C_{Y,s}$	stability-axis side-force coefficient, $\frac{F_{Y,s}}{q_\infty S_w}$
$\bar{c}$	aerodynamic reference chord, ft
$\bar{c}_w$	wing mean aerodynamic chord, ft
E_h	declination angle from vehicle altitude at middle marker to runway threshold, deg
F_c	column force required for elevator deflection, pull force positive, lb
F_p	rudder pedal force, positive when right pedal depressed, lb
F_w	wheel force required at rim for aileron deflection, positive clockwise, lb
$F_{X,b}$, $F_{Y,b}$, $F_{Z,b}$	combined aerodynamic and propulsive force along body axes, respectively, lb
$F_{X,s}$, $F_{Y,s}$, $F_{Z,s}$	combined aerodynamic and propulsive forces along stability axes, respectively, lb
G	control surface gearing ratio, 1/ft
g	gravitational constant, 32.17 ft/sec^2
h	altitude, ft
I_P	moment of inertia of propeller, gear box, and engine rotating components about axis of rotation, slug-ft^2
I_X, I_Y, I_Z	moments of inertia about body axes, slug-ft^2
I_{XZ}	body-axis product of inertia, slug-ft^2
i_t	horizontal-tail incidence angle, deg
KDP, KDT	gain in directional control system for pilot and for trim
KLP, KLT	gain in longitudinal control system for pilot and for trim
KLATP, KLATT	gain in lateral control system for pilot and for trim
L_b, M_b, N_b	combined aerodynamic and propulsive moments about body axes, respectively, ft-lb
L_α	$= \frac{q_\infty S_w}{mV} C_{L_\alpha}$
M	Mach number
m	vehicle mass, slugs
N	engine speed, rpm
n	load factor, g units
n_{LE}, n_{RE}	propeller rotational speed of left and right power units, rps
p, q, r	rolling, pitching, and yawing angular velocity about body axes, deg/sec or rad/sec
Q	engine torque, ft-lb
q_∞	dynamic pressure, $\frac{1}{2}\rho V^2$, lb/ft^2
rms( )	root mean square value of quantity computed for trajectory portion between outer and middle markers
S	surface area, ft^2
S_w	wing area, ft^2
s	Laplace variable

s^*	unbiased estimate of standard deviation
T	thrust from a single-turbine-engine and propeller combination, lb
t	time, sec
u, v, w	velocity components along body axes, ft/sec
V	velocity, ft/sec
W	weight, lb
X_B, Y_B, Z_B	Cartesian coordinate system of body axes with origin located at vehicle center of gravity
X_E, Y_E, Z_E	Earth-fixed axis system with origin positioned at runway threshold on centerline (positive X_E direction is along runway)
X_S, Y_S, Z_S	stability axes with origin at vehicle c.g.
x_E, y_E, z_E	displacements of vehicle c.g. from runway threshold measured in Earth-fixed axes
y_e, z_e	right engine thrust axis displacements along body axes
a	angle of attack relative to airplane longitudinal axis, deg or rad
β	angle of sideslip, deg
γ	flight path angle, deg
ΔC_D ΔC_L ΔC_l ΔC_m ΔC_n ΔC_y	induced effect due to power of a single-turbine-engine and propeller combination
$\Delta\varepsilon$	tracking error about glideslope centerline, $\left[\tan^{-1}\left(\frac{h}{1000-x_E}\right) - 3°\right]$, deg
$\Delta\sigma$	tracking error about localizer centerline, $\left[\tan^{-1}\left(\frac{y_E}{11\,000-x_E}\right)\right]$, deg
δ_a	total aileron deflection $\left(\frac{\delta_{a,R}-\delta_{a,L}}{2}\right)$, deg
$\delta_{a,L}$	left aileron deflection, positive trailing edge down, deg
$\delta_{a,R}$	right aileron deflection, positive trailing edge down, deg
δ_c	pilot's control column deflection, in.
δ_e	elevator deflection, positive trailing edge down, deg
δ_f	flap deflection, positive trailing edge down, deg
δ_{LG}	landing gear deflection, 0 is retracted, 1 is fully extended
δ_P	cockpit rpm lever position
δ_r	rudder deflection, positive trailing edge left, deg
δ_{rp}	pilot's rudder pedal deflection, in.
δ_{SB}	speed brake deflection, 0 is closed, 1 is fully deflected
δ_T	cockpit throttle lever position
δ_w	pilot's control wheel deflection, deg
ζ	damping ratio
ρ	mass density of air, slugs/ft^3
$\tau_1, \tau_2, \tau_3, \tau_4$	engine-model time constants, sec
τ_f	flap time constant, sec
τ_{LG}	landing-gear time constant, sec
τ_r	roll-mode time constant, sec
τ_{SB}	speed-brake time constant, sec
τ_s	spiral-mode time constant, sec
ψ, θ, ϕ	Euler angles (yaw, pitch, and roll angles, respectively), deg or rad
ω_n	undamped natural frequency, rad/sec

Derivatives:

$$C_{D_{\delta_e}} = \frac{\partial C_{D,s}}{\partial \delta_e} \qquad C_{L_{\delta_e}} = \frac{\partial C_{L,s}}{\partial \delta_e} \qquad C_{m_{\delta_e}} = \frac{\partial C_{m,b}}{\partial \delta_e}$$

$$C_{D_{\delta_f}} = \frac{\partial C_{D,s}}{\partial \delta_f} \qquad C_{L_{\delta_f}} = \frac{\partial C_{L,s}}{\partial \delta_f} \qquad C_{m_{\delta_f}} = \frac{\partial C_{m,b}}{\partial \delta_f}$$

$$C_{D_{i_t}} = \frac{\partial C_{D,s}}{\partial_{i_t}} \qquad C_{L_{i_t}} = \frac{\partial C_{L,s}}{\partial_{i_t}} \qquad C_{m_{i_t}} = \frac{\partial C_{m,b}}{\partial_{i_t}}$$

$$C_{D_q} = \frac{\partial C_{D,s}}{\partial \frac{q\bar{c}_w}{2V}} \qquad C_{L_q} = \frac{\partial C_{L,s}}{\partial \frac{q\bar{c}_w}{2V}} \qquad C_{m_q} = \frac{\partial C_{m,b}}{\partial \frac{q\bar{c}_w}{2V}}$$

$$C_{D_{\dot{\alpha}}} = \frac{\partial C_{D,s}}{\partial \frac{\dot{\alpha}\bar{c}_w}{2V}} \qquad C_{L_{\dot{\alpha}}} = \frac{\partial C_{L,s}}{\partial \frac{\dot{\alpha}\bar{c}_w}{2V}} \qquad C_{m_{\dot{\alpha}}} = \frac{\partial C_{m,b}}{\partial \frac{\dot{\alpha}\bar{c}_w}{2V}}$$

$$C_{D_{\delta_r}} = \frac{\partial C_{D,s}}{\partial |\delta_r|} \qquad C_{L_\alpha} = \frac{\partial C_{L,s}}{\partial \alpha} \qquad C_{m_\alpha} = \frac{\partial C_{m,b}}{\partial \alpha}$$

$$C_{Y_\beta} = \frac{\partial C_{Y,s}}{\partial \beta} \qquad C_{l_\beta} = \frac{\partial C_{l,b}}{\partial \beta} \qquad C_{n_\beta} = \frac{\partial C_{n,b}}{\partial \beta}$$

$$C_{Y_{\delta_r}} = \frac{\partial C_{Y,s}}{\partial \delta_r} \qquad C_{l_{\delta_r}} = \frac{\partial C_{l,b}}{\partial \delta_r} \qquad C_{n_{\delta_r}} = \frac{\partial C_{n,b}}{\partial \delta_r}$$

$$C_{Y_{\delta_a}} = \frac{\partial C_{Y,s}}{\partial \delta_a} \qquad C_{l_{\delta_a}} = \frac{\partial C_{l,b}}{\partial \delta_a} \qquad C_{n_{\delta_a}} = \frac{\partial C_{n,b}}{\partial \delta_a}$$

$$C_{Y_p} = \frac{\partial C_{Y,s}}{\partial \frac{pb}{2V}} \qquad C_{l_p} = \frac{\partial C_{l,b}}{\partial \frac{pb}{2V}} \qquad C_{n_p} = \frac{\partial C_{n,b}}{\partial \frac{pb}{2V}}$$

$$C_{Y_r} = \frac{\partial C_{Y,s}}{\partial \frac{rb}{2V}} \qquad C_{l_r} = \frac{\partial C_{l,b}}{\partial \frac{rb}{2V}} \qquad C_{n_r} = \frac{\partial C_{n,b}}{\partial \frac{rb}{2V}}$$

Subscripts:

a	aileron
b	body axis
c	column
dyn	dynamic
e	elevators
f	flap
GE	ground effect
LE	left engine
max	maximum
NE	no engine, propeller off
o	conditions where $\delta_{a,L} = \delta_{a,R} = \delta_e = \delta_r = 0°$ and $\beta = 0°$
RE	right engine
r	rudder
s	stability axis
st	static
w	wing

Abbreviations:

AGL	above ground level
ATPTB	Advanced Turboprop Test Bed
CAS	calibrated airspeed, knots
c.g.	center of gravity
DME	distance-measuring equipment
DOF	degrees of freedom
FAR's	Federal Air Regulations
FIATI	aileron scaling function
IAF	initial approach fix
IAS	indicated airspeed
IFR	instrument flight rules
ILS	instrument landing system
INT	intersection
KNUTS	intersection of VORTAC radial with localizer
LG	landing gear
LOM	locator outer marker (beacon)
MA	missed approach
MAP	missed-approach point
max	maximum
MM	middle marker
NM	nautical miles
OM	outer marker
PS	turbine power lever (throttle) setting, 2 is full power and 10 is power off
RMI	radio magnetic indicator
RWY	runway
TED	trailing edge down
TEU	trailing edge up

A dot over a quantity represents a derivative with respect to time, and two dots represent a second derivative. A bar over a symbol indicates the arithmetic mean of the values in the sample.

Aircraft Simulated

The flight vehicle was a one-of-a-kind configuration constructed by the Cessna Aircraft Company from a number of existing components and some newly built parts. The configuration was designated the ATPTB (Advanced Turboprop Test Bed). The purpose of the test bed was to provide the company an opportunity to explore the flight characteristics and performance of this type of aircraft. A three-view drawing of the configuration is presented in figure 2. The aircraft has two Pratt and Whitney PT6-66/3 aft-mounted turbine engines driving five bladed constant-speed propellers through gear boxes that produce propeller rotation in opposite directions. The flight controls consisted of a wheel, a column, and rudder pedals connected through a conventional cable arrangement to ailerons, an elevator, and a rudder. Trim capability was generated by an aileron tab, a rudder tab, and horizontal-tail incidence. Down springs and bobweights were not used in the control system nor was a SAS (stability augmentation system) installed. A limited number of flight tests of the aircraft over an altitude—Mach number envelope were performed. Flights to an altitude of 41 000 ft were flown, and flight tests were conducted over a Mach number range up to 0.60. Limited test data have been obtained for a range of vehicle weights from 9500 lb to 14 500 lb and for center-of-gravity locations from 15 percent $\bar{c}_w$ to 28 percent $\bar{c}_w$. In assembling the test-bed aircraft, no attempt was made to optimize the configuration in regard to drag. The vehicle mass and geometric characteristics used in the present simulator study to represent the aircraft are presented in table 1 and figure 2.

Table 1. Vehicle Mass and Geometric Characteristics

Fuselage:	
Body station of fuselage nose, in.	17.88
Length, ft	44.76
Maximum diameter, in.	64.00
Wing:	
Area (trapezoidal reference), ft^2	322.25
Span, ft	51.71
Quarter-chord sweep, deg	1.41
Aspect ratio	8.30
Taper ratio (trapezoidal reference)	0.35
Mean aerodynamic chord, in.	80.98
Dihedral, deg	4.00
Root incidence, deg	3.18
Body station of wing leading edge at root, in.	230.72
Body station of moment reference center, $0.25\bar{c}$, in.	281.26
Side-of-body airfoil chord, in.	126.00
Leading-edge break airfoil chord, in.	90.99
Tip airfoil chord, in.	36.87
Tip incidence, deg	−0.77
Horizontal tail:	
Area, ft^2	67.41
Span, ft	18.35
Aspect ratio	4.99
Quarter-chord sweep, deg	31.63
Dihedral, deg	−3.00
Taper ratio	0.35
Mean geometric chord, in.	47.50
Body station of tail leading edge at root, in.	537.14
Root airfoil chord, in.	65.32
Tip airfoil chord, in.	22.87

Table 1. Concluded

Vertical tail:	
Area, ft^2	65.82
Height, in.	104.13
Leading-edge sweep, deg	43.00
Body station of tail leading edge at root, in.	441.11
Root airfoil chord, in.	113.77
Tip airfoil chord, in.	68.26
Pylon:	
Area (planform, centerline to centerline for both pylons), ft^2	20.13
Span, in.	48.37
Dihedral, deg	14.25
Body station of pylon leading edge at root, in.	351.37
Chord, in.	59.94
Propellers:	
Single rotation:	
Tip diameter, in.	100.00
Maximum nacelle diameter, in.	32.40
Body station at propeller disk, in.	434.29
Control surface deflections:	
Elevator, δ_e, deg	-16 (TEU) to $+14$ (TED)
Horizontal tail, i_t, deg	-16 (TEU) to $+8$ (TED)
Single aileron, $\delta_{a,L}$ or $\delta_{a,R}$, deg	-15 (TEU) to $+17$ (TED)
Rudder, δ_r, deg	± 25
Weight:	
W, nominal value, lb	12 500
Moments of inertia:	
I_X, slugs-ft^2	14 956
I_Y, slugs-ft^2	39 385
I_Z, slugs-ft^2	49 687
I_{XZ}, slugs-ft^2	5604
$I_{P,LE}$, slugs-ft^2	12.453
$I_{P,RE}$, slugs-ft^2	11.743

Description of Simulation

The Langley General Aviation Simulator was used in this study. The individual elements of the simulation are shown in figure 3. An engine math model, an aerodynamic math model, and a math model for control forces were required for the real-time simulation program to define a specific aircraft. Available in this program was a model for atmospheric turbulence and a table of horizontal winds having both speed and direction varying with altitude. The math models were implemented on an all-digital simulation system that used a Control Data CYBER 175 series computer. The system operated in real time at an iteration rate of 32 frames/sec. The following sections contain a detailed description of the simulator cockpit and the various math models.

Simulator Cockpit

The simulator cockpit consisted of a portion of the fuselage of an actual light, twin-engine aircraft. The cockpit was mounted on a three-degree-of-freedom motion system that provided roll, pitch, and heave motions. (See figs. 4 and 5.) The motion base is described in detail in reference 14. The instrument panel contained displays that were comparable with those in the ATPTB aircraft and provided information on altitude, airspeed, vehicle attitude, rate of climb, heading, turn and slip, values from RMI and DME, localizer error, and glideslope error,

etc. Displays for each engine were limited to engine torque, speed in rpm, and fuel flow. Although the information presented to the pilot was comparable, the panel layout of the simulator differed from that of the actual ATPTB aircraft.

The simulator was equipped with hydraulic control loaders for the elevator, aileron, and rudder cockpit controls. The force on each control was programmed on the computer, and deadbands were inserted at the computer-cockpit interface. Cockpit levers or switches were available to activate flaps, landing gear, and speed brakes. A system of speakers located around the cockpit provided a simulated noise environment. Each turboprop power unit had a power lever and an rpm lever. These four levers were located on the center console between the seats. Trim wheels for rudder and aileron tabs were also located on the center console near the floor. Longitudinal trim control was commanded through a thumb switch on the wheel. A closed-circuit color television system provided a 48° by 26° visual scene of a terrain board, which was displayed through a virtual image system through the front window. In addition, a computer-controlled cloud ceiling could be adjusted to obscure the terrain when flying above a certain altitude.

Engine Model

The information for each turboprop power unit was supplied by the Cessna Aircraft Company. The data consisted of thrust, torque, and fuel flow values supplied in tabular form as a function of four variables: Mach number, altitude (h), power setting (PS), and propeller rotational speed in rpm. Tables were provided for only two rpm values, 1700 and 2000, and were arranged in the program as shown in figure 6. Linear interpolation was used for intermediate rpm settings. The tables were part of a more extensive engine data set used by Cessna. Because of the restricted data set, special considerations were made in the math model to incorporate the engine-out condition and achieve a feathered-propeller condition. Failing either the left or right engine could be commanded only at the simulator real-time computer console. Details of the engine model are presented in appendix B.

Aerodynamic Model

The airplane is represented in the equations of motion by three force coefficients and three moment coefficients. Each of the six coefficients consists of a summation of individual aerodynamic terms or stability derivatives plus the contribution from the direct thrust output of the individual turboprop power units. The aerodynamic terms are further divided into the static and dynamic contributions. Each of the individual static aerodynamic terms is composed of three elements—one associated with the propeller removed condition and two associated with the power-induced effect of a particular turboprop unit. With this arrangement, either the left or right turboprop unit could be failed when examining the engine-out condition. The model included some effects of Mach number, sideslip angle, and ground effect. The equations of motion and the forces and moments are given in appendix C.

The expressions for the force and moment coefficients are reasonably conventional in form. The data for the various elements are contained in the software program in tabular form as a function of two variables, usually angle of attack and thrust coefficient. Data were provided for an angle-of-attack range from $-8°$ to $36°$ in $4°$ increments with an additional entry at $\alpha = 14°$ to provide better definition near the stall. Table entries were provided for thrust coefficient values of -0.0070, 0, 0.0354, and 0.2014. Wind tunnel data from powered-model tests in the Langley 14- by 22-Foot Tunnel, the 30- by 60-Foot Tunnel, and the 12-Foot Low-Speed Tunnel were used to establish the numerical values for the data tables. Some of these data are presented in references 9, 11, and 12. Interpolation and some extrapolation of the measured wind tunnel data were used to establish the table values used herein. To obtain values for the dynamic derivatives, oscillatory tests were conducted on an unpowered model in the Langley 30- by 60-Foot Tunnel. (See ref. 12.) Measurements through the angle-of-attack range were made only for the rolling-moment and yawing-moment derivatives. As a consequence, estimates were made for the pitching-moment derivatives by using information from reference 15. Power effects on the derivatives of p, q, r, and $\dot{\alpha}$ were not included because estimates of their magnitudes were questionable. Propeller forces resulting from an inclined flow at the propeller disc due to angular rates p, q, and r also were not included in the equations. Although such forces and resulting moments undoubtedly exist, they were omitted in this simulation because their computation involved unreliable estimates of their magnitude. Because the ATPTB flight Reynolds numbers were at least four times larger than any of the Reynolds numbers used in the wind tunnel tests, empirical adjustments were made in the simulation database to account for Reynolds number differences. Adjustments included increasing the stall angle of attack by several degrees and lowering some drag levels to account for reductions in the skin friction. Increasing the stall angle of attack

increased $C_{L,\max}$ and shifted all stall-related breaks in the aerodynamic characteristics to the higher angle of attack.

Control System Model

A hydraulic control loader is available in the Langley General Aviation Simulator for use with pilot-actuated controllers consisting of wheel, column, and rudder pedals. The force on each controller was programmed in the computer as a function of the cockpit trim-wheel position, deflection of the primary flight control surface (either ailerons, elevator, or rudder), and the airplane flight condition. The hinge moment data used to establish the forces for the three controls were supplied by the Cessna Aircraft Company from measurements made on a similar type of aircraft. The equations and data used are given in appendix D, and block diagrams for the longitudinal, directional, and lateral control systems are given in figure 7. Pitch trim was accomplished by adjusting the horizontal-tail incidence. A tab on the rudder provided directional trim. A trim tab located on one aileron provided roll trim in the ATPTB aircraft. This tab was not programmed in the simulation; instead, roll trim was achieved by introducing a differential increment in the deflection of the ailerons. In figure 7, three additional block diagrams for the flaps, landing gear, and speed brakes are shown with the longitudinal control system. The cockpit controls for the landing gear and speed brake had two positions, either retracted or extended. The cockpit flap position lever had four detents to position the flaps at deflection angles of 0°, 7°, 20°, and 35°. The first-order lag indicated in each block diagram was used to provide a realistic output response. The following time constants were used:

Time constants	Value	Time for full deployment, sec
τ_f	4.0	16
τ_{SB}	1.0	4
τ_{LG}	3.0	12

Turbulence and Horizontal Wind Models

To represent adverse weather conditions for this study, random turbulence was included for all flights in the test syllabus. The turbulence model used in the simulation was the standard Dryden turbulence model (refs. 16 and 17). Random turbulence for each vehicle axis was calculated independently in a subroutine and then was input into the equations for each of the three axes. Although several intensity levels were available in the simulation program, only the moderate level was used.

To increase task difficulty, a selected number of simulator flights in the test program were performed in the presence of horizontal winds. Both wind direction and magnitude were varied as a function of altitude. Only winds approaching the vehicle from the front hemisphere were considered. The winds were inserted in the simulation program as shown in the following table, and a linear interpolation scheme was used to establish intermediate values:

Altitude, ft	Wind speed, knots	Direction, deg
1600	25	0
1200	20	270
800	15	0
400	10	90
0	5	0

For altitudes above 1600 ft, the winds remained constant at the values given for the 1600-ft altitude. The null direction listed in the table was chosen parallel to the runway centerline.

Simulation Validation

Two approaches were used to establish the simulation as representative of the ATPTB aircraft. First, a number of comparisons were performed between simulator outputs and flight data to obtain satisfactory representation of the airplane flight characteristics. Second, the company pilot for the ATPTB aircraft flew the simulated airplane at altitudes and speeds of his own choosing in order to explore a larger segment of the flight envelope than involved in the test program for the purpose of providing an overall assessment of the simulation.

Data comparison from simulator and flight records are presented and discussed in detail in appendix A. Although the amount of flight data was limited, a number of comparisons of both performance and stability information were made for different speeds and altitudes. Typical comparisons include, among others, those for maximum speed, rate of climb, wind-up turns, steady heading sideslips, and several dynamic stability checks for short-period, phugoid, and Dutch roll motions. For most of the comparisons, reasonably good agreement was obtained. In some areas of the simulation, additional adjustments to the math model could have been made. However, these adjustments were not undertaken because the ILS task used for the piloted

part of the study placed the airplane in a region of the math model removed from the discrepancies. The comparison comments by the company pilot are discussed following the data comparisons.

Pilot's Task

The task selected for this study was purposely chosen to be a difficult one. The simulation approaches were initiated closer to the runway threshold than the usual ILS approach. Consequently, the time between scheduled events was compressed to accentuate the presence of any undesirable flight characteristics.

During the initial preflight briefing, each pilot was supplied with the following four items: (1) a drawing of the airplane (fig. 2), (2) a written description of the task (fig. 8), (3) a typical pilots' instrument approach procedure plate outlining the approach (fig. 9), and (4) a copy of the Cooper-Harper handling-qualities rating scale (fig. 10). A discussion of the items was conducted during which the pilots were asked to evaluate the data at each waypoint. Glideslope and localizer needle displacements of less than one-half maximum deflection should be the target for flight down the glideslope. In addition, indicated airspeed (IAS) should be maintained within ± 5 knots. Missed-approach procedures were given; however, aircraft operating procedures such as airspeed and power settings were left to the pilots' discretion. It was emphasized that a right turn was required. A Cooper-Harper rating and pilot comments were requested for every flight for the approach from flight initiation to the middle marker. An additional rating and comments were requested for the missed-approach runs covering the flight portion from the middle marker to the run termination.

ILS Geometry

The localizer transmitter was placed at the end of the 11 000-ft runway opposite the threshold and positioned on the centerline of the 150-ft-wide runway. Maximum needle deflection on the cockpit localizer instrument was set at $\pm 1.8224°$, which corresponds to a 350-ft lateral displacement at the runway threshold. The glideslope transmitter was located 1000 ft down the runway from the threshold with the centerline of the transmitter signal set at an elevation angle of 3° above the ground plane. Maximum needle deflection on the glideslope indicator corresponded to a displacement of $\pm 0.7°$ about the centerline. Vertical and lateral displacements for maximum needle deflections on the glideslope and localizer instruments at the ILS middle and outer markers are given in the following table:

ILS marker	Longitudinal position prior to threshold, ft	Glideslope max, deg	Vertical displace, ment, ft	Localizer max, deg	Vertical displace- ment, ft
Middle	2816	±0.70	±47	±1.82	±440
Outer	18081	±0.70	±233	±1.82	±925

Subjects

Six subjects participated in the test program. Two of the subjects were research pilots. One was a NASA research pilot (pilot Y) with experience in a variety of helicopters and fixed-wing aircraft, and the other was an active-duty Air Force research pilot (pilot P) temporarily assigned to NASA. Another subject was a Cessna test pilot and the principal pilot of the ATPTB aircraft (pilot L). The remaining three subjects were general aviation pilots selected for their varying level of experience. One was a certified flight instructor (pilot B) one was a private pilot with an instrument rating (pilot M) and one was a private pilot actively pursuing an instrument rating (pilot G).

Exposure to the simulation before starting the test program varied between the test subjects. The two research pilots had limited simulator exposure consisting of three or four 2-hour sessions spaced over a 4- to 6-week interval. Simulator exposure for the company test pilot was concentrated into two 4-hour sessions in two succeeding days that involved familiarization flights, test program flights, and additional evaluation flights. In contrast, two general aviation pilots had considerable simulator exposure consisting of several hours per day, twice a week, for several months before the test session. The remaining general aviation pilot, however, had only three 1-hour sessions on different days before initiation of the test program.

Test Syllabus and Data

The test syllabus consisted of a set of 16 simulator flights that were conducted in the sequence shown in figure 11. The run schedule indicated whether the run was a normal ILS approach where the console operator took control of the simulation after the middle marker was passed or whether a missed approach was to be executed. The schedule also specified the presence of winds, whether an engine failure occurred, which engine was involved, and where the failure occurred. All test runs were made in the presence

of moderate turbulence with the motion base active. Pilots were not informed of these test conditions.

Because the simulator flights were of short duration, all 16 runs could be conducted in a given 3-hour simulator session. Unfortunately, technical difficulties sometimes prevented all the runs from being conducted in one session. In such situations, the test schedule was resumed where it left off after several practice flights were made because of the time interval between simulation sessions.

A number of flights were made by the general aviation pilots to provide information on the effect of variables such as c.g. location and approach speed. These subjects also provided the test data for comparison with flight measurements.

For each test run shown in figure 11, some variables were recorded on magnetic tape at 1-sec intervals for postprocessing. For immediate use in monitoring flight progress, two time-history recorders providing 16 channels of information were used. In addition, at the completion of each run a digital printout of selected information was made available for immediate examination. Included were rms values for several specific variables for the flight trajectory segment down the glideslope. Finally, pilot ratings and comments from the research pilots and company pilot were recorded by one of the researchers who occupied the right-hand seat during the simulator runs. Comments from the general aviation pilots were recorded by the researcher monitoring the time-history recorders.

Results and Discussion

The results of the piloted runs listed in the test syllabus are presented in the following three sections. The first two sections examine the flight path trajectories and the various recorded performance measures. The third section presents the pilots' ratings and comments. Some additional simulator runs were made to briefly examine several influencing factors such as approach speed and c.g. location. These results are addressed in the section entitled "Supplemental Results." Note, all approaches performed in these tests were conducted with raw ILS error indications rather than use of more sophisticated avionics such as a flight director.

Flight Path Trajectories

Typical trajectories are presented in figures 12 and 13 for runs with both engines operating, with the left engine failed, and with the right engine failed. Values of indicated airspeed along each trajectory are also given. Vehicle longitudinal, lateral, and vertical displacements relative to the runway are measured in an axis system with the origin positioned at the runway threshold on the centerline. (Positive X-displacements are measured down the runway and positive Y-displacements place the vehicle to the right of the runway.) Note, the longitudinal scale used as the abscissa in figures 12 and 13 has been compressed with respect to the vertical scale, which tends to accentuate changes in the value of the ordinate. Results for the various pilots are shown in each figure.

ILS approaches. Figure 12 presents the results for the six pilots from initial conditions to the middle marker. Boundaries showing the values corresponding to the maximum needle deflections on the panel instruments for glideslope and localizer are provided. In addition, dashed boundary lines corresponding to twice the desired ± 5 knots tracking goal are provided for the IAS traces.

An examination of the trajectory traces between the outer and middle markers indicate that all flights were within the localizer and glideslope boundaries except for a couple of excursions on the glideslope trace shown in figure 12(b). Recall that the tracking goal specified in the preflight briefing was to remain within one-half maximum needle deflections on the final approach, whereas the boundaries shown correspond to maximum needle deflections on the instrument. The traces for the various pilots show the tracking goal was not met for a considerable portion of each run. The altitude traces for runs with a failed engine (figs. 12(b) and 12(c)) appear to be above the glideslope centerline for most of the longitudinal distance between the outer marker to the middle marker. In addition, some difficulties in localizer tracking is apparent in the oscillatory nature of the lateral positioning traces. This difficulty is apparent in the results for all three engine conditions and is partly caused by the presence of the horizontal winds. The presence of the winds also influenced the vehicle airspeed. With the exception of a few runs, airspeed varied along the final approach from the target value of 120 knots by as much as ± 10 knots. These results provided an indication of the difficulty of the task performed by the pilots.

Missed approach. Figure 13 presents the results for six pilots for that portion of the trajectory covering the transition from the instrument approach to the missed-approach segment. Engine failures were programmed to occur at the missed-approach point (MAP), which for this simulation was chosen to coincide with the middle marker. Results for both

engines operating (fig. 13(a)) show the expected increase in the airspeed after the application of power and the initial development of the right climbing turn. Altitude traces before the MAP were similar for all pilots with only the trace for pilot L showing a delay in initiating the climb. At the middle markers, the lateral positioning trace for pilot P is the only trace located to the right of the runway centerline and is the result of a correction made by pilot P to reduce the localizer error before reaching the middle marker.

When an engine was failed at the MAP (figs. 13(b) and 13(c)), some obvious differences are discernible in the traces when compared with those for both engines operating. Some pilots attempted to maintain speed and heading while adjusting to the failed-engine condition. Extra power, which was available for the aircraft for a full-throttle setting on the good engine, was used to increase altitude. When the left engine was failed (fig. 13(b)), some pilots (L, Y, P, and M) chose not to maintain tight heading control and permitted the airplane to yaw left as evidenced by the increasing negative lateral displacement before recovering and initiating the right turn. When the right engine failed (fig. 13(c)), initiation of the right turn was generated by the left engine with the pilot simply controlling the turn rate.

The minimum airspeed recorded for most missed-approach flights exceeded 110 knots; however, there were several flights with a failed engine where airspeeds as low as 90 knots were recorded. These low airspeeds caused some concern over having sufficient directional control. For these flights, however, no comments were made by the pilots concerning any difficulty in controlling the vehicle directionally. An examination of the rudder deflection required to counter the yawing moment produced by full-throttle thrust generated by the operating engine was made by using the equations in appendix C, and the results are given in figure 14. The curves indicate that for an airspeed below 94 knots, flight with zero sideslip cannot be maintained with full rudder deflection. An examination of the recorded time-history data indicate that for this portion of the flight trajectory the pilot used large rudder deflections (but less than maximum), banked the vehicle into the operating engine, and maintained a sideslip angle on the airplane. With this piloting technique, directional control remained available in both directions.

Performance Assessment

ILS approach. State variables were printed at the following four waypoints during the approach: (1) DUMMY, (2) KNUTS, (3) the outer marker (OM), and (4) the middle marker (MM). Sufficient variations existed in the numerical values of the state variables at the first two locations among the different runs by a given pilot and among the different pilots to preclude making a detailed analysis. The numerical differences were the result of how aggressively the pilots tried to laterally acquire the extended runway centerline and the specified altitude of 1000 ft at KNUTS. With the first two waypoints thus omitted from further consideration, only the final two waypoints remained. Data at both the outer and middle markers were examined with particular emphasis on more variables at the middle marker. These results are presented in figures 15 to 18.

Figure 15 presents the combined results for the six pilots and shows the vertical and lateral locations relative to the glideslope centerline existing at the outer and middle markers along with the corresponding deviation in airspeed from the desired 120 knots. All data are shown, including those values for flights with failed engines and with winds on and off. Included are the data for all missed-approach runs. The results are presented in the form of a cumulative frequency distribution, which gives the number of flights or the percentage of total flights made having a magnitude less than that specified by the abscissa. The abscissa of figure 15 was chosen to provide the results relative to the target magnitude requested in the preflight briefing and thus is designated as target size. For example, a unit target size corresponds to plus or minus one-half of the maximum needle deflections displayed on the glideslope and localizer panel instruments and to a $\pm$5-knot deviation in airspeed. The results of figure 15 indicate that the pilots reduced the localizer error and airspeed deviation during the flight between the outer and middle markers. Glideslope error, however, showed some degradation. Some loss in glideslope tracking performance may be anticipated because tracking the glideslope required continual adjustment to airspeed and to the rate of descent, whereas flight approaching the outer marker was made at a constant altitude. The airspeed result of figure 15(c) shows that only about 60 percent of the flights were within the $\pm$5-knot band at the middle marker. Position error results at both the middle and outer markers show that at least 80 percent of the flights were within the desired target band. The results shown in figures 15(a) and 15(b) for glideslope and localizer target size beyond a numerical value of 2.0 correspond to flights in which the vehicle position was beyond the range displayed on the cockpit instruments. These few flights are indicated by dashed lines and would in most cases

require a missed-approach maneuver to be executed. Because target size includes both positive and negative values, a division of the data according to sign is indicated in the following table:

Item	Location	Total flights, percentage	
		Middle marker	Outer marker
$\Delta\varepsilon$	Above glideslope	48.5	29.2
	Below glideslope	51.5	70.8
$\Delta\sigma$	Right of centerline	28.2	65.7
	Left of centerline	71.8	34.3
ΔV	Above 120 knots	30.8	35.9
	Below 120 knots	69.2	64.2

Interestingly, at the outer marker, the vehicle was positioned below the glideslope centerline about twice as often as above the centerline, whereas at the middle marker the data were about evenly divided about the centerline. The localizer data showed a reversal in the distribution of vehicle lateral position between the outer and middle markers. About two-thirds of the data place the vehicle to the right of the centerline at the outer marker and to the left of the centerline at the middle marker. An examination of the data for winds on and winds off indicated that this shift in localizer data was directly traceable to the influence of the horizontal winds. The airspeed deviation at both locations show about twice as many runs had velocities below 120 knots as above 120 knots.

The results given in figure 15 examine each of the three variables independent of the other two. For each flight, however, the piloting task was to meet all three target goals simultaneously. Accordingly, the data were recompiled, and the results obtained at the middle marker are given in figure 16. Assembling the results of the volume target clearly showed that the airspeed component had a significant influence. Because velocity deviations may be of less importance than position errors, the data were also recompiled to meet a glideslope and localizer area target. Both curves are given in figure 16. An examination of figure 16 indicates that the pilots achieved all three target goals in about 50 percent of the flights. By eliminating the velocity requirements, the pilots met the two position goals in about 75 percent of the flights.

In addition to indicated airspeed, information on flight path angles at the middle marker is also of interest. Figure 17 presents the data for pilot B as a function of E_h, which is the declination angle from the airplane altitude at the middle marker to the runway threshold. The symbols shown below the solid line in figure 17 indicate that the aircraft has a rate of descent that will lead to an impact short of the runway if not reduced. For an approach speed of 120 knots along the glideslope at the middle marker, about 14 sec of flight time remain before reaching the runway threshold, which is ample time to reduce the rate of descent. It is interesting to note in the table of figure 17 that every pilot had several flights that required reductions in the magnitude of $\dot{h}$. About 22 percent of the total flights evidenced this condition.

The interpretation presented of γ versus E_h is valid only for flights made with no winds because γ is defined relative to the air mass. Calculations were not made to account for the winds and to convert γ to an inertial-axis reference frame. The data points for the wind-on condition if corrected could shift slightly farther in the negative direction and thus would not alter the original assessment.

The single data point in figure 17 with a positive flight path angle is from a flight with a trajectory below the glideslope centerline where the pilot has already applied power to execute a missed approach.

For a typical ILS approach, the vehicle attitude angles and angular rates existing at the middle marker should be small, which would indicate that a stabilized situation exists before executing the flare. Figure 18 presents simulation results for the three Euler angles (ψ, θ, and ϕ) and three body angular rates (p, q, and r) that were recorded for the six pilots. The results are presented in the form of cumulative frequency distributions. Magnitude of the angles and angular rates was selected as the abscissa to eliminate the influence of whether the aircraft was located to the left or to the right of the extended runway centerline. For pitch angle θ, however, about 85 percent of the values were negative, which indicates that the vehicle acquired a nose-down attitude at the middle marker. The cumulative frequency distribution gives the frequency, that is, the number of flights or the percentage of the total flights made with a magnitude less than that specified by the abscissa. The curves of figure 18 indicate about 75 percent of the flights had yaw and roll attitude angles less than $\pm 6°$. Correspondingly, about 93 percent of the flights had pitch attitude angles less than $6°$. During a few flights, large roll and yaw angle magnitudes (above $10°$) were obtained. These conditions corresponded to pilot attempts to reduce the vehicle lateral displacement from the extended runway centerline. Large roll and yaw rates usually accompanied these larger angle displacements.

In addition to the instantaneous conditions existing at the outer and middle markers, measurements of pilot performance and the control deflections used were obtained for the vehicle trajectory down the glideslope measured between the outer and middle markers. These measurements are in the form of rms values obtained from data taken at the sampling rate of 32 samples/sec. Figure 19 presents typical results by providing values for every run made by a single pilot during the test program. The effect of engine failure for both winds on and winds off is given for each variable. The tracking errors $\Delta\varepsilon$ and $\Delta\sigma$ in figure 19 are the angular errors from the nominal glideslope and localizer values as represented by the needle displacements on the cockpit instruments. The rms values of IAS are referenced to zero airspeed. Similarly, rms values of aileron, elevator, and rudder deflections are referenced to zero deflection. Horizontal-tail incidence, however, was referenced to the trim value at the initiation of each flight. This bias in rms i_t obviates the direct relationship between the rms values for elevator and horizontal-tail incidence.

Several observations can be made from an examination of the data of figure 19. Increases in rms δ_r are larger when either the left or right engine is failed than when both engines are operating. A similar increase, although of much less magnitude, is apparent in the aileron data. These observations hold for both wind-on and wind-off conditions. A comparison of localizer tracking error data indicates a larger error exists for wind-on conditions than for wind-off conditions. Other observations are not as obvious because of the scatter in the data and the limited number of data points. These three observations were readily apparent in the test data for each of the six pilots. To further illustrate the tracking error results, figure 20 shows the cumulative result of the six pilots for both wind-on and wind-off conditions with both engines operating and with one engine failed. Mean values and standard deviation bars are presented. Figure 20 indicates that the presence of winds or an engine failure had little effect on the glideslope rms error means and standard deviations. Similarly, not much difference was obtained in the airspeed results for the different conditions. The localizer error results, however, show a large effect due to the presence of the horizontal winds for both engine conditions. In contrast, little influence is shown when comparing the localizer data for the effect of engine failure. (In fig. 20, compare circle with diamond symbols and square with triangle symbols.) Apparently piloting adjustments to the presence of a failed engine were completed by the time flight down the glideslope was initiated, whereas the presence of the varying winds required constant adjustment during the final approach. A statistical check on the glideslope, localizer, and airspeed data with the Student's "t" test indicates that the effect of winds on the localizer results was significant at the 5-percent level of significance.

Missed approach. Upon reaching the middle marker with the runway not visible, the required procedure was to execute a missed approach. The test matrix for these runs incorporated the following three engine conditions: (1) both engines operating, (2) one engine failed at the middle marker, and (3) one engine failed shortly after starting the run at $h = 1300$ ft. Engine failures included both left and right engines, and the runs were made with and without the presence of the horizontal winds. Although no specific performance measures were specified in the pilot's preflight briefing for the missed-approach portion of the trajectory, data for some variables were printed at run termination. Among these variables were time intervals measured from passage over the middle marker to activation of respective panel levers by the pilot that indicate the pilot's response to the missed-approach situation. Results obtained by the research pilots and Cessna test pilot for several of these time intervals are given in table 2. Because piloting procedures affecting these variables were not specified for the missed-approach task, the results are not discussed and are included as additional task information.

Several other parameters were also available for the missed-approach runs. One was the minimum altitude of the trajectory, which is a function of rate of descent and the altitude existing at the middle marker as well as pilot control inputs. An examination of all data runs showed that all trajectories remained above an altitude of 100 ft except for one run made by pilot Y in which the aircraft descended to an altitude of 63 ft.

Data for three other parameters of interest are given in the following table and are defined as follows:

H200IAS—indicated airspeed in knots when vehicle reacquires an altitude of 200 ft

TH1000—time from passage over middle marker for vehicle to reach an altitude of 1000 ft

TPSI180—time from passage over middle marker for vehicle to complete 180° turn to right

Table 2. Time-Interval Data for Missed-Approach Runs

[Time designations are defined as follows: THDOTO, time from middle marker (MM) to zero rate of descent ($\dot{h} = 0$); TGEARUP, time from MM to lever activation for landing gear retraction; TFLAP20, time from MM to lever activation to retract flaps to 20°; TFLAPUP, time from MM to lever activation to retract flaps to 0°]

Pilot[a]	THDOTO, sec			TGEARUP, sec			TFLAP20, sec			TFLAPUP, sec		
	Mean value	s^*	Data points	Mean value	s^*	Data points	Mean value	s^*	Data points	Mean value	s^*	Data points
Y	7.5355	4.0245	7	14.5914	3.2630	7	6.7043	2.0576	7	21.2175	3.8444	4
P	5.5500	2.3752	10	15.0450	5.6373	10	16.6840	7.6757	10	35.0986	6.5975	7
L	7.5310	3.4843	10	21.1470	6.8570	10	12.6310	5.8016	10	36.2880	14.4286	6

[a]For all pilots, runs omitted for flaps full up when lever first engaged; for pilot Y, flaps at 20° for one run, and for pilot L, flaps at 20° for two runs.

Parameter	Both engines operating		One engine failed	
	Mean value	s^*	Mean value	s^*
H200IAS, knots	127.52	11.54	119.53	5.27
TH1000, sec	29.97	6.57	84.75	12.76
TPSI180, sec	66.77	12.65	86.10	11.96
Data points	12		37	

To provide representative values for the missed-approach maneuver, the data for all piloted runs were combined into composite values for both engines operating and one engine failed. The trends shown in the table were evident in the results for each individual pilot. An examination of the values in the table show the expected difference due to the presence of a failed engine. With both engines operating, the average time to complete the turn was only slightly longer than that required for a standard rate turn of 3°/sec. In the case of the failed engine, runs occurred in which the 180° turn was completed before the vehicle reached an altitude of 1000 ft. These runs are the reason for the small difference between the mean values for TH1000 and TPSI180.

Pilot Evaluations

Cooper-Harper ratings were provided by the two research pilots at the completion of each run. A single rating was given for all flights from run initiation to the middle marker, and a separate rating was given for the missed-approach maneuver. These results are arranged in tabular form in figure 21 with the ratings by the two pilots presented side by side for the same test condition. As presented, a comparison of ratings can also be made for the effect of winds and engine out. Pilot comments were obtained after each run and salient excerpts are included.

As shown in the tables, most ratings were either a 4, 5, or 6. According to the handling-qualities chart of figure 10 these ratings indicated that performance was acceptable but that existing deficiencies warrant improvement. Several ratings of 7 also appear in the table. These values were given by pilot P and involved runs with a failed engine. In general, pilot P provided average ratings for a given data set having an additional one point degradation over those given by pilot Y. At the completion of the test program, pilot P commented that under optimum weather conditions and with both engines operating, the best rating that could be hoped for would be a 3. One flight was made with both engines operating by pilot Y in which turbulence and winds were eliminated, and pilot Y gave this flight a rating of 3. Pilot Y commented after the flight that the presence of turbulence had an influence on the ratings. Pilot P also commented that he thought the aircraft was certifiable under the FAR's (Federal Air Regulations, ref. 18).

Both research pilots indicated that the ratings from 4 to 7 were primarily the effect of two factors. One factor was the predominant pitch coupling with changes in power setting as a result of the high location of the engines and the other factor was low directional damping. The pilots commented that when reducing power during descent, the vehicle nose pitched up and when adding power for leveling off or executing a missed approach, the vehicle nose pitched down. The latter occurrence was particularly disturbing during two-engine missed approaches at IFR (instrument flight rules) minimums. These vehicle responses are opposite of those normally encountered for most aircraft. Because of

these responses, the pilots needed to watch both the vehicle attitude and engine torque indicators when making power changes. Unfortunately, as mentioned by the pilots, the layout of the instrument panel did not facilitate this. Regarding the second factor, low directional damping, the pilots commented that precisely maintaining a heading was difficult, and this difficulty resulted in flying in an S-shaped pattern across the final approach course for flight down the glideslope. They further commented that capturing a given heading from a standard rate turn was also difficult. To improve the vehicle handling qualities, they suggested that the flight control system be augmented to eliminate pitch coupling with power and that a yaw damper be added to improve lateral-directional characteristics.

The Cessna test pilot indicated that he was not experienced with using the handling-qualities chart of figure 10. He was more concerned with the certifiability of the configuration under the FAR's and ensuring suitable handling qualities for customer acceptance. Most of his comments, therefore, concerned comparison between the simulator and the actual test-bed aircraft. (See comparisons in appendix A.) Nevertheless, he indicated that the simulator provided a reasonably good representation of the aircraft for the portion of the flight envelope examined and that the configuration as tested was in the certifiable range. Increases in pitch and yaw damping, reductions in pitch coupling with power, and control force reductions with flap deflection would be desirable improvements.

The general aviation pilots, although not qualified to rate handling qualities using the chart of figure 10, provided comments similar to those of the research pilots. Major criticism by all three pilots concerned pitch coupling with power and low directional damping.

Supplemental Results

To examine what effect slower approach speeds would have on the ILS task, pilots B and G made runs in which the vehicle was trimmed at different airspeeds at the initial condition position. These ILS approaches were to be made at constant airspeed with no turbulence and no winds to isolate the effect of approach speed. Flights were initiated at trim indicated airspeeds of 120, 110, 100, and 90 knots. At the completion of the test runs, the pilots commented that the lateral-directional handling characteristics were poorer at 110 knots than at 120 knots and they degraded rapidly as airspeed was reduced. Longitudinal handling characteristics also degraded as airspeed was reduced. Figure 22 presents the rms data for tracking error and control inputs for the two pilots. Increasing rms values with decreasing airspeed, particularly for the control deflections, corroborate the comments provided by the pilots. One difficulty mentioned by the pilots was the difficulty in setting the throttles. Delays in vehicle speed response following a power adjustment at the slower speeds led to overshoots when trying to achieve a desired setting.

Several flights were made with no winds and no turbulence to examine the effect of longitudinal c.g. location on task difficulty. Runs were made by pilots B and G with the vehicle c.g. at a forward location of $0.189\bar{c}_w$ and at a rearward location of $0.276\bar{c}_w$. These locations corresponded to the most-forward and most-rearward positions examined in the ATPTB flight test program. Pilots felt the changes in c.g. location for the simulator runs were of less significance than the changes in approach speed.

Summary of Results

A motion-base piloted simulation study has been conducted with the Langley General Aviation Simulator to examine the task performance and handling qualities of an advanced twin-engine turboprop business/commuter aircraft configuration during both an instrument landing system (ILS) approach and a missed-approach task. The simulation math model was generated to approximate the characteristics of the Cessna Aircraft Company's ATPTB (Advanced Turboprop Test Bed). Comparison of simulation and flight test data was used to establish validation. Simulation flights were made in the presence of varying horizontal winds and with an engine-out condition. All flights in the test program were conducted in the presence of moderate turbulence and with the motion base active. Six pilots consisting of two research pilots, a Cessna test pilot, and three general aviation pilots participated in the investigation. Results of the study are as follows:

1. Comparisons of simulation results with flight test data indicate the simulation was a valid representation of the Cessna ATPTB aircraft over a considerable portion of the aircraft flight envelope. The differences that existed were far removed from the region of flight used in the ILS and missed-approach tasks of this study. The qualitative remarks of the company test pilot support the quantitative results.

2. Successful ILS approaches and missed-approach maneuvers were performed by each of the six test pilots for the different wind and engine-out conditions of the test program. Pilots commented on the difficulty of the high-work-load task, which

was compounded by the presence of pitch coupling with power due to the high engine location relative to the vehicle's center of gravity and by the configuration's low directional damping. These two factors were directly reflected in the handling-quality ratings of 4 to 7 given by the research pilots and were the two items suggested for improvement. The vehicle was considered to be in the certifiable range under the present Federal Air Regulations.

3. Flight trajectories between the outer and middle markers show that most vertical and lateral excursions from the glideslope centerline were within the limits indicated by the maximum glideslope and localizer needle deflections. For a portion of most trajectories, however, excursions were recorded that exceeded the one-half maximum needle deflection specified as the desired task target limit.

4. Performance measures show the vast majority of flights were positioned vertically and laterally within the target cross section at the middle marker and were within the target velocity bounds. The root mean square (rms) values down the glideslope indicate larger rudder and aileron deflections were experienced when an engine was failed. The rms localizer tracking error was larger for flights when the horizontal winds were present; however, no difference due to winds was detected in rms glideslope tracking error.

5. Different procedures were used by the six pilots in executing the missed-approach portion of the simulator flights and all flights were performed successfully. Minimum altitude during a missed approach for all flights except one was above 100 ft. The time required to reach an altitude of 1000 ft was increased by a factor of 3 for flights involving a failed engine.

NASA Langley Research Center
Hampton, VA 23681-0001
September 30, 1993

Appendix A

Simulation and Flight Test Results

Comparisons of simulation and flight test data were made for simulation validation. These results are given in figures 23 to 43 and in tables A1 and A2. Included among the comparisons were those involving vehicle performance and various measures of aircraft flight characteristics as discussed subsequently. Because the same flight test was repeated at different airspeeds, altitudes, and c.g. locations, more than one comparison of a given flight characteristic was made. Comments of the Cessna test pilot comparing various aspects of the simulation with comparable experience on the aircraft are presented to provide added information addressing the adequacy of the aircraft representation.

Performance

Several performance measures of the ATPTB (Advanced Turboprop Test Bed) aircraft were calculated by the Cessna Aircraft Company using flight-measured drag values and the Pratt and Whitney Company engine performance deck. Maximum true airspeed and maximum rate of climb were calculated at various altitudes with this information, and the results are given in figure 23. Corresponding maximum values for the simulation were obtained for trimmed flight at the various altitudes, and these results are included in figure 23 for comparison with the estimated flight values. Agreement between the curves is considered to be good. The difference in airspeed at altitudes above 30 000 ft may be partly due to differences in the atmospheric model used in the calculations.

Longitudinal Characteristics

Static stability. Static longitudinal stability data in the form of control-column force and elevator deflection versus airspeed were available from a series of aircraft flight tests in which factors such as center of gravity (c.g.) location, trim speed, and flap deflection were varied. Some comparisons of simulator results with flight data are presented in figures 24 and 25. Use of parameters $\delta_e - \delta_{e,\text{trim}}$ and $F_c - F_{c,\text{trim}}$ in the figures permit adjustment of the data for differences in trim conditions. Longitudinal trim in the aircraft produced zero column force. For this condition, the elevator was deflected. In the simulator, the trim routine set the elevator deflection to zero and adjusted horizontal-tail incidence. Eliminating the trim values permits a more direct comparison of the variation with speed. Figure 24 presents the data comparisons for the cruise configuration for two different c.g. locations, and figure 25 presents the comparisons for the landing configuration for three different c.g. locations. The simulator and flight test data on all five comparison figures appear to be in reasonably good agreement. This agreement is particularly apparent for the elevator deflection data. Measurements for the simulator column-force data including both the push and pull forces appear linear over the speed range. This linearity occurs because the values presented do not contain the breakout forces, which are input to the control system at the computer-cockpit interface. The flight test data, however, includes both breakout and friction forces. The resulting displacement about the trim position is readily apparent in figure 25. The data sets for both cruise and landing configurations appear to provide similar slopes and yield a force gradient with speed of about 1 lb/6 knots.

Neutral point. Stick-fixed neutral points were determined for the simulated vehicle in the cruise and landing configurations to permit comparisons with flight test results. Trim conditions for straight and level flights were established for a range of airspeeds for each configuration with the vehicle c.g. positioned at several different longitudinal locations. Figure 26 presents these results and establishes the neutral-point location for each configuration. In the computer program simulation, longitudinal trim was obtained by adjusting horizontal-tail incidence while holding zero elevator deflection. In flight, the aircraft horizontal-tail incidence was held fixed once it was initially set and the elevator deflection was adjusted to provide trim conditions. Either method can be shown to provide the desired result. Figure 27 compares the simulator values as determined by figure 26(a) and 26(b) with those values determined by Cessna from flight test measurements. Simulator values from figure 26(b) are also used for comparison in figure 27 for the flap-down and gear-up condition because the landing gear as simulated provided no contribution to longitudinal stability. The neutral-point results of figure 27 are presented against lift coefficient; this was the format used for the flight test results. The comparisons show fair agreement. Some differences between simulator and flight test results can be traced to data reduction difficulties caused by scatter in the flight test measurements.

Maneuver stability. Comparisons of simulator and flight test data for maneuver stability are given in figure 28 for the cruise configuration and in figure 29 for the landing configuration. Measurements of control-column force and elevator deflection versus load factor are presented for each configuration. The data were obtained from wind-up turns performed in

both the left and right directions. Figures 28 and 29 show that reasonable agreement was obtained between simulator and flight data. Some differences in elevator deflection exist between simulator and flight values at load factors above 1.8. Excellent agreement, however, was obtained at the lower load factors, and values of elevator deflections per g appear nearly identical for the simulator and aircraft in this load factor range. An examination of the column-force measurements shows that scatter exists in the flight test data, particularly those values obtained for the right turn for both cruise and landing configurations. Values taken during the left turn appear to be more consistent. As previously mentioned, the simulator values are the calculated computer inputs to the cockpit hydraulic control loader, whereas the flight data contained control-system friction and breakout forces. Overall, the comparison is considered reasonable because stick force per g is similar for the aircraft and simulator in the load factor ranges between 1.2 and 1.8. Values for the maneuver parameters $\frac{\partial \delta_e}{\partial n}$ and $\frac{\partial F_c}{\partial n}$ obtained from the simulation data are given in the following table:

Configuration	$\frac{\partial \delta_e}{\partial n}$, deg/$g$	$\frac{\partial F_c}{\partial n}$, lb/$g$
Cruise	−4.50	14.50
Landing	−6.75	13.40

Dynamic stability. A limited amount of dynamic stability data was obtained for the ATPTB aircraft. Short-period data consisted of a few oscillatory traces taken for both cruise and landing configurations operating at an altitude around 15 000 ft with the c.g. at a forward location ($0.189\bar{c}_w$). The aircraft short-period motion appeared damped for all test cases with no evidence of persistent residual oscillations. No attempt to establish values of frequency and damping ratio were undertaken due to the small amplitude of the motion. Phugoid data were not available at this altitude. Dynamic stability data were obtained for the simulation with the math model in conjunction with the computer program of reference 19. Frequency and damping ratio values were obtained for the cruise and landing configurations operating at an altitude of 15 000 ft because most of the flight test data were obtained at this altitude. Calculations were made for several c.g. locations, including the most-forward and most-rearward locations used in the flight tests. The results are presented in table A1. Both short-period and phugoid data are provided. (The lateral characteristics listed in the table are discussed subsequently.) An indication of the flying qualities of the simulated vehicle is given in figures 30 and 31, which used the charts taken from references 20 and 21. For the altitude and airspeed used in the calculations, satisfactory longitudinal flying qualities are predicted. Similarly for the phugoid motion, level 1 flying qualities are predicted for all cases in that the predicted oscillations have periods considerably longer than 20 sec and damping ratios in excess of 0.04. Several flight records for the phugoid motion were obtained with the ATPTB aircraft flying at an altitude of 35 000 ft. Time-history traces constructed from the flight records are presented in figure 32. Values for period and damping ratio evaluated from the airspeed trace are listed in the figure. To provide a comparison, calculations were made for the simulation for comparable test conditions through use of the computer program of reference 19 and these results are also provided in the figure. The frequency and damping values obtained for simulation and flight are in excellent agreement.

Trim change with thrust. A change in longitudinal trim with thrust setting would be expected because of the high engine location relative to the center of gravity. A comparison of trim change with application of power between flight test data and simulator results is given in figure 33. The overall increments in column force and elevator deflection between $t = 10$ sec and $t = 26$ sec are in reasonable agreement. The smooth traces shown for the simulator data are the direct result of using two test subjects to perform the task. The pilot in the right seat operated the throttles to provide a smooth application of power with time while the pilot in the left seat flew straight and level while maintaining altitude. Zero elevator deflection exists at $t = 0$ since the simulated vehicle was longitudinally trimmed for straight and level flight with horizontal-tail incidence. Differences in horizontal-tail trim setting could account for part of the initial elevator differences shown.

Lateral-Directional Characteristics

Directional stability. Static directional stability comparisons of simulation and flight test data are presented for the cruise configuration in figure 34(a) and for the landing configuration in figure 34(b). The data in both the simulator and aircraft were obtained from piloted steady-heading sideslip runs. This procedure was used for the simulation to directly obtain values for rudder pedal force at the completion of a run. An examination of the figure indicates good agreement exists between simulator and flight results for rudder deflection with sideslip angle. The

comparison of rudder pedal force, however, shows that larger forces were needed in the simulation than in flight to produce the same sideslip angle. These differences, although not noticeable for small sideslip angles, would be particularly obvious when the pilot tried to generate large sideslip angles. The major contributor to the simulation's large pedal forces was the omission of the effect of the rudder tab in computing the pedal forces. (See appendix D.) Improved comparisons in figures 34(a) and 34(b) would result if the reductions in the force levels due to the tab were included in the simulation. The effect of the rudder tab was included in the aerodynamic forces and moments and thus provided the good agreement shown for rudder deflection.

Dynamic stability. Some flight tests were made to evaluate the ATPTB Dutch roll characteristics for both cruise and landing configurations for several Mach numbers at altitudes up to 35 000 ft. The natural frequency and damping of the Dutch roll motion were evaluated from traces of sideslip angle versus time. A typical example of these data is given in figure 35. Time-history traces for the same test condition in the simulation are presented in figure 36. The latter traces resulted from a pedal kick with full rudder deflection. Some disturbances in the longitudinal characteristics are apparent in the traces for a short time interval following the large rudder input. Natural frequency and damping ratio values were evaluated from flight and simulator traces with the assumption that the motion was produced by a second-order system and the results are given in table A2. Also listed are frequency and damping values evaluated from similar traces for the landing configuration. An examination of the table shows the results to be in reasonable agreement.

Additional values of Dutch roll characteristics for the simulated vehicle are contained in table A1. As mentioned previously, these values were obtained with the computer program described in reference 19. The tabulated frequency and damping-ratio values show only small changes as a result of shifting the c.g. from $0.189\bar{c}_w$ to $0.276\bar{c}_w$. Of more interest are the magnitudes shown in the table. A comparison of these values with values for the minimum frequency and damping requirements given in reference 20 and in reference 22 show that the natural frequencies are in the satisfactory range; however, the damping-ratio values are somewhat low. Figure 37 shows these values placed on the Dutch roll flying-qualities chart of reference 20. Level 1 flying qualities are indicated for the cruise configuration. For the landing configuration, only level 2 flying qualities are indicated for all three c.g. positions. Some improvement in damping ratio may be desirable for this configuration. The results of the dynamic stability analysis given in table A1 also showed the spiral mode was slightly stable with a large time constant. This result was obtained for both cruise and landing configurations. Reference 20 indicates such values represent level 1 flying qualities. Recall that for the spiral mode, level 1 flying qualities apply until the time to double amplitude is less than 20 sec. All roll-mode time constants given in the table are less than 1 sec, which indicates level 1 flying qualities.

Engine out. Limited flight test data were obtained with one engine inoperative and the propeller feathered to establish the minimum engine-out control speed for the ATPTB. During this process, values for rudder deflection and pedal force were recorded for a range of airspeeds. Figure 38 presents a comparison of these flight test values with results obtained from piloted runs in the simulator for the landing configuration with the left engine out (propeller feathered). The trend of increasing force and deflection magnitudes shown for the simulator results at the lower airspeeds was also observed in other flight test data. In addition, the recorded measurements for the simulator runs showed a rate of descent from 5 to 10 ft/sec existed at all airspeeds. Undoubtedly, the presence of a descent rate is the reason simulation airspeeds as low as 80 knots were obtained. As noted in figure 38, bank angle for the flight test data points was about 5°. Simulation printouts showed both ϕ and β were of the order of 1° or less. Since both data sets were from piloted runs, the comparison shown in figure 38 seems reasonable. Figure 39 presents further comparison of simulation data for right engine failed. The corresponding flight data were unavailable; thus, to provide a comparison, the flight test data for the left engine failed (fig. 38) were replotted in figure 39 with the signs reversed. A comparison of simulation and flight test results show good agreement for rudder deflection, but some differences exist in pedal force. Recall that sideslip angle has a large influence on rudder deflection and pedal force. Any difference in sideslip angle β between flight and simulation could easily account for the differences shown in figures 38 and 39.

Lateral stability. Static lateral stability of the ATPTB aircraft and the present simulation is given in figure 40, which presents a comparison of measured data obtained from steady-heading sideslip maneuvers. Values of aileron deflection and wheel forces are shown as a function of sideslip angle. The data of figure 40(a) for both the simulation and aircraft are for comparable conditions. The large discrepancies between the two data sets of figure 40(a) is due

not only to the equations and values used in the simulation but also to difficulties in obtaining accurate flight measurements. Accurate flight values of wheel force and aileron deflection are difficult to acquire for small surface deflections because of the presence of breakout and friction forces as well as cable stretch existing in the aircraft control system. The slope of the curves of δ_a versus β (fig. 40(a)) shows that the simulation has almost twice the magnitude as the flight data. Unfortunately, the total increment of aileron deflection for the β range tested for the flight data was only about 1°. In addition, the wheel force data appear invariant with sideslip angle. Consequently, a second comparison was undertaken and the results are presented in figure 40(b). For this comparison, some differences exist in the configurations tested; however, both data sets were obtained at altitude with the same c.g. location and reasonably comparable airspeeds. The slopes of the curves of δ_a versus β are nearly the same, and the comparison of wheel force data is much improved. (Note, flap deflection affects aileron effectiveness in the region of the stall but has little influence at the angles of attack corresponding to the listed flight speeds.)

Roll rate. To provide roll rate values for comparison with flight test data, simulation values were obtained with the pilot conducting a bank-to-bank rolling maneuver. The maneuver began by setting an initial bank angle of $\approx 60°$. Aileron step inputs were then input in the direction of reduced bank angle. Wheel position was held constant until the motion passed through zero roll angle. Data were recorded when roll angle was zero. A number of runs were made varying the size of the aileron input. Results for roll rate, aileron deflection, and wheel force obtained for the cruise and landing configurations are compared with flight test measurements in figures 41 and 42. Each figure presents the results for a given pilot. The comparisons presented in figures 41 and 42 show fair agreement between simulation and flight data for roll rate versus aileron deflection and poor agreement for the corresponding wheel force curves. Some differences were anticipated in these comparisons because adjustments were made in the computer program following the Cessna test pilot's initial exposure to the simulation. He commented that wheel deflection was excessive and commanded too little vehicle roll response. Adjustments were made to the gain settings in the program until the Cessna test pilot felt a reasonable resemblance between simulation and the ATBTB aircraft was achieved. Because of scheduling constraints, no further comparison checks were undertaken and the test program was immediately initiated. Since the primary factors affecting the pilot's judgment are wheel force and the resulting roll response, typical cross plots of the data for the landing configuration shown in figures 41(b) and 42(b) are presented in figure 43. These results indicate that the simulation produces less roll rate for a given applied wheel force than that produced in the aircraft. Slopes of the simulator data $\frac{\partial p}{\partial F_w}$ are 80 to 85 percent of the slopes shown for the ATPTB aircraft. This difference could be partly due to the manner in which the data were acquired. Nevertheless, differences of this magnitude would be difficult for a pilot to detect.

Miscellaneous Characteristics

Lift-curve slopes. Figure 44 presents a comparison of flight test and simulator trim lift curves. Results are presented for the flaps set at three different deflection angles. For all three cases, a slight displacement exists between comparable curves; however, the lift-curve slopes are nearly the same. The angle-of-attack values for the flight test data were obtained from the pitch rate gyro while speed and power measurements were being taken. The simulation values were obtained for a 12 500-lb vehicle with the c.g. at $0.25\bar{c}_w$. Differences in c.g. locations can account for part of the displacement between the trim lift curves.

Stalls. Several $1g$ stalls with wings level at an altitude of about 10 000 ft were attempted by the Cessna test pilot with the simulated vehicle in both the cruise and landing configurations. For both configurations, the vehicle at the stall break pitch-up as a result of the unstable break in the pitching-moment data programmed in the simulation. This result is directly opposite to that experienced in the aircraft. Flight test data indicate a gentle pitch-down occurs at the stall break. Apparently, modifications to the simulation database at stall break are required if the simulation is to duplicate the aircraft stall motions.

Cessna Test Pilot Evaluation Comments

The Langley Advanced Turboprop Simulator was evaluated during two simulator sessions. Approximately 17 ILS approaches were flown in the presence of moderate turbulence with varying combinations of wind shear, cross winds, and engine failures. In addition to the landing approaches, basic handling qualities were evaluated at speeds up to about 230 knots at low altitudes. The following comments compare the flight simulator with the engineering test aircraft.

1. The pitch-down with power application for the simulator appears to be a little more pronounced than it is for the aircraft.
2. The pitch change with flap extension is accurate.
3. The pitch trim rate is accurate, but the aircraft has an initial lag due to actuator inertia. Quick short-duration trim inputs do not provide a trim change in the aircraft.
4. Static longitudinal stability is well simulated.
5. Pitch response to a given force is accurate. The aircraft requires considerably more control displacement for a given response as compared with the simulator.
6. The dynamic and static directional stability is well simulated.
7. Lateral control force gradient is steeper in the aircraft. The aircraft feels as if it has a spring with a preload that must be overcome to deflect the aileron. (Note: This is an illusion as the system has no springs.)
8. Roll rate versus control deflection appears to be similar.
9. The simulator has more adverse yaw than the aircraft.
10. The engine-out characteristics are well simulated. Rudder force versus deflection and rudder power is good. Trim ability is accurate.
11. Static lateral stability in the landing configuration at low speeds is better in the simulator than it is in the aircraft.
12. An accurate check was not made on climb performance, but both single engine and multiengine climb performance appears to be close to that of the aircraft.

Table A1. Simulation Dynamic Stability Data

c.g., percent of $\bar{c}_w$	Longitudinal				Lateral			
	Phugoid		Short period		Dutch roll		Spiral	Roll
	ω_n, rad/sec	ζ	ω_n, rad/sec	ζ	ω_n, rad/sec	ζ	τ_s, sec	τ_r, sec
Cruise configuration[a]								
18.9	0.1221	0.0742	3.586	0.3966	2.320	0.0889	300.2	0.2219
25.0	.1220	.0725	3.260	.4296	2.265	.0864	242.3	.2217
27.6	.1204	.0716	3.110	.4475	2.241	.0853	223.0	.2216
Landing configuration[b]								
18.9	0.1721	0.1280	2.627	0.4104	1.744	0.0473	57.51	0.2893
25.0	.1732	.1224	2.396	.4439	1.701	.0425	53.51	.2887
27.6	.1738	.1194	2.290	.4618	1.683	.0404	51.91	.2884

[a]Weight = 13 000 lb $\quad \delta_f = 0.0°$
Altitude = 15 000 ft $\quad$ Landing gear up
Trim IAS = 180 knots

[b]Weight = 13 000 lb $\quad \delta_f = 35°$
Altitude = 15 000 ft $\quad$ Landing gear down
Trim IAS = 140 knots

Table A2. Flight and Simulator Dutch Roll Characteristics

	Cruise configuration	Landing configuration
IAS, knots	190	142
h, ft	14 200	14 000
W, lb	12 900	12 700
c.g., percent of $\bar{c}_w$	27.6	27.6
δ_f, deg	0	35
Gear	Up	Down
Flight control free:		
$\zeta\omega_n$	0.116	0.132
ω_n, rad/sec	1.85	1.57
ζ	0.064	0.084
Simulator control fixed:		
$\zeta\omega_n$	0.232	0.112
ω_n, rad/sec	2.34	1.73
ζ	0.099	0.065

Appendix B

Engine-Propeller Math Model

Basic information on a single-turbine-engine and propeller combination was supplied by the Cessna Aircraft Company. Data tables for thrust, torque, and fuel flow were provided as a function of four variables: altitude (h), Mach number (M), power setting (PS), and propeller rotational speed (rpm). Data entries were provided for altitudes from sea level to 43 000 ft, for Mach numbers up to 0.65 and power settings from full throttle (PS = 2) to flight idle (PS = 7). Data were linearly extrapolated in the simulation to obtain values between flight idle and power off (PS = 10). Only data sets at 1700 rpm and 2000 rpm were provided. In the simulation, the data were linearly interpolated for intermediate rpm values. Data entries at 2000 rpm were used for all rpm values exceeding 2000 rpm. Similarly, data entries at 1700 rpm were used for all rpm values less than 1700 rpm. Figure 45 is a sketch illustrating this formulation for the thrust of a single-turbine-engine and propeller combination operating at sea level ($h = 0$) and a low Mach number ($M = 0.1$). (Note, the negative thrust values were obtained for the power-off condition (PS = 10) because of the drag of the propeller.)

An engine-out condition for either engine could be commanded from the main computer console at any time during a simulated piloted flight. Once an engine was failed, further computer inputs from pilot operation of the cockpit engine controls for the failed engine were bypassed. Block diagrams detailing this process for a single-turbine-engine and propeller combination are given in figure 46. When an engine failure occurred, the torque, fuel flow, and rpm readings were reduced to zero through use of a first-order lag. Thrust output was reduced in a somewhat similar manner except rather than zero, the final thrust output acquired a negative value indicating an increase in drag of the power unit. The values used herein for $C_{T,\text{windmilling}}$ and $C_{T,\text{feathered}}$ were obtained from the drag data in reference 11 at an angle of attack of 0°. This latter modification to the thrust block diagram was made to represent an autofeather mode and was included because it was believed a production aircraft would have this feature. Values of the three different time constants used in the engine model for the present study are given in figure 46. Tabulated values of thrust, torque, and fuel flow are given in tables B1 and B2. For conciseness, the data sets have been limited to the parameter ranges used in the present ILS approach and go-around study. The full range of values, however, was programmed and available in the simulation.

Table B1. Single-Engine Thrust, Torque, and Fuel Flow Values for 1700 rpm

PS	h, ft	Thrust, lb, at—			Torque, ft-lb, at—			Fuel flow, lb/sec, at—		
		$M = 0.1$	$M = 0.2$	$M = 0.3$	$M = 0.1$	$M = 0.2$	$M = 0.3$	$M = 0.1$	$M = 0.2$	$M = 0.3$
2	0	2144.90	1580.90	1152.20	2364.00	2364.00	2363.90	530.20	530.40	519.00
	10K	1847.20	1537.90	1172.00	2364.00	2364.00	2364.10	467.50	465.80	457.00
3	0	2144.90	1580.90	1152.20	2364.00	2364.00	2363.90	530.20	530.40	519.00
	10K	1847.20	1537.90	1172.00	2364.00	2364.00	2364.10	467.50	465.80	457.00
4	0	2144.90	1580.90	1152.20	2364.00	2364.00	2363.90	530.20	530.40	519.00
	10K	1847.20	1537.90	1172.00	2364.00	2364.00	2364.10	467.50	465.80	457.00
5	0	2144.90	1580.90	1152.20	2364.00	2364.00	2363.90	530.20	530.40	519.00
	10K	1847.20	1537.90	1172.00	2326.80	2364.00	2364.10	462.40	465.80	457.00
6	0	1942.10	1430.50	1117.20	2015.30	2109.70	2292.00	482.30	495.00	509.30
	10K	1649.50	1287.30	1020.60	1843.90	1901.10	2035.70	394.90	403.10	412.50
7	0	1385.20	968.70	773.80	1289.80	1386.60	1590.50	388.20	400.70	418.50
	10K	1336.90	974.60	757.30	1318.10	1378.20	1496.10	322.40	330.60	339.20

Table B2. Single-Engine Thrust, Torque, and Fuel Flow Values for 2000 rpm

PS	h, ft	Thrust, lb, at—			Torque, ft-lb, at—			Fuel flow, lb/sec, at—		
		$M = 0.1$	$M = 0.2$	$M = 0.3$	$M = 0.1$	$M = 0.2$	$M = 0.3$	$M = 0.1$	$M = 0.2$	$M = 0.3$
2	0	2542.10	1834.10	1339.40	2363.40	2363.50	2363.50	598.30	598.80	585.80
	10K	2292.10	1806.40	1381.50	2363.50	2363.50	2363.50	533.20	530.10	521.90
3	0	2542.10	1834.10	1339.40	2363.40	2363.50	2363.50	598.30	598.80	585.80
	10K	2292.10	1806.40	1381.50	2363.50	2363.50	2363.50	533.20	530.10	521.90
4	0	2542.10	1834.10	1339.40	2363.40	2363.50	2363.50	598.30	598.80	585.80
	10K	2292.10	1806.40	1381.50	2363.50	2363.50	2363.50	533.20	530.10	521.90
5	0	2466.80	1819.50	1339.40	2262.60	2343.60	2363.50	582.50	595.60	585.80
	10K	2039.50	1563.70	1249.20	1941.30	1997.50	2126.20	462.40	469.50	481.90
6	0	1869.90	1330.10	1046.20	1598.70	1684.60	1852.30	482.30	495.00	509.30
	10K	1702.80	1255.20	991.00	1509.30	1561.40	1679.90	394.90	403.10	412.50
7	0	1111.80	762.60	648.80	922.60	1011.30	1202.00	388.20	400.70	418.50
	10K	1244.10	883.30	690.60	1027.50	1082.90	1189.90	322.40	330.60	339.20

Appendix C

Equations of Motion and Aerodynamic Math Model

The equations used to describe the motion of the airplane are nonlinear, six-degree-of-freedom, rigid-body equations referenced to the body-fixed system of axes shown in figure 1. The equations are as follows:

Forces:

$$\dot{u} = rv - qw - g\sin\theta + \frac{F_{X,b}}{m}$$

$$\dot{v} = pw - ru + g\cos\theta\sin\phi + \frac{F_{Y,b}}{m}$$

$$\dot{w} = qu - pv + g\cos\theta\cos\phi + \frac{F_{Z,b}}{m}$$

Moments:

$$\dot{p} = \frac{I_Y - I_Z}{I_X}qr + \frac{I_{XZ}}{I_X}(\dot{r} + pq) + \frac{L_b}{I_X}$$

$$\dot{q} = \frac{I_Z - I_X}{I_Y}pr + \frac{I_{XZ}}{I_Y}\left(r^2 - p^2\right) + \frac{M_b}{I_Y} - \frac{I_{P,LE}}{I_Y}2\pi r n_{LE} + \frac{I_{P,RE}}{I_Y}2\pi r n_{RE}$$

$$\dot{r} = \frac{I_X - I_Y}{I_Z}pq + \frac{I_{XZ}}{I_Z}(\dot{p} - qr) + \frac{N_b}{I_Z} + \frac{I_{P,LE}}{I_Z}2\pi q n_{LE} - \frac{I_{P,RE}}{I_Z}2\pi q n_{RE}$$

The force and moment terms $F_{X,b}$, $F_{Y,b}$, $F_{Z,b}$, L_b, M_b, and N_b are a combination of aerodynamic and thrust effects. The term in the $\dot{q}$ and $\dot{r}$ equations containing $I_{P,LE}$ and $I_{P,RE}$ are gyroscopic terms involving a combination of the propeller, gear-box, and engine rotating components. (The engines are identical and rotate in the same direction; the propellers rotate in opposite directions.) Auxiliary equations include

$$\alpha = \tan^{-1}\frac{w}{u}$$

$$\beta = \sin^{-1}\frac{v}{V}$$

$$V = \sqrt{u^2 + v^2 + w^2}$$

$$a_z = -qu + pv - g\cos\theta\cos\phi + \dot{w}$$

In calculating the external forces, use was made of wind tunnel measurements obtained in the stability-axis system. The following transformation

$$\begin{bmatrix} F_{X,b} \\ F_{Y,b} \\ F_{Z,b} \end{bmatrix} = \begin{bmatrix} \cos\alpha & 0 & -\sin\alpha \\ 0 & 1 & 0 \\ \sin\alpha & 0 & \cos\alpha \end{bmatrix} \begin{bmatrix} F_{X,s} \\ F_{Y,s} \\ F_{Z,s} \end{bmatrix}$$

provides the forces for the equations of motion. The subscript s signifies the stability-axis system. In addition, coefficients, rather than forces and moments, were used in the following equations:

$$F_{X,s} = -C_{D,s}q_\infty S_w$$

$$F_{Y,s} = C_{Y,s}q_\infty S_w$$

$$F_{Z,s} = -C_{L,s}q_\infty S_w$$

$$L_b = C_{l,b}q_\infty S_w b$$

$$M_b = C_{m,b}q_\infty S_w \bar{c}_w$$

$$N_b = C_{n,b}q_\infty S_w b$$

Finally, each of the six aerodynamic coefficients for calculation purposes was divided into two parts as follows:

$$C_{D,s} = C'_{D,\text{st}} + C'_{D,\text{dyn}}$$

$$C_{Y,s} = C'_{Y,\text{st}} + C'_{Y,\text{dyn}}$$

$$C_{L,s} = C'_{L,\text{st}} + C'_{L,\text{dyn}}$$

$$C_{l,b} = C'_{l,\text{st}} + C'_{l,\text{dyn}}$$

$$C_{m,b} = C'_{m,\text{st}} + C'_{m,\text{dyn}}$$

$$C_{n,b} = C'_{n,\text{st}} + C'_{n,\text{dyn}}$$

where the subscript st refers to static and dyn refers to dynamic . The static and dynamic designations are used to facilitate transferring the data to different center-of-gravity locations. The transfer equations only permit c.g. movement fore and aft along the longitudinal body axis and were obtained from reference 23. To transfer the static terms, the following equations apply:

$$C'_{L,\text{st}} = C_{L,\text{st}}$$

$$C'_{D,\text{st}} = C_{D,\text{st}}$$

$$C'_{m,\text{st}} = C_{m,\text{st}} - C_{L,\text{st}}\frac{\Delta\bar{x}}{\bar{c}_w}\cos\alpha - C_{D,\text{st}}\frac{\Delta\bar{x}}{\bar{c}_w}\sin\alpha$$

$$C'_{Y,\text{st}} = C_{Y,\text{st}}$$

$$C'_{n,\text{st}} = C_{n,\text{st}} - \frac{\Delta\bar{x}}{b_w}C_{Y,\text{st}}$$

$$C'_{l,\text{st}} = C_{l,\text{st}}$$

where $\Delta\bar{x}$ is the distance of the new c.g. along the body X_B axis forward (positive) of the $0.25\bar{c}_w$ position. To transfer the dynamic terms, each individual component comprising the dynamic term must be transferred individually. The transfer equations are listed with each individual term.

Each of the static and dynamic terms consists of the summation of several individual elements. The math model uses tables of aerodynamic coefficients and stability derivatives as functions of either one or two variables usually angle of attack α and thrust coefficient C_T. In some situations at low forward speed, C_T can exceed the maximum value listed in aerodynamic tables. Therefore, prior to data table entry the C_T value was limited to the maximum tabulated.

To permit examining the engine-out conditions with either a failed left or right engine, most static terms contain a direct thrust input for each engine. The corresponding power-induced aerodynamic contributions were designated through the use of subscripts LE and RE (left engine and right engine, respectively). The subscript NE designates the basic data values for no engine operating and propellers removed. Thus, for the situation of a failed engine and feathered propeller, negative values of C_T are obtained. Aerodynamic power-induced effects were not included in the dynamic terms because of the unreliability of such estimates. Since Mach numbers up to 0.6 have been experienced in flight tests of the ATPTB aircraft, a first-order Prandtl-Glauert compressibility factor ($B = \sqrt{1 - M^2}$) was included in the math model. This factor was used to modify certain static and dynamic terms. An option was provided in the program to permit the console operator to either include or eliminate this factor.

The various elements comprising each of the static and dynamic terms are presented on the following pages. The expression for each of the six static coefficients has a coefficient with the subscript 0. For these terms, the sideslip angle β is 0° as are all control surface deflections; that is,

$$\beta = \delta_e = \delta_{a,L} = \delta_{a,R} = \delta_r = \delta_f = 0^\circ$$

In addition, the speed brake and landing gear are retracted ($\delta_{SB} = \delta_{LG} = 0$) and the vehicle is located out of ground effect.

In the summation of terms in the static coefficients for lift, drag, and pitching moments, incremental terms are used to adjust the values for the effect of sideslip. The incremental corrections were obtained simply by subtracting low-speed wind tunnel propeller-off values at zero sideslip from those at sideslip for the model configuration with zero control and flap deflection. These values are tabulated as function of α for $\beta = 0^\circ$, $\beta = \pm 10^\circ$, and $\beta = \pm 20^\circ$. The incremental scheme was used since most of the wind tunnel data for the other terms, such as the contributions due to elevator deflection and flap deflection, were obtained at zero sideslip. Thus, the sideslip effect, which couples the lateral motion with the longitudinal equations, is only approximate. Nevertheless, although inexact, the scheme is believed to provide a large part of the coupling effect. Power-off coupling terms $C_{Y,NE}$, $C_{l,NE}$, $C_{n,NE}$, as functions of α were included in the side-force, rolling-moment, and yawing-moment equations to provide initial departure forces and moments at high angle of attack near the stall. For this particular study, since stall departure was not of interest, all three parameters were set to zero.

Note that the drag coefficient $C_{D,s}$ referred to herein as the drag coefficient along the stability axis was used for convenience in fitting this math model into the existing general aviation simulation program.

Data tables providing numerical values for the individual aerodynamics terms and stability derivatives comprising the three forces and three moments are provided in tables C1 to C6. Constant values were used for some aerodynamic terms appearing in the equations. For convenience, these values are listed as follows:

$$C_{D_{\delta_{LG}}} = 0.0120$$

$$C_{D_{\delta_{SB}}} = 0.0187$$

$$\left(C_{D_q}\right)_{NE} = 0$$

$$\left(C_{D_{\dot{\alpha}}}\right)_{NE} = 0$$

$$C_{Y,NE} = 0$$

$$C_{n,NE} = 0$$

$$C_{l,NE} = 0$$

$$C_{Y_{\delta_{r,\mathrm{tab}}}} = 0.000111$$

$$C_{n_{\delta_{r,\mathrm{tab}}}} = -0.00045$$

$$C_{l_{\delta_{r,\mathrm{tab}}}} = 0.00016$$

Lift:

$$C_{L,\text{st}} = C_{L_0} + (C_{T,LE} + C_{T,RE}) \sin\alpha + C_{L_{\delta_e}} \delta_e + C_{L_{i_t}} i_t + C_{L_{\delta_f}} \delta_f + \Delta C_{L,\beta} + \Delta C_{L,GE} C_{L_1}$$

where

$$C_{L_0} = BC_{L,NE} + \Delta C_{L,LE} + \Delta C_{L,RE}$$

$$C_{L_{i_t}} = B\left(C_{L_{i_t}}\right)_{NE} + \left(\Delta C_{L_{i_t}}\right)_{LE} + \left(\Delta C_{L_{i_t}}\right)_{RE}$$

$$C_{L_{\delta_e}} = B\left(C_{L_{\delta_e}}\right)_{NE} + \left(\Delta C_{L_{\delta_e}}\right)_{RE} + \left(\Delta C_{L_{\delta_e}}\right)_{LE}$$

$$C_{L_{\delta_f}} = B\left(C_{L_{\delta_f}}\right)_{NE} + \left(\Delta C_{L_{\delta_f}}\right)_{LE} + \left(\Delta C_{L_{\delta_f}}\right)_{RE}$$

$$C_{L_1} = C_{L_0} + C_{L_{\delta_f}} \delta_f$$

$$C'_{L,\text{dyn}} = C'_{L_q} \frac{q\bar{c}_w}{2V} + C'_{L_{\dot{\alpha}}} \frac{\dot{\alpha}\bar{c}_w}{2V}$$

where

$$C'_{L_q} = BC_{L_q} + \frac{2\,\Delta\bar{x}}{\bar{c}_w} C_{L_\alpha}$$

$$C_{L_q} = B\left(C_{L_q}\right)_{NE}$$

$$C_{L_{\dot{\alpha}}} = B\left(C_{L_{\dot{\alpha}}}\right)_{NE}$$

$$C'_{L_{\dot{\alpha}}} = C_{L_{\dot{\alpha}}}$$

Drag:

$$C_{D,\text{st}} = C_{D_0} + \left(C_{T,LE} + C_{T,RE}\right) \cos\alpha + C_{D_{\delta_e}} \delta_e + C_{D_{i_t}} i_t + \Delta C_{D,\delta_f} + C_{D_{\delta_r}} |\delta_r| + \Delta C_{D\beta} + C_{D_{\delta_{LG}}} \delta_{LG} + \Delta C_{D,GE} C_{L_1} + C_{D_{\delta_{SB}}} \delta_{SB}$$

where

$$C_{D_0} = BC_{D,NE} + \Delta C_{D,LE} + \Delta C_{D,RE}$$

$$C_{D_{\delta_e}} = B\left(C_{D_{\delta_e}}\right)_{NE} + \left(\Delta C_{D_{\delta_e}}\right)_{LE} + \left(\Delta C_{D_{\delta_e}}\right)_{RE}$$

$$C_{D_{i_t}} = B\left(C_{D_{i_t}}\right)_{NE} + \left(\Delta C_{D_{i_t}}\right)_{LE} + \left(\Delta C_{D_{i_t}}\right)_{RE}$$

$$C_{D_{\delta_r}} = B\left(C_{D_{\delta_r}}\right)_{NE} + \left(\Delta C_{D_{\delta_r}}\right)_{LE} + \left(\Delta C_{D_{\delta_r}}\right)_{RE}$$

$$C'_{D,\text{dyn}} = C_{D_q} \frac{q\bar{c}_w}{2V} + C_{D_{\dot{\alpha}}} \frac{\dot{\alpha}\bar{c}_w}{2V}$$

where

$$C_{D_q} = B\left(C_{D_q}\right)_{NE}$$

$$C_{D_{\dot{\alpha}}} = B\left(C_{D_{\dot{\alpha}}}\right)_{NE}$$

Pitching moment:

$$C_{m,\text{st}} = C_{m_0} + \left(C_{T,LE} + C_{T,RE}\right)\frac{z_e}{\bar{c}_w} + C_{m_{\delta_e}}\delta_e + C_{m_{i_t}}i_t + C_{m_{\delta_f}}\delta_f + \Delta C_{m,\beta} + C_{m_{\delta_{LG}}}\delta_{LG} + \Delta C_{m,GE} + C_{L_1} + C_{m_{\delta_{SB}}}\delta_{SB}$$

where

$$\begin{aligned}
C_{m_0} &= BC_{m,NE} + \Delta C_{m,LE} + \Delta C_{m,RE} \\
C_{m_{\delta_e}} &= B\left(C_{m_{\delta_e}}\right)_{NE} + \left(\Delta C_{m_{\delta_e}}\right)_{LE} + \left(\Delta C_{m_{\delta_e}}\right)_{RE} \\
C_{m_{i_t}} &= B\left(C_{m_{i_t}}\right)_{NE} + \left(\Delta C_{m_{i_t}}\right)_{LE} + \left(\Delta C_{m_{i_t}}\right)_{RE} \\
C_{m_{\delta_f}} &= B\left(C_{m_{\delta_f}}\right)_{NE} + \left(\Delta C_{m_{\delta_f}}\right)_{LE} + \left(\Delta C_{m_{\delta_f}}\right)_{RE} \\
C'_{m,\text{dyn}} &= C'_{m_q}\frac{q\bar{c}_w}{2V} + C'_{m_{\dot{\alpha}}}\frac{\dot{\alpha}\bar{c}_w}{2V}
\end{aligned}$$

where

$$\begin{aligned}
C'_{m_q} &= C_{m_q} - \frac{\Delta\bar{x}}{\bar{c}_w}C_{L_q} + \frac{2\,\Delta\bar{x}}{\bar{c}_w}C_{m_\alpha} - 2\left(\frac{\Delta\bar{x}}{\bar{c}_w}\right)^2 C_{L_\alpha} \\
C'_{m_{\dot{\alpha}}} &= C_{m_{\dot{\alpha}}} - \frac{\Delta\bar{x}}{\bar{c}_w}C_{L_{\dot{\alpha}}} \\
C_{m_{\dot{\alpha}}} &= B\left(C_{m_{\dot{\alpha}}}\right)_{NE} \\
C_{m_q} &= B\left(C_{m_q}\right)_{NE}
\end{aligned}$$

Yawing moment:

$$C_{n,\text{st}} = C_{n_0} + \left(C_{T,LE} + C_{T,RE}\right)\frac{y_e}{b_w} + C_{n_\beta}\beta + C_{n_{\delta_r}}\delta_r + C_{n_{\delta_{a,L}}}\delta_{a,L} + C_{n_{\delta_{a,R}}}\delta_{a,R} + C_{n_{\delta_{r,\text{tab}}}}\delta_{r,\text{tab}}$$

where

$$\begin{aligned}
C_{n_0} &= BC_{n,NE} + \Delta C_{n,LE} + \Delta C_{n,RE} \\
C_{n_\beta} &= B\left(C_{n_\beta}\right)_{NE} + \left(\Delta C_{n_\beta}\right)_{LE} + \left(\Delta C_{n_\beta}\right)_{RE} \\
C_{n_{\delta_r}} &= B\left(C_{n_{\delta_r}}\right)_{NE} + \left(\Delta C_{n_{\delta_r}}\right)_{LE} + \left(\Delta C_{n_{\delta_r}}\right)_{RE} \\
C_{n_{\delta_{a,L}}} &= \frac{1}{B}\left(C_{n_{\delta_{a,L}}}\right)_{NE} \\
C_{n_{\delta_{a,R}}} &= \frac{1}{B}\left(C_{n_{\delta_{a,R}}}\right)_{NE} \\
C'_{n,\text{dyn}} &= C'_{n_p}\frac{pb_w}{2V} + C'_{n_r}\frac{rb_w}{2V}
\end{aligned}$$

where

$$C'_{n_r} = C_{n_r} - \frac{\Delta\bar{x}}{b_w} C_{Y_r} - \frac{2\,\Delta\bar{x}}{b_w} C_{n_\beta} + 2\left(\frac{\Delta\bar{x}}{b_w}\right)^2 C_{Y_\beta}$$

$$C_{n_r} = B\,(C_{n_r})_{NE}$$

$$C'_{n_p} = C_{n_p} - \frac{\Delta\bar{x}}{b_w} C_{Y_p}$$

$$C_{n_p} = \frac{1}{B}\left(C_{n_p}\right)_{NE}$$

Rolling moment:

$$C_{l,\text{st}} = C_{l_0} + C_{l_\beta}\beta + C_{l_{\delta_r}}\delta_r + C_{l_{\delta_{a,L}}}\delta_{a,L} + C_{l_{\delta_{a,R}}}\delta_{a,R} + C_{l_{\delta_{r,\text{tab}}}}\delta_{r,\text{tab}}$$

where

$$C_{l_0} = BC_{l,NE} + \Delta C_{l,LE}\left(1 + \frac{\delta_f}{35°}\right) + \Delta C_{l,RE}\left(1 + \frac{\delta_f}{35°}\right)$$

$$C_{l_\beta} = B\left(C_{l_\beta}\right)_{NE} + \left(\Delta C_{l_\beta}\right)_{LE} + \left(\Delta C_{l_\beta}\right)_{RE}$$

$$C_{l_{\delta_r}} = B\left(C_{l_{\delta_r}}\right)_{NE} + \left(\Delta C_{l_{\delta_r}}\right)_{LE} + \left(\Delta C_{l_{\delta_r}}\right)_{RE}$$

$$C_{l_{\delta_{a,L}}} = B\left(C_{l_{\delta_{a,L}}}\right)_{NE}$$

$$C_{l_{\delta_{a,R}}} = B\left(C_{l_{\delta_{a,R}}}\right)_{NE}$$

$$C'_{l,\text{dyn}} = C'_{l_p}\frac{pb_w}{2V} + C'_{l_r}\frac{rb_w}{2V}$$

where

$$C'_{l_p} = C_{l_p}$$

$$C_{l_p} = B\left(C_{l_p}\right)_{NE}$$

$$C'_{l_r} = C_{l_r} - \frac{2\,\Delta\bar{x}}{b_w} C_{l_\beta}$$

$$C_{l_r} = \frac{1}{B}\left(C_{l_r}\right)_{NE}$$

Side force:

$$C_{Y,\text{st}} = C_{Y_0} + C_{Y_\beta}\beta + C_{Y_{\delta_r}}\delta_r + C_{Y_{\delta_{a,L}}}\delta_{a,L} + C_{Y_{\delta_{a,R}}}\delta_{a,R} + C_{Y_{\delta_{r,\text{tab}}}}\delta_{r,\text{tab}}$$

where

$$C_{Y_0} = BC_{Y,NE} + \Delta C_{Y,LE} + \Delta C_{Y,RE}$$

$$C_{Y_\beta} = B\left(C_{Y_\beta}\right)_{NE} + \left(\Delta C_{Y_\beta}\right)_{LE} + \left(\Delta C_{Y_\beta}\right)_{RE}$$

$$C_{Y_{\delta_r}} = B\left(C_{Y_{\delta_r}}\right)_{NE} + \left(\Delta C_{Y_{\delta_r}}\right)_{LE} + \left(\Delta C_{Y_{\delta_r}}\right)_{RE}$$

$$C_{Y_{\delta_{a,L}}} = B\left(C_{Y_{\delta_{a,L}}}\right)_{NE}$$

$$C_{Y_{\delta_{a,R}}} = B\left(C_{Y_{\delta_{a,R}}}\right)_{NE}$$

$$C'_{Y,\text{dyn}} = C'_{Y_p}\frac{pb_w}{2V} + C'_{Y_r}\frac{rb_w}{2V}$$

where

$$C'_{Y_p} = C_{Y_p}$$

$$C_{Y_p} = B\left(C_{Y_p}\right)_{NE}$$

$$C'_{Y_r} = C_{Y_r} - \frac{2\,\Delta\bar{x}}{b_w}C_{Y_\beta}$$

$$C_{Y_r} = B\left(C_{Y_r}\right)_{NE}$$

Table C1. Lift-Coefficient Data

$\Delta C_{L,LE}, \Delta C_{L,RE}$

	C_T			
α	$(-0.00710$	0.00000	0.03540	0.20140)
−8.00000	−0.00614	0.00000	−0.00172	−0.01842
−4.00000	−0.00240	0.00000	0.00357	−0.00407
0.00000	−0.00043	0.00000	0.00658	0.03073
4.00000	0.00090	0.00000	0.00694	0.02336
8.00000	0.00286	0.00000	0.00645	0.03235
12.00000	0.00211	0.00000	0.00577	0.03426
14.00000	0.00164	0.00000	0.00636	0.03426
16.00000	0.00575	0.00000	0.00636	0.03426
20.00000	0.00990	0.00000	0.10387	0.26600
24.00000	0.00578	0.00000	0.11950	0.28713
28.00000	0.00219	0.00000	0.11024	0.25893
32.00000	0.00018	0.00000	0.09766	0.22656
36.00000	−0.00183	0.00000	0.08519	0.19484

$C_{L,NE}$

α	$C_{L,NE}$
−8.0000	−0.6177
−4.0000	−0.2142
0.0000	0.1958
4.0000	0.5952
8.0000	0.9793
12.0000	1.3277
14.0000	1.4602
16.0000	1.5927
20.0000	0.8191
24.0000	0.8322
28.0000	0.8653
32.0000	0.8982
36.0000	0.9310

$\left(\Delta C_{L_{\delta_e}}\right)_{RE}, \left(\Delta C_{L_{\delta_e}}\right)_{LE}$

	C_T			
α	$(-0.00710$	0.00000	0.03540	0.20140)
−8.00000	−0.00004	0.00000	−0.00014	0.00002
−4.00000	−0.00003	0.00000	−0.00004	0.00004
0.00000	−0.00005	0.00000	−0.00007	0.00001
4.00000	−0.00004	0.00000	−0.00013	0.00003
8.00000	−0.00003	0.00000	−0.00015	0.00027
12.00000	−0.00035	0.00000	−0.00041	0.00065
14.00000	−0.00048	0.00000	0.00006	0.00121
16.00000	0.00039	0.00000	0.00057	0.00257
20.00000	−0.00067	0.00000	0.00189	0.00434
24.00000	−0.00006	0.00000	0.00085	0.00350
28.00000	0.00012	0.00000	0.00074	0.00277
32.00000	0.00030	0.00000	0.00063	0.00253
36.00000	0.00047	0.00000	0.00052	0.00228

Table C1. Continued

$\left(C_{L_{\delta_e}}\right)_{NE}$

α	$\left(C_{L_{\delta_e}}\right)_{NE}$
−8.0000	0.0071
−4.0000	0.0073
0.0000	0.0075
4.0000	0.0074
8.0000	0.0074
12.0000	0.0075
14.0000	0.0069
16.0000	0.0048
20.0000	0.0025
24.0000	0.0020
28.0000	0.0009
32.0000	−0.0003
36.0000	−0.0014

$\left(\Delta C_{L_{i_t}}\right)_{LE}, \left(\Delta C_{L_{i_t}}\right)_{RE}$

	C_T			
α	(−0.00710	0.00000	0.03540	0.20140)
−8.00000	0.00008	0.00000	−0.00030	−0.00068
−4.00000	0.00012	0.00000	−0.00047	−0.00056
0.00000	0.00008	0.00000	−0.00030	−0.00078
4.00000	0.00008	0.00000	−0.00032	−0.00094
8.00000	0.00012	0.00000	−0.00048	−0.00069
12.00000	0.00006	0.00000	−0.00024	−0.00030
14.00000	−0.00003	0.00000	0.00014	−0.00015
16.00000	−0.00042	0.00000	0.00167	0.00103
20.00000	−0.00047	0.00000	0.00190	0.00396
24.00000	−0.00033	0.00000	0.00131	0.00338
28.00000	−0.00033	0.00000	0.00131	0.00319
32.00000	−0.00032	0.00000	0.00130	0.00314
36.00000	−0.00032	0.00000	0.00128	0.00324

$\left(C_{L_{i_t}}\right)_{NE}$

α	$\left(C_{L_{i_t}}\right)_{NE}$
−8.0000	0.0104
−4.0000	0.0126
0.0000	0.0135
4.0000	0.0136
8.0000	0.0133
12.0000	0.0127
14.0000	0.0124
16.0000	0.0097
20.0000	0.0019
24.0000	0.0022
28.0000	0.0020
32.0000	0.0017
36.0000	0.0014

Table C1. Continued

$\left(\Delta C_{L_{\delta_f}}\right)_{LE}$, $\left(\Delta C_{L_{\delta_f}}\right)_{RE}$

	C_T			
α	$(-0.00710$	0.00000	0.03540	0.20140)
−8.00000	0.00003	0.00000	−0.00010	0.00004
−4.00000	0.00000	0.00000	0.00000	0.00007
0.00000	0.00001	0.00000	−0.00003	0.00006
4.00000	0.00001	0.00000	−0.00005	−0.00006
8.00000	−0.00002	0.00000	0.00009	0.00001
12.00000	0.00001	0.00000	−0.00004	0.00005
14.00000	0.00054	0.00000	−0.00217	−0.00168
16.00000	0.00000	0.00000	0.00002	0.00007
20.00000	−0.00025	0.00000	0.00099	0.00192
24.00000	−0.00017	0.00000	0.00066	0.00117
28.00000	−0.00007	0.00000	0.00028	0.00074
32.00000	−0.00004	0.00000	0.00014	0.00051
36.00000	−0.00002	0.00000	0.00008	0.00026

$\left(C_{L_{\delta_f}}\right)_{NE}$

α	$\left(C_{L_{\delta_f}}\right)_{NE}$
−8.0000	0.0169
−4.0000	0.0176
0.0000	0.0177
4.0000	0.0178
8.0000	0.0182
12.0000	0.0181
14.0000	0.0158
16.0000	0.0140
20.0000	0.0080
24.0000	0.0066
28.0000	0.0061
32.0000	0.0060
36.0000	0.0059

$\Delta C_{L,\beta}$

	β				
α	$(-20.00000$	−10.00000	0.00000	10.00000	20.00000)
−8.00000	0.01200	0.00500	0.00000	0.00500	0.01200
−4.00000	0.00550	0.00200	0.00000	0.00200	0.00550
0.00000	−0.00600	−0.00200	0.00000	−0.00200	−0.00600
4.00000	−0.01800	−0.00600	0.00000	−0.00600	−0.01800
8.00000	−0.03000	−0.01000	0.00000	−0.01000	−0.03000
12.00000	−0.04200	−0.01400	0.00000	−0.01400	−0.04200
14.00000	−0.04050	−0.01350	0.00000	−0.01350	−0.04050
16.00000	−0.03600	−0.01200	0.00000	−0.01200	−0.03600
20.00000	−0.02700	−0.00900	0.00000	−0.00900	−0.02700
24.00000	−0.01800	−0.00600	0.00000	−0.00600	−0.01800
28.00000	−0.00900	−0.00300	0.00000	−0.00300	−0.00900
32.00000	0.00000	0.00000	0.00000	0.00000	0.00000
36.00000	0.00000	0.00000	0.00000	0.00000	0.00000

Table C1. Concluded

$\Delta C_{L,GE}$

	Flaps		
Height	(0.00000	20.00000	35.00000)
0.00000	0.15000	0.15000	0.10000
10.00000	0.04000	0.06000	0.03400
20.00000	0.01500	0.02600	0.01250
30.00000	0.00600	0.01000	0.00500
40.00000	0.00200	0.00400	0.00150
50.00000	0.00050	0.00100	0.00020
75.00000	0.00000	0.00000	0.00000
100.00000	0.00000	0.00000	0.00000
125.00000	0.00000	0.00000	0.00000

$\left(C_{L_q}\right)_{NE}$

α	$\left(C_{L_q}\right)_{NE}$
−8.0000	8.0000
−4.0000	8.0000
0.0000	8.0000
4.0000	8.0000
8.0000	8.0000
12.0000	8.0000
14.0000	7.6700
16.0000	7.3400
20.0000	6.6800
24.0000	6.0200
28.0000	5.3600
32.0000	4.7000
36.0000	4.0400

$\left(C_{L_{\dot{\alpha}}}\right)_{NE}$

α	$\left(C_{L_{\dot{\alpha}}}\right)_{NE}$
−8.0000	1.3440
−4.0000	1.3440
0.0000	1.3440
4.0000	1.3440
8.0000	1.3440
12.0000	1.3440
14.0000	1.3440
16.0000	1.3440
20.0000	1.3440
24.0000	1.3440
28.0000	1.3440
32.0000	1.3440
36.0000	1.3440

C_{L_α}

α	C_{L_α}
−8.0000	5.6211
−4.0000	5.6211
0.0000	5.6211
4.0000	5.6211
8.0000	5.6211
12.0000	5.6211
14.0000	5.6211

Table C2. Drag-Coefficient Data

$\Delta C_{D,LE}, \Delta C_{D,RE}$

	C_T			
α	$(-0.00710$	0.00000	0.03540	0.20140)
−8.00000	0.00488	0.00000	−0.00153	−0.02103
−4.00000	0.00468	0.00000	0.00007	−0.01435
0.00000	0.00431	0.00000	0.00431	−0.00875
4.00000	0.00386	0.00000	0.00775	0.00017
8.00000	0.00416	0.00000	0.01125	−0.00333
12.00000	0.00462	0.00000	0.01319	−0.00445
14.00000	0.00098	0.00000	0.01121	−0.00872
16.00000	−0.00308	0.00000	−0.01523	−0.00704
20.00000	−0.00083	0.00000	0.00711	0.02147
24.00000	0.00219	0.00000	0.01552	0.03639
28.00000	−0.00519	0.00000	0.00384	0.02473
32.00000	−0.01049	0.00000	−0.00895	0.00313
36.00000	−0.01574	0.00000	−0.02186	−0.00365

$C_{D,NE}$

α	$C_{D,NE}$
−8.0000	0.0532
−4.0000	0.0325
0.0000	0.0252
4.0000	0.0331
8.0000	0.0556
12.0000	0.0909
14.0000	0.1233
16.0000	0.2300
20.0000	0.3513
24.0000	0.4206
28.0000	0.5198
32.0000	0.6189
36.0000	0.7180

$\left(\Delta C_{D_{\delta_e}}\right)_{LE}, \left(\Delta C_{D_{\delta_e}}\right)_{RE}$

	C_T			
α	$(-0.00710$	0.00000	0.03540	0.20140)
−8.00000	−0.00003	0.00000	−0.00014	−0.00073
−4.00000	−0.00002	0.00000	−0.00025	−0.00068
0.00000	−0.00006	0.00000	−0.00032	−0.00062
4.00000	−0.00002	0.00000	−0.00019	−0.00052
8.00000	−0.00001	0.00000	−0.00021	−0.00032
12.00000	−0.00006	0.00000	−0.00021	−0.00026
14.00000	−0.00004	0.00000	−0.00022	−0.00012
16.00000	0.00001	0.00000	−0.00009	0.00025
20.00000	0.00006	0.00000	0.00018	0.00122
24.00000	−0.00016	0.00000	0.00026	0.00141
28.00000	−0.00012	0.00000	0.00001	0.00134
32.00000	−0.00009	0.00000	−0.00007	0.00094
36.00000	−0.00005	0.00000	−0.00005	0.00069

Table C2. Continued

$\left(C_{D_{\delta_e}}\right)_{NE}$

α	$\left(C_{D_{\delta_e}}\right)_{NE}$
−8.0000	−0.0007
−4.0000	−0.0003
0.0000	0.0000
4.0000	0.0003
8.0000	0.0006
12.0000	0.0011
14.0000	0.0012
16.0000	0.0012
20.0000	0.0010
24.0000	0.0009
28.0000	0.0008
32.0000	0.0006
36.0000	0.0005

$\left(\Delta C_{D_{i_t}}\right)_{LE}, \left(\Delta C_{D_{i_t}}\right)_{RE}$

	C_T			
α	(−0.00710	0.00000	0.03540	0.20140)
−8.00000	−0.00001	0.00000	0.00003	0.00000
−4.00000	−0.00002	0.00000	0.00009	0.00014
0.00000	0.00001	0.00000	−0.00004	0.00005
4.00000	0.00005	0.00000	−0.00019	−0.00004
8.00000	0.00002	0.00000	−0.00008	0.00014
12.00000	0.00003	0.00000	−0.00011	0.00031
14.00000	0.00008	0.00000	−0.00032	0.00017
16.00000	0.00006	0.00000	−0.00025	0.00077
20.00000	−0.00015	0.00000	0.00060	0.00162
24.00000	−0.00013	0.00000	0.00051	0.00243
28.00000	−0.00012	0.00000	0.00050	0.00208
32.00000	−0.00012	0.00000	0.00047	0.00176
36.00000	−0.00011	0.00000	0.00045	0.00143

$\left(C_{D_{i_t}}\right)_{NE}$

α	$\left(C_{D_{i_t}}\right)_{NE}$
−8.0000	−0.0032
−4.0000	−0.0021
0.0000	−0.0009
4.0000	0.0001
8.0000	0.0007
12.0000	0.0015
14.0000	0.0025
16.0000	0.0023
20.0000	0.0022
24.0000	0.0016
28.0000	0.0013
32.0000	0.0010
36.0000	0.0006

Table C2. Continued

$\Delta C_{D,\delta_f}$

	Flap deflection, deg						
α	(0.000	6.000	12.000	18.000	24.000	29.000	35.000)
−8.00000	0.00000	−0.00596	−0.00758	−0.00486	0.00220	0.01141	0.02643
−4.00000	0.00000	−0.00130	0.00147	0.00832	0.01923	0.03143	0.04980
0.00000	0.00000	0.00322	0.01007	0.02056	0.03469	0.04924	0.07004
4.00000	0.00000	0.00824	0.01953	0.03388	0.05128	0.06811	0.09111
8.00000	0.00000	0.01250	0.02753	0.04508	0.06516	0.08382	0.10853
12.00000	0.00000	0.01566	0.03365	0.05399	0.07667	0.09735	0.12432
14.00000	0.00000	0.01908	0.03909	0.06003	0.08189	0.10082	0.12438
16.00000	0.00000	0.01374	0.03182	0.05425	0.08102	0.10665	0.14138
20.00000	0.00000	0.02859	0.05731	0.08613	0.11508	0.13929	0.16845
24.00000	0.00000	0.03314	0.06496	0.09545	0.12462	0.14791	0.17464
28.00000	0.00000	0.03516	0.06891	0.10125	0.13217	0.15685	0.18518
32.00000	0.00000	0.02315	0.04903	0.07764	0.10897	0.13716	0.17349
36.00000	0.00000	0.01015	0.02741	0.05178	0.08328	0.11495	0.15949

$\Delta C_{D\beta}$

	β				
α	(−20.00000	−10.00000	0.00000	10.00000	20.00000)
−8.00000	−0.01800	−0.00600	0.00000	−0.00600	−0.01800
−4.00000	−0.01800	−0.00600	0.00000	−0.00600	−0.01800
0.00000	−0.01800	−0.00600	0.00000	−0.00600	−0.01800
4.00000	−0.01800	−0.00600	0.00000	−0.00600	−0.01800
8.00000	−0.01800	−0.00600	0.00000	−0.00600	−0.01800
12.00000	−0.01800	−0.00600	0.00000	−0.00600	−0.01800
14.00000	−0.01800	−0.00600	0.00000	−0.00600	−0.01800
16.00000	−0.01500	−0.00500	0.00000	−0.00500	−0.01500
20.00000	−0.01200	−0.00400	0.00000	−0.00400	−0.01200
24.00000	−0.01200	−0.00400	0.00000	−0.00400	−0.01200
28.00000	−0.01200	−0.00400	0.00000	−0.00400	−0.01200
32.00000	−0.01200	−0.00400	0.00000	−0.00400	−0.01200
36.00000	−0.01200	−0.00400	0.00000	−0.00400	−0.01200

$\left(\Delta C_{D_{\delta r}}\right)_{LE}$, $\left(\Delta C_{D_{\delta r}}\right)_{RE}$

	C_T			
α	(−0.00710	0.00000	0.03540	0.20140)
−8.00000	−0.00004	0.00000	0.00004	0.00035
−4.00000	−0.00006	0.00000	0.00006	0.00033
0.00000	−0.00004	0.00000	0.00004	0.00040
4.00000	−0.00004	0.00000	0.00004	0.00050
8.00000	−0.00002	0.00000	0.00002	0.00049
12.00000	−0.00010	0.00000	0.00010	0.00047
14.00000	−0.00002	0.00000	0.00002	0.00042
16.00000	−0.00008	0.00000	0.00008	0.00039
20.00000	−0.00002	0.00000	0.00002	0.00024
24.00000	0.00000	0.00000	0.00000	0.00021
28.00000	−0.00004	0.00000	0.00004	0.00031
32.00000	−0.00008	0.00000	0.00008	0.00040
36.00000	−0.00011	0.00000	0.00011	0.00049

Table C2. Concluded

$\left(C_{D_{\delta r}}\right)_{NE}$

α	$\left(C_{D_{\delta r}}\right)_{NE}$
−8.0000	0.0007
−4.0000	0.0007
0.0000	0.0006
4.0000	0.0004
8.0000	0.0005
12.0000	0.0004
14.0000	0.0004
16.0000	0.0004
20.0000	0.0003
24.0000	0.0002
28.0000	−0.0001
32.0000	−0.0003
36.0000	−0.0006

$\Delta C_{D,GE}$

	Flaps		
Height	(0.00000	20.00000	35.00000)
0.00000	0.01300	0.01300	−0.01300
10.00000	0.01250	0.01300	−0.01350
20.00000	0.01000	0.01250	−0.01400
30.00000	0.00700	0.00850	−0.01600
40.00000	0.00300	0.00400	−0.01600
50.00000	0.00000	0.00000	−0.01250
75.00000	0.00000	0.00000	0.00000
100.00000	0.00000	0.00000	0.00000
125.00000	0.00000	0.00000	0.00000

$\left(\Delta C_{D_q}\right)_{NE}$

α	$\left(\Delta C_{D_q}\right)_{NE}$
−8.0000	0.0000
−4.0000	0.0000
0.0000	0.0000
4.0000	0.0000
8.0000	0.0000
12.0000	0.0000
14.0000	0.0000
16.0000	0.0000
20.0000	0.0000
24.0000	0.0000
28.0000	0.0000
32.0000	0.0000
36.0000	0.0000

$\left(\Delta C_{D_{\dot{\alpha}}}\right)_{NE}$

α	$\left(\Delta C_{D_{\dot{\alpha}}}\right)_{NE}$
−8.0000	0.0000
−4.0000	0.0000
0.0000	0.0000
4.0000	0.0000
8.0000	0.0000
12.0000	0.0000
14.0000	0.0000
16.0000	0.0000
20.0000	0.0000
24.0000	0.0000
28.0000	0.0000
32.0000	0.0000
36.0000	0.0000

Table C3. Pitching-Moment Data

$\Delta C_{m,LE}$, $\Delta C_{m,RE}$

	C_T			
α	(−0.00710	0.00000	0.03540	0.20140)
−8.00000	0.01016	0.00000	0.00486	0.00669
−4.00000	0.01051	0.00000	0.00721	0.00904
0.00000	0.00773	0.00000	0.00843	0.01676
4.00000	0.00677	0.00000	0.01047	0.02030
8.00000	0.00626	0.00000	0.01296	−0.00271
12.00000	0.00637	0.00000	0.01457	−0.07560
14.00000	0.00955	0.00000	0.01475	−0.09292
16.00000	0.01704	0.00000	−0.02876	−0.08793
20.00000	0.00737	0.00000	−0.08943	−0.20760
24.00000	0.01335	0.00000	−0.09745	−0.28112
28.00000	0.00154	0.00000	−0.07926	−0.24693
32.00000	−0.01868	0.00000	−0.05948	−0.21815
36.00000	−0.03888	0.00000	−0.03968	−0.26935

$C_{m,NE}$

α	$C_{m,NE}$
−8.0000	0.2849
−4.0000	0.1762
0.0000	0.0718
4.0000	−0.0293
8.0000	−0.1303
12.0000	−0.2285
14.0000	−0.2779
16.0000	−0.3000
20.0000	−0.2685
24.0000	−0.1555
28.0000	−0.0708
32.0000	0.0136
36.0000	0.0980

$\left(\Delta C_{m_{\delta_e}}\right)_{LE}$, $\left(\Delta C_{m_{\delta_e}}\right)_{RE}$

	C_T			
α	(−0.00710	0.00000	0.03540	0.20140)
−8.00000	0.00020	0.00000	0.00022	0.00016
−4.00000	0.00026	0.00000	0.00020	−0.00006
0.00000	0.00047	0.00000	0.00032	0.00007
4.00000	0.00042	0.00000	0.00026	0.00000
8.00000	0.00042	0.00000	0.00030	−0.00009
12.00000	0.00055	0.00000	0.00020	−0.00033
14.00000	0.00075	0.00000	0.00008	−0.00064
16.00000	0.00135	0.00000	−0.00122	−0.00393
20.00000	0.00099	0.00000	−0.00457	−0.01107
24.00000	0.00066	0.00000	−0.00263	−0.01050
28.00000	0.00023	0.00000	−0.00145	−0.00836
32.00000	0.00029	0.00000	−0.00079	−0.00665
36.00000	0.00040	0.00000	−0.00045	−0.00571

Table C3. Continued

$\left(C_{m_{\delta_e}}\right)_{NE}$

α	$\left(C_{m_{\delta_e}}\right)_{NE}$
−8.0000	−0.0255
−4.0000	−0.0269
0.0000	−0.0278
4.0000	−0.0280
8.0000	−0.0279
12.0000	−0.0276
14.0000	−0.0272
16.0000	−0.0268
20.0000	−0.0131
24.0000	−0.0100
28.0000	−0.0065
32.0000	−0.0040
36.0000	−0.0016

$\left(\Delta C_{m_{i_t}}\right)_{LE}$, $\left(\Delta C_{m_{i_t}}\right)_{RE}$

	C_T			
α	(−0.00710	0.00000	0.03540	0.20140)
−8.00000	−0.00005	0.00000	0.00021	0.00053
−4.00000	−0.00002	0.00000	0.00008	0.00007
0.00000	0.00000	0.00000	0.00002	0.00112
4.00000	0.00001	0.00000	−0.00003	0.00136
8.00000	0.00000	0.00000	0.00000	0.00010
12.00000	0.00004	0.00000	−0.00018	−0.00035
14.00000	0.00014	0.00000	−0.00058	−0.00119
16.00000	0.00103	0.00000	−0.00412	−0.00838
20.00000	0.00131	0.00000	−0.00525	−0.01490
24.00000	0.00123	0.00000	−0.00491	−0.01594
28.00000	0.00069	0.00000	−0.00278	−0.01358
32.00000	0.00052	0.00000	−0.00207	−0.00959
36.00000	0.00057	0.00000	−0.00230	−0.00824

$\left(C_{m_{i_t}}\right)_{NE}$

α	$\left(C_{m_{i_t}}\right)_{NE}$
−8.0000	−0.0391
−4.0000	−0.0447
0.0000	−0.0487
4.0000	−0.0492
8.0000	−0.0493
12.0000	−0.0493
14.0000	−0.0486
16.0000	−0.0450
20.0000	−0.0241
24.0000	−0.0165
28.0000	−0.0128
32.0000	−0.0099
36.0000	−0.0074

Table C3. Continued

$\left(\Delta C_{m_{\delta_f}}\right)_{LE}$, $\left(\Delta C_{m_{\delta_f}}\right)_{RE}$

	C_T			
α	(−0.00710	0.00000	0.03540	0.20140)
−8.00000	0.00004	0.00000	−0.00015	−0.00032
−4.00000	0.00004	0.00000	−0.00014	−0.00031
0.00000	0.00003	0.00000	−0.00013	−0.00030
4.00000	0.00003	0.00000	−0.00013	−0.00027
8.00000	0.00003	0.00000	−0.00013	−0.00026
12.00000	0.00003	0.00000	−0.00011	−0.00047
14.00000	0.00015	0.00000	−0.00058	−0.00066
16.00000	0.00001	0.00000	−0.00005	−0.00020
20.00000	0.00003	0.00000	−0.00012	−0.00025
24.00000	0.00000	0.00000	0.00001	0.00004
28.00000	0.00001	0.00000	−0.00005	−0.00005
32.00000	0.00000	0.00000	−0.00002	−0.00003
36.00000	0.00002	0.00000	−0.00006	−0.00007

$\left(C_{m_{\delta_f}}\right)_{NE}$

α	$\left(C_{m_{\delta_f}}\right)_{NE}$
−8.0000	−0.0017
−4.0000	−0.0016
0.0000	−0.0014
4.0000	−0.0012
8.0000	−0.0009
12.0000	−0.0006
14.0000	−0.0007
16.0000	−0.0007
20.0000	−0.0007
24.0000	0.0004
28.0000	0.0013
32.0000	0.0019
36.0000	0.0027

$\Delta C_{m,\beta}$

	β				
α	(−20.00000	−10.00000	0.00000	10.00000	20.00000)
−8.00000	−0.09000	−0.03000	0.00000	−0.03000	−0.09000
−4.00000	−0.09000	−0.03000	0.00000	−0.03000	−0.09000
0.00000	−0.09000	−0.03000	0.00000	−0.03000	−0.09000
4.00000	−0.09000	−0.03000	0.00000	−0.03000	−0.09000
8.00000	−0.09000	−0.03000	0.00000	−0.03000	−0.09000
12.00000	−0.09000	−0.03000	0.00000	−0.03000	−0.09000
14.00000	−0.09000	−0.03000	0.00000	−0.03000	−0.09000
16.00000	−0.08250	−0.02750	0.00000	−0.02750	−0.08250
20.00000	−0.07500	−0.02500	0.00000	−0.02500	−0.07500
24.00000	−0.06750	−0.02250	0.00000	−0.02250	−0.06750
28.00000	−0.06000	−0.02000	0.00000	−0.02000	−0.06000
32.00000	−0.05250	−0.01750	0.00000	−0.01750	−0.05250
36.00000	−0.04500	−0.01500	0.00000	−0.01500	−0.04500

Table C3. Concluded

$\Delta C_{m,GE}$

α	$\Delta C_{m,GE}$
0.0000	−0.0760
10.0000	−0.0375
20.0000	−0.0220
30.0000	−0.0150
40.0000	−0.0105
50.0000	−0.0075
75.0000	−0.0040
100.0000	−0.0020
125.0000	0.0000

$\left(C_{m_{\dot{\alpha}}}\right)_{NE}$

α	$\left(C_{m_{\dot{\alpha}}}\right)_{NE}$
−8.0000	−4.9918
−4.0000	−4.9918
0.0000	−4.9918
4.0000	−4.9918
8.0000	−4.9918
12.0000	−4.9918
14.0000	−4.9918
16.0000	−4.9918
20.0000	−4.9918
24.0000	−4.9918
28.0000	−4.9918
32.0000	−4.9918
36.0000	−4.9918

C_{m_α}

α	C_{m_α}
−8.0000	−1.4612
−4.0000	−1.4612
0.0000	−1.4612
4.0000	−1.4612
8.0000	−1.4612
12.0000	−1.4612
14.0000	−1.4612

$\left(C_{m_q}\right)_{NE}$

α	$\left(C_{m_q}\right)_{NE}$
−8.0000	−19.5300
−4.0000	−19.5300
0.0000	−19.5300
4.0000	−19.5300
8.0000	−19.5300
12.0000	−19.5300
14.0000	−18.3600
16.0000	−17.1900
20.0000	−14.8400
24.0000	−12.5000
28.0000	−10.1600
32.0000	−7.8100
36.0000	−5.4700

Table C4. Rolling-Moment Coefficient Data

$\Delta C_{l,LE}$

	C_T				
α	$(-0.00710$	0.00000	0.03540	0.11180	0.20140)
−8.00000	0.00000	0.00000	−0.00200	−0.00200	−0.00200
−4.00000	0.00000	0.00000	−0.00160	−0.00160	−0.00160
0.00000	0.00000	0.00000	−0.00113	−0.00113	−0.00113
4.00000	0.00000	0.00000	−0.00080	−0.00080	−0.00080
8.00000	0.00000	0.00000	−0.00050	−0.00050	−0.00050
12.00000	0.00000	0.00000	−0.00090	−0.00090	−0.00090
14.00000	0.00000	0.00000	−0.00090	−0.00090	−0.00090
16.00000	0.00000	0.00000	0.00640	0.01040	0.01440
20.00000	0.00000	0.00000	0.01400	0.02150	0.02890
24.00000	0.00000	0.00000	0.01800	0.02430	0.03050
28.00000	0.00000	0.00000	0.01800	0.02430	0.03050
32.00000	0.00000	0.00000	0.01800	0.02430	0.03050
36.00000	0.00000	0.00000	0.01800	0.02430	0.03050

$\Delta C_{l,RE}$

	C_T				
α	$(-0.00710$	0.00000	0.03540	0.11180	0.20140)
−8.00000	0.00000	0.00000	0.00200	0.00200	0.00200
−4.00000	0.00000	0.00000	0.00160	0.00160	0.00160
0.00000	0.00000	0.00000	0.00113	0.00113	0.00113
4.00000	0.00000	0.00000	0.00080	0.00080	0.00080
8.00000	0.00000	0.00000	0.00050	0.00050	0.00050
12.00000	0.00000	0.00000	0.00090	0.00090	0.00090
14.00000	0.00000	0.00000	0.00090	0.00090	0.00090
16.00000	0.00000	0.00000	−0.00640	−0.01040	−0.01440
20.00000	0.00000	0.00000	−0.01400	−0.02150	−0.02890
24.00000	0.00000	0.00000	−0.01800	−0.02430	−0.03050
28.00000	0.00000	0.00000	−0.01800	−0.02430	−0.03050
32.00000	0.00000	0.00000	−0.01800	−0.02430	−0.03050
36.00000	0.00000	0.00000	−0.01800	−0.02430	−0.03050

$\left(\Delta C_{l_\beta}\right)_{LE}, \left(\Delta C_{l_\beta}\right)_{RE}$

	C_T			
α	$(-0.00710$	0.00000	0.03540	0.20140)
−8.00000	0.00002	0.00000	−0.00010	−0.00019
−4.00000	0.00002	0.00000	−0.00010	−0.00019
0.00000	0.00001	0.00000	−0.00005	−0.00014
4.00000	0.00002	0.00000	−0.00010	−0.00017
8.00000	0.00001	0.00000	−0.00005	−0.00009
12.00000	0.00001	0.00000	−0.00005	−0.00012
14.00000	0.00001	0.00000	−0.00006	−0.00015
16.00000	0.00008	0.00000	−0.00040	−0.00076
20.00000	0.00006	0.00000	−0.00029	−0.00085
24.00000	0.00006	0.00000	−0.00030	−0.00080
28.00000	0.00001	0.00000	−0.00010	−0.00024
32.00000	−0.00004	0.00000	−0.00005	−0.00016
36.00000	−0.00009	0.00000	−0.00007	−0.00009

Table C4. Continued

$\left(C_{l_\beta}\right)_{NE}$

α	$\left(C_{l_\beta}\right)_{NE}$
−8.0000	−0.0024
−4.0000	−0.0022
0.0000	−0.0019
4.0000	−0.0017
8.0000	−0.0017
12.0000	−0.0017
14.0000	−0.0018
16.0000	−0.0025
20.0000	−0.0026
24.0000	−0.0019
28.0000	−0.0023
32.0000	−0.0027
36.0000	−0.0031

$\left(\Delta C_{l_{\delta_r}}\right)_{LE}$, $\left(\Delta C_{l_{\delta_r}}\right)_{RE}$

	C_T			
α	(−0.00710	0.00000	0.03540	0.20140)
−8.00000	0.00000	0.00000	0.00000	0.00015
−4.00000	0.00000	0.00000	0.00001	0.00018
0.00000	0.00000	0.00000	0.00001	0.00007
4.00000	0.00000	0.00000	0.00000	0.00003
8.00000	0.00000	0.00000	0.00001	−0.00001
12.00000	0.00000	0.00000	−0.00002	0.00000
14.00000	0.00000	0.00000	0.00000	−0.00006
16.00000	0.00004	0.00000	−0.00015	0.00005
20.00000	0.00002	0.00000	−0.00007	−0.00004
24.00000	0.00000	0.00000	0.00001	−0.00002
28.00000	0.00000	0.00000	−0.00001	−0.00004
32.00000	0.00001	0.00000	−0.00004	−0.00006
36.00000	0.00002	0.00000	−0.00007	−0.00004

$\left(C_{l_{\delta_r}}\right)_{NE}$

α	$\left(C_{l_{\delta_r}}\right)_{NE}$
−8.0000	0.0008
−4.0000	0.0006
0.0000	0.0005
4.0000	0.0004
8.0000	0.0003
12.0000	0.0002
14.0000	0.0001
16.0000	0.0000
20.0000	0.0000
24.0000	−0.0001
28.0000	−0.0001
32.0000	0.0000
36.0000	0.0000

$\left(C_{l_p}\right)_{NE}$

α	$\left(C_{l_p}\right)_{NE}$
−8.0000	−0.4800
−4.0000	−0.4720
0.0000	−0.4660
4.0000	−0.4580
8.0000	−0.4200
12.0000	−0.3250
14.0000	−0.1950
16.0000	0.0000
20.0000	−0.0500
24.0000	−0.1000
28.0000	−0.1250
32.0000	−0.1300
36.0000	−0.1100

Table C4. Concluded

$\left(C_{l_{\delta_{a,L}}}\right)_{NE}$

	Flap deflection, deg	
α	(0.0000	35.0000)
−8.00000	0.00132	0.00147
−4.00000	0.00142	0.00157
0.00000	0.00151	0.00159
4.00000	0.00145	0.00149
8.00000	0.00137	0.00145
12.00000	0.00131	0.00135
14.00000	0.00127	0.00108
16.00000	0.00109	0.00039
20.00000	0.00084	0.00078
24.00000	0.00075	0.00047
28.00000	0.00054	0.00049
32.00000	0.00033	0.00050
36.00000	0.00011	0.00052

$\left(C_{l_{\delta_{aR}}}\right)_{NE}$

	Flap deflection,deg	
α	(0.0000	35.0000)
−8.00000	−0.00132	−0.00147
−4.00000	−0.00142	−0.00157
0.00000	−0.00151	−0.00159
4.00000	−0.00145	−0.00149
8.00000	−0.00137	−0.00145
12.00000	−0.00131	−0.00135
14.00000	−0.00127	−0.00108
16.00000	−0.00109	−0.00039
20.00000	−0.00084	−0.00078
24.00000	−0.00075	−0.00047
28.00000	−0.00054	−0.00049
32.00000	−0.00033	−0.00050
36.00000	−0.00011	−0.00052

$\left(C_{l_r}\right)_{NE}$

α	$\left(C_{l_r}\right)_{NE}$
−8.0000	0.0479
−4.0000	0.0937
0.0000	0.1395
4.0000	0.1853
8.0000	0.2311
12.0000	0.2769
14.0000	0.3000
16.0000	0.0200
20.0000	0.1000
24.0000	0.0600
28.0000	0.0400
32.0000	0.0400
36.0000	0.0400

Table C5. Yawing-Moment Coefficient Data

$\Delta C_{n,LE}$

	C_T				
α	$(-0.00710$	0.00000	0.03540	0.11180	0.20140)
−8.00000	0.00000	0.00000	0.00230	0.00200	0.00170
−4.00000	0.00000	0.00000	0.00130	0.00110	0.00080
0.00000	0.00000	0.00000	0.00000	−0.00010	−0.00020
4.00000	0.00000	0.00000	−0.00080	−0.00080	−0.00080
8.00000	0.00000	0.00000	−0.00130	−0.00130	−0.00130
12.00000	0.00000	0.00000	−0.00130	−0.00130	−0.00130
14.00000	0.00000	0.00000	−0.00150	−0.00150	−0.00150
16.00000	0.00000	0.00000	0.00310	0.00430	0.00550
20.00000	0.00000	0.00000	0.00120	0.00260	0.00400
24.00000	0.00000	0.00000	−0.00370	−0.00060	0.00250
28.00000	0.00000	0.00000	−0.00530	−0.00240	0.00050
32.00000	0.00000	0.00000	−0.00580	−0.00360	−0.00150
36.00000	0.00000	0.00000	−0.00620	−0.00450	−0.00300

$\Delta C_{n,RE}$

	C_T				
α	$(-0.00710$	0.00000	0.03540	0.11180	0.20140)
−8.00000	0.00000	0.00000	−0.00230	−0.00200	−0.00170
−4.00000	0.00000	0.00000	−0.00130	−0.00110	−0.00080
0.00000	0.00000	0.00000	0.00000	0.00010	0.00020
4.00000	0.00000	0.00000	0.00080	0.00080	0.00080
8.00000	0.00000	0.00000	0.00130	0.00130	0.00130
12.00000	0.00000	0.00000	0.00130	0.00130	0.00130
14.00000	0.00000	0.00000	0.00150	0.00150	0.00150
16.00000	0.00000	0.00000	−0.00310	−0.00430	−0.00550
20.00000	0.00000	0.00000	−0.00120	−0.00260	−0.00400
24.00000	0.00000	0.00000	0.00370	0.00060	−0.00250
28.00000	0.00000	0.00000	0.00530	0.00240	−0.00050
32.00000	0.00000	0.00000	0.00580	0.00360	0.00150
36.00000	0.00000	0.00000	0.00620	0.00450	0.00300

$\left(\Delta C_{n_\beta}\right)_{LE}$, $\left(\Delta C_{n_\beta}\right)_{RE}$

	C_T			
α	$(-0.00710$	0.00000	0.03540	0.20140)
−8.00000	0.00015	0.00000	0.00010	0.00021
−4.00000	0.00016	0.00000	0.00005	0.00018
0.00000	0.00005	0.00000	0.00000	0.00020
4.00000	0.00013	0.00000	0.00005	0.00018
8.00000	−0.00005	0.00000	0.00000	0.00005
12.00000	0.00011	0.00000	0.00006	−0.00004
14.00000	0.00010	0.00000	0.00000	0.00005
16.00000	−0.00025	0.00000	0.00025	0.00041
20.00000	−0.00022	0.00000	0.00074	0.00109
24.00000	0.00019	0.00000	0.00095	0.00181
28.00000	0.00014	0.00000	0.00076	0.00169
32.00000	0.00009	0.00000	0.00056	0.00151
36.00000	0.00002	0.00000	0.00035	0.00134

Table C5. Continued

$(C_{n_\beta})_{NE}$

α	$(C_{n_\beta})_{NE}$
−8.0000	0.0024
−4.0000	0.0024
0.0000	0.0022
4.0000	0.0020
8.0000	0.0021
12.0000	0.0023
14.0000	0.0025
16.0000	0.0029
20.0000	0.0016
24.0000	0.0004
28.0000	0.0005
32.0000	0.0006
36.0000	0.0007

$(\Delta C_{n_{\delta_r}})_{LE}$, $(\Delta C_{n_{\delta_r}})_{RE}$

	C_T			
α	(−0.00710	0.00000	0.03540	0.20140)
−8.00000	0.00001	0.00000	−0.00003	−0.00005
−4.00000	0.00000	0.00000	0.00000	−0.00007
0.00000	0.00000	0.00000	0.00000	−0.00006
4.00000	0.00000	0.00000	0.00002	−0.00007
8.00000	0.00001	0.00000	−0.00004	−0.00009
12.00000	0.00001	0.00000	−0.00003	−0.00006
14.00000	0.00000	0.00000	−0.00001	−0.00003
16.00000	0.00001	0.00000	−0.00002	0.00002
20.00000	0.00003	0.00000	−0.00013	−0.00011
24.00000	0.00002	0.00000	−0.00009	−0.00018
28.00000	0.00002	0.00000	−0.00008	−0.00019
32.00000	0.00002	0.00000	−0.00008	−0.00020
36.00000	0.00002	0.00000	−0.00010	−0.00022

$(C_{n_{\delta_r}})_{NE}$

α	$(C_{n_{\delta_r}})_{NE}$
−8.0000	−0.0013
−4.0000	−0.0013
0.0000	−0.0013
4.0000	−0.0013
8.0000	−0.0012
12.0000	−0.0011
14.0000	−0.0011
16.0000	−0.0010
20.0000	−0.0006
24.0000	−0.0004
28.0000	−0.0002
32.0000	0.0000
36.0000	0.0000

$(C_{n_p})_{NE}$

α	$(C_{n_p})_{NE}$
−8.0000	0.0700
−4.0000	0.0400
0.0000	−0.0180
4.0000	−0.0700
8.0000	−0.1150
12.0000	−0.1250
14.0000	−0.0700
16.0000	0.0500
20.0000	−0.0650
24.0000	0.0100
28.0000	0.0200
32.0000	0.0200
36.0000	0.0200

Table C5. Concluded

$\left(C_{n_{\delta_{a,L}}}\right)_{NE}$

	Flap deflection, deg	
α	(0.0000	35.0000)
−8.00000	0.00014	0.00017
−4.00000	0.00008	0.00015
0.00000	0.00000	0.00008
4.00000	−0.00004	0.00003
8.00000	−0.00012	−0.00004
12.00000	−0.00014	−0.00006
14.00000	−0.00014	−0.00016
16.00000	−0.00014	−0.00034
20.00000	−0.00030	−0.00020
24.00000	−0.00033	−0.00006
28.00000	−0.00022	−0.00018
32.00000	−0.00012	−0.00029
36.00000	−0.00002	−0.00041

$\left(C_{n_{\delta_{aR}}}\right)_{NE}$

	Flap deflection,deg	
α	(0.0000	35.0000)
−8.00000	−0.00014	−0.00017
−4.00000	−0.00008	−0.00015
0.00000	0.00000	−0.00008
4.00000	0.00004	−0.00003
8.00000	0.00012	0.00004
12.00000	0.00014	0.00006
14.00000	0.00014	0.00016
16.00000	0.00014	0.00034
20.00000	0.00030	0.00020
24.00000	0.00033	0.00006
28.00000	0.00022	0.00018
32.00000	0.00012	0.00029
36.00000	0.00002	0.00041

$\left(C_{n_r}\right)_{NE}$

α	$\left(C_{n_r}\right)_{NE}$
−8.0000	−0.1950
−4.0000	−0.1950
0.0000	−0.1950
4.0000	−0.1950
8.0000	−0.1950
12.0000	−0.1950
14.0000	−0.1950
16.0000	−0.0800
20.0000	−0.1750
24.0000	−0.1500
28.0000	−0.1200
32.0000	−0.1000
36.0000	−0.1000

Table C6. Side-Force-Coefficient Data

$\Delta C_{Y,LE}$

	C_T				
α	(−0.00710	0.00000	0.03540	0.11180	0.20140)
−8.00000	0.00000	0.00000	−0.00800	−0.00700	−0.00600
−4.00000	0.00000	0.00000	−0.00550	−0.00500	−0.00450
0.00000	0.00000	0.00000	−0.00350	−0.00350	−0.00350
4.00000	0.00000	0.00000	−0.00150	−0.00150	−0.00150
8.00000	0.00000	0.00000	−0.00150	−0.00150	−0.00150
12.00000	0.00000	0.00000	−0.00200	−0.00200	−0.00200
14.00000	0.00000	0.00000	−0.00150	−0.00150	−0.00150
16.00000	0.00000	0.00000	−0.00600	−0.00600	−0.00600
20.00000	0.00000	0.00000	−0.00030	−0.00900	−0.01860
24.00000	0.00000	0.00000	0.00900	−0.00780	−0.02250
28.00000	0.00000	0.00000	0.01750	−0.00270	−0.02300
32.00000	0.00000	0.00000	0.02050	−0.00150	−0.02350
36.00000	0.00000	0.00000	0.02100	−0.00150	−0.02400

$\Delta C_{Y,RE}$

	C_T				
α	(−0.00710	0.00000	0.03540	0.11180	0.20140)
−8.00000	0.00000	0.00000	0.00800	0.00700	0.00600
−4.00000	0.00000	0.00000	0.00550	0.00500	0.00450
0.00000	0.00000	0.00000	0.00350	0.00350	0.00350
4.00000	0.00000	0.00000	0.00150	0.00150	0.00150
8.00000	0.00000	0.00000	0.00150	0.00150	0.00150
12.00000	0.00000	0.00000	0.00200	0.00200	0.00200
14.00000	0.00000	0.00000	0.00150	0.00150	0.00150
16.00000	0.00000	0.00000	0.00600	0.00600	0.00600
20.00000	0.00000	0.00000	0.00030	0.00900	0.01860
24.00000	0.00000	0.00000	−0.00900	0.00780	0.02250
28.00000	0.00000	0.00000	−0.01750	0.00270	0.02300
32.00000	0.00000	0.00000	−0.02050	0.00150	0.02350
36.00000	0.00000	0.00000	−0.02100	0.00150	0.02400

$\left(\Delta C_{Y_\beta}\right)_{LE}$, $\left(\Delta C_{Y_\beta}\right)_{RE}$

	C_T			
α	(−0.00710	0.00000	0.03540	0.20140)
−8.00000	0.00056	0.00000	−0.00060	−0.00127
−4.00000	0.00020	0.00000	−0.00055	−0.00088
0.00000	0.00025	0.00000	−0.00039	−0.00075
4.00000	0.00021	0.00000	−0.00055	−0.00079
8.00000	−0.00025	0.00000	−0.00050	−0.00100
12.00000	0.00002	0.00000	−0.00050	−0.00066
14.00000	0.00055	0.00000	−0.00045	−0.00081
16.00000	0.00200	0.00000	−0.00102	−0.00118
20.00000	0.00069	0.00000	−0.00256	−0.00271
24.00000	0.00054	0.00000	−0.00286	−0.00347
28.00000	0.00036	0.00000	−0.00143	−0.00396
32.00000	0.00019	0.00000	−0.00075	−0.00356
36.00000	0.00015	0.00000	−0.00040	−0.00258

Table C6. Continued

$\left(C_{Y_\beta}\right)_{NE}$

α	$\left(C_{Y_\beta}\right)_{NE}$
−8.0000	−0.0157
−4.0000	−0.0154
0.0000	−0.0141
4.0000	−0.0135
8.0000	−0.0130
12.0000	−0.0133
14.0000	−0.0136
16.0000	−0.0137
20.0000	−0.0076
24.0000	−0.0048
28.0000	−0.0029
32.0000	−0.0020
36.0000	−0.0017

$\left(\Delta C_{Y_{\delta_r}}\right)_{LE}$, $\left(\Delta C_{Y_{\delta_r}}\right)_{RE}$

	C_T			
α	(−0.00710	0.00000	0.03540	0.20140)
−8.00000	−0.00002	0.00000	0.00009	0.00019
−4.00000	−0.00001	0.00000	0.00002	0.00012
0.00000	−0.00001	0.00000	0.00004	0.00014
4.00000	−0.00001	0.00000	0.00004	0.00014
8.00000	−0.00001	0.00000	0.00005	0.00015
12.00000	0.00000	0.00000	0.00000	0.00010
14.00000	−0.00001	0.00000	0.00003	0.00013
16.00000	−0.00007	0.00000	0.00026	0.00037
20.00000	−0.00008	0.00000	0.00033	0.00053
24.00000	−0.00010	0.00000	0.00024	0.00045
28.00000	−0.00007	0.00000	0.00026	0.00040
32.00000	−0.00004	0.00000	0.00041	0.00076
36.00000	−0.00014	0.00000	0.00057	0.00103

$\left(C_{Y_{\delta_r}}\right)_{NE}$

α	$\left(C_{Y_{\delta_r}}\right)_{NE}$
−8.0000	0.0037
−4.0000	0.0035
0.0000	0.0033
4.0000	0.0031
8.0000	0.0029
12.0000	0.0029
14.0000	0.0028
16.0000	0.0026
20.0000	0.0016
24.0000	0.0010
28.0000	0.0004
32.0000	−0.0002
36.0000	−0.0009

$\left(C_{Y_P}\right)_{NE}$

α	$\left(C_{Y_P}\right)_{NE}$
−8.0000	−0.0220
−4.0000	0.0350
0.0000	0.0600
4.0000	0.1000
8.0000	0.1300
12.0000	0.1750
14.0000	0.1820
16.0000	0.0200
20.0000	0.0700
24.0000	0.1000
28.0000	0.1000
32.0000	0.1000
36.0000	0.1000

Table C6. Concluded

$\left(C_{Y_{\delta_{a,L}}}\right)_{NE}$

	Flap deflection, deg	
α	(0.0000	35.0000)
−8.00000	0.00045	0.00046
−4.00000	0.00030	0.00041
0.00000	0.00030	0.00035
4.00000	0.00045	0.00039
8.00000	0.00055	0.00035
12.00000	0.00041	0.00033
14.00000	0.00016	0.00024
16.00000	−0.00001	0.00020
20.00000	−0.00009	0.00001
24.00000	0.00025	0.00035
28.00000	−0.00006	0.00005
32.00000	−0.00035	−0.00025
36.00000	−0.00065	−0.00055

$\left(C_{Y_{\delta_{a,R}}}\right)_{NE}$

	Flap deflection,deg	
α	(0.0000	35.0000)
−8.00000	−0.00045	−0.00046
−4.00000	−0.00030	−0.00041
0.00000	−0.00030	−0.00035
4.00000	−0.00045	−0.00039
8.00000	−0.00055	−0.00035
12.00000	−0.00041	−0.00033
14.00000	−0.00016	−0.00024
16.00000	0.00001	−0.00020
20.00000	0.00009	−0.00001
24.00000	−0.00025	−0.00035
28.00000	0.00006	−0.00005
32.00000	0.00035	0.00025
36.00000	0.00065	0.00055

$\left(C_{Y_r}\right)_{NE}$

α	$\left(C_{Y_r}\right)_{NE}$
−8.0000	0.8000
−4.0000	0.7600
0.0000	0.7200
4.0000	0.6800
8.0000	0.6400
12.0000	0.6000
14.0000	0.5800
16.0000	0.5200
20.0000	0.4000
24.0000	0.2800
28.0000	0.1600
32.0000	0.0400
36.0000	0.0000

Appendix D

Control System Models

Basic block diagrams for the longitudinal, directional, and lateral control systems are given in figure 7. Pitch trim was accomplished by adjusting horizontal-tail incidence. A tab on the rudder was used to provide directional trim. Roll trim was achieved by introducing a different increment in the deflection of the ailerons. Trim wheels located on the center console in the cockpit were used for rudder tab and aileron trim inputs. A thumb activated switch located on the left horn of the control wheel was used to adjust pitch trim. Control loaders provided forces on the column, wheel, and pedals. The forces used with the control loaders were calculated as follows:

Column force:

$$F_c = G_e C_{h_e} q_\infty S_e \bar{c}_e + \text{ breakout}$$

Parameter	Function of	Value
C_{h_e}	δ_e, i_t	See table D1
G_e	δ_e	See table D2
S_e		16.839
$\bar{c}_e$		1.251

Pedal force:

$$F_p = G_r C_{h_r} q_\infty S_r \bar{c}_r + \text{ breakout}$$

Parameter	Function of	Value
C_{h_r}	δ_r, β	See table D3
G_r	δ_r	See table D4
S_r		14.67
$\bar{c}_r$		2.31

Wheel force:

$$\delta_a = \frac{\delta_{a,R} - \delta_{a,L}}{2}$$

$$F_w = 2 G_a C_{h_a} \delta_a q_\infty S_a \bar{c}_a + \text{ breakout}$$

Parameter	Function of	Value
C_{h_a}	δ_a	0.0062
G_a		See table D5
S_a		10.15
$\bar{c}_a$		1.21

Breakout force:

Control	Value, direction
Column	+3.5 (aft) −5.0 (forward)
Pedals	+17 (right) −22 (left)
Wheel	+3 (right) −3 (left)

Maximum control surface deflections:

Control	Value
δ_e	−16° to +14°
i_t	−16° to +8°
$\delta_{a,R}$	−15° (up) to +17° (down)
$\delta_{a,L}$	−15° (up) to +17° (down)
δ_r	±25°

For convenience, three additional block diagrams are shown with the longitudinal control system. Diagrams are given for the flaps, speed brakes, and landing gear. The speed break and landing gear cockpit control had two positions, either retracted or extended. The flap cockpit position lever had four detents to position the flaps at deflection angles of 0°, 7°, 20°, and 35°. The first-order lag indicated in each block diagram was used to provide a realistic output response. The time constants used are as follows:

Time constant	Value	Time for full deployment, sec
τ_f	4.0	16
τ_{SB}	1.0	4
τ_{LG}	3.0	12

Table D1. Values of Elevator Hinge Moment Coefficient C_{h_e}

δ_e, deg	C_{h_e} at—						
	$i_t = -16°$	$i_t = -12°$	$i_t = -8°$	$i_t = -4°$	$i_t = 0°$	$i_t = 4°$	$i_t = 8°$
−20	0.20110	0.16817	0.14351	0.12349	0.11025	0.09421	0.06924
−18	0.18535	0.14723	0.11872	0.09690	0.08640	0.07509	0.05380
−16	0.17016	0.12758	0.09478	0.07188	0.06392	0.05664	0.04032
−14	0.15567	0.11018	0.07333	0.05053	0.04454	0.03917	0.02925
−12	0.14200	0.09600	0.05600	0.03500	0.03000	0.02300	0.02100
−10	0.13090	0.08406	0.04345	0.02631	0.02410	0.01837	0.01722
−8	0.12048	0.07236	0.03378	0.02104	0.02197	0.02065	0.01419
−6	0.10764	0.06021	0.02489	0.01589	0.01642	0.01594	0.00765
0	0.06884	0.02700	0.00112	−0.00229	−0.03240	−0.00678	−0.01488
6	0.03142	−0.00300	−0.01364	−0.01709	−0.01775	−0.02455	−0.03639
8	0.02126	−0.01258	−0.01873	−0.02382	−0.02575	−0.03801	−0.04947
10	0.01398	−0.01952	−0.02485	−0.03193	−0.03740	−0.05641	−0.06797
12	0.00845	−0.02414	−0.03139	−0.04064	−0.05138	−0.07668	−0.08992
14	0.00323	−0.02720	−0.03785	−0.04986	−0.06705	−0.09725	−0.11339
16	−0.00308	−0.02947	−0.04370	−0.05952	−0.08374	−0.11655	−0.13650
18	−0.01111	−0.03095	−0.04822	−0.06950	−0.10103	−0.13410	−0.15822
20	−0.02000	−0.03000	−0.05100	−0.80000	−0.12000	−0.15100	−0.18000

Table D2. Elevator Gearing Data

δ_e, deg	G_e, 1/ft
−20	1.07
−18	0.93
−16	0.79
−14	0.62
−12	0.54
−10	0.49
−8	0.47
−6	0.47
0	0.47
6	0.47
8	0.47
10	0.48
12	0.52
14	0.60
16	0.79
18	0.97
20	1.15

Table D3. Value of Rudder Hinge Moment Coefficient C_{h_r}

δ_r, deg	C_{h_r} at—				
	$\beta = -20°$	$\beta = -10°$	$\beta = 0°$	$\beta = 10°$	$\beta = 20°$
−30	0.32	0.25	0.22	0.17	0.06
−20	0.24	0.16	0.13	0.08	0.01
−10	0.16	0.08	0.04	0.03	−0.04
−5	0.13	0.05	0.02	0.01	−0.07
0	−0.11	−0.03	0	0.03	0.11
5	−0.13	−0.05	−0.02	−0.01	0.07
10	−0.16	−0.08	−0.04	−0.03	0.04
20	−0.24	−0.16	−0.13	−0.08	−0.01
30	−0.32	−0.25	−0.22	−0.17	−0.06

Table D4. Rudder Gearing Data

δ_r, deg	G_r, 1/ft
-30	0.35
-20	0.85
-10	1.25
-5	1.29
0	1.32
5	1.29
10	1.26
20	0.84
30	0.35

Table D5. Aileron Gearing Data

δ_a, deg	G_a, 1/ft
-18	-0.13
-16	-0.39
-14	-0.40
-12	-0.41
-10	-0.41
-8	-0.41
-4	-0.41
0	-0.41
4	-0.41
6	-0.41
8	-0.41
10	-0.39
12	-0.36
14	-0.33
16	-0.28

References

1. Albers, James A.; and Zuk, John: *Aircraft Technology Opportunities for the 21st Century.* NASA TM-101060, 1988.

2. Hager, Roy D.; and Vrabel, Deborah: *Advanced Turboprop Project.* NASA SP-495, 1988.

3. Goldsmith, I. M.: *A Study To Define the Research and Technology Requirements for Advanced Turbo/Propfan Transport Aircraft.* NASA CR-166138, 1981.

4. Dugan, James F.; Miller, Brent A.; Graber, Edwin J.; and Sagerser, David A.: *The NASA High-Speed Turboprop Program.* NASA TM-81561, [1980].

5. Williams, L. J.; Johnson, J. L., Jr.; and Yip, L. P.: Some Aerodynamic Considerations for Advanced Aircraft Configurations. AIAA-84-0562, Jan. 1984.

6. Coe, Paul L., Jr.; Applin, Zachary T.; and Williams, Louis J.: Stability and Control Results for Advanced Turboprop Aft-Mount Installations. *SAE 1984 Transactions*, Volume 93, Soc. of Automative Engineers, Inc., c.1985, pp. 6.256–6.263. (Availableas SAE Paper 841479.)

7. Johnson, J. L., Jr.; and White, E. R.: Exploratory Low-Speed Wind-Tunnel Investigation of Advanced Commuter Configurations Including an Over-the-Wing Propeller Design. AIAA-83-2531, 1983.

8. Johnson, Jospeh L., Jr.; Yip, Long P.; and Jordan, Frank L., Jr.: Preliminary Aerodynamic Design Considerations for Advanced Laminar Flow Aircraft Configurations. Laminar Flow Aircraft Certification, Louis J. Williams, compiler, NASA CP-2413, 1986, pp. 185–225.

9. Turner, Steven George: Configuration Effects on the Stability and Control Characteristics of an Advanced Turboprop Business/Commuter Aircraft. M.S. Thesis, George Washington Univ., 1989.

10. Coe, Paul L., Jr.; Perkins, John N.; and Owens, D. Bruce: Exploratory Wind Tunnel Investigation of the Stability and Control Characteristics of a Three-Surface, Forward-Swept Wing Advanced Turboprop Model. *A Collection of Technical Papers, Part 2—AIAA 8th Aerodynamics Conference*, Aug. 1990, pp. 846–856. (Available as AIAA-90-3074.)

11. Dunham, Dana Morris; Gentry, Garl L.; Manuel, Gregory S.; Applin, Zachary T.; and Quinto, P. Frank: *Low-Speed Aerodynamic Characteristics of a Twin-Engine General Aviation Configuration With Aft-Fuselage-Mounted Pusher Propellers.* NASA TP-2763, 1987.

12. Coe, Paul L., Jr.; Turner, Steven G.; and Owens, D. Bruce: *Low-Speed Wind-Tunnel Investigation of the Flight Dynamic Characteristics of an Advanced Turboprop Business/Commuter Aircraft Configuration.* NASA TP-2982, 1990.

13. Coe, Paul L., Jr.; Perkins, John N.; and Rhodes, Graham S.: 30 by 60 Foot Wind Tunnel Test Highlights for an Over-the-Tail Advanced Turboprop Configuration. AIAA-91-0681, Jan. 1991.

14. Ashworth, Billy R.; and Parrish, Russell V.: A Visual Motion Simulator for General Aviation Compensated Within the Nonlinear Adaptive Washout for Actuator Lag. AIAA Paper No. 76-1720, Apr. 1976.

15. *USAF Stability and Control Datcom.* Contracts AF 33(616)-6460 and F33615-75-C-3067, McDonnell Douglas Corp., Oct. 1960. (Revis. Apr. 1976.)

16. Taylor, James: Manual on Aircraft Loads. AGARDograph 83, Pergamon Press Inc., c.1965.

17. Houbolt, John C.; Steiner, Roy; and Pratt, Kermit G.: *Dynamic Response of Airplanes to Atmospheric Turbulence Including Flight Data on Input and Response.* NASA TR R-199, 1964.

18. Airworthiness Standards: Transport Category Airplanes. FAR, Pt. 25, Federal Aviation Adm., June 1974.

19. Dieudonne, James E.: *Description of a Computer Program and Numerical Technique for Developing Linear Perturbation Models From Nonlinear Systems Simulations* NASA TM-78710, 1978.

20. *Military Specification—Flying Qualities of Piloted Airplanes.* MIL-F-8785C, Nov. 5, 1980. (Supersedes MIL-F-8785B, Aug. 7, 1969.)

21. Shomber, Henry A.; and Gertsen, W. M.: Longitudinal Handling Qualities Criteria: An Evaluation. *J. Aircr.*, vol. 4, no. 4, July/Aug. 1967, pp. 371–376.

22. McCormick, Barnes W.: *Aerodynamics, Aeronautics, and Flight Mechanics.* John Wiley & Sons, Inc., c.1979.

23. Gainer, Thomas G.; and Hoffman, Sherwood: *Summary of Transformation Equations and Equations of Motion Used in Free-Flight and Wind-Tunnel Data Reduction and Analysis.* NASA SP-3070, 1972.

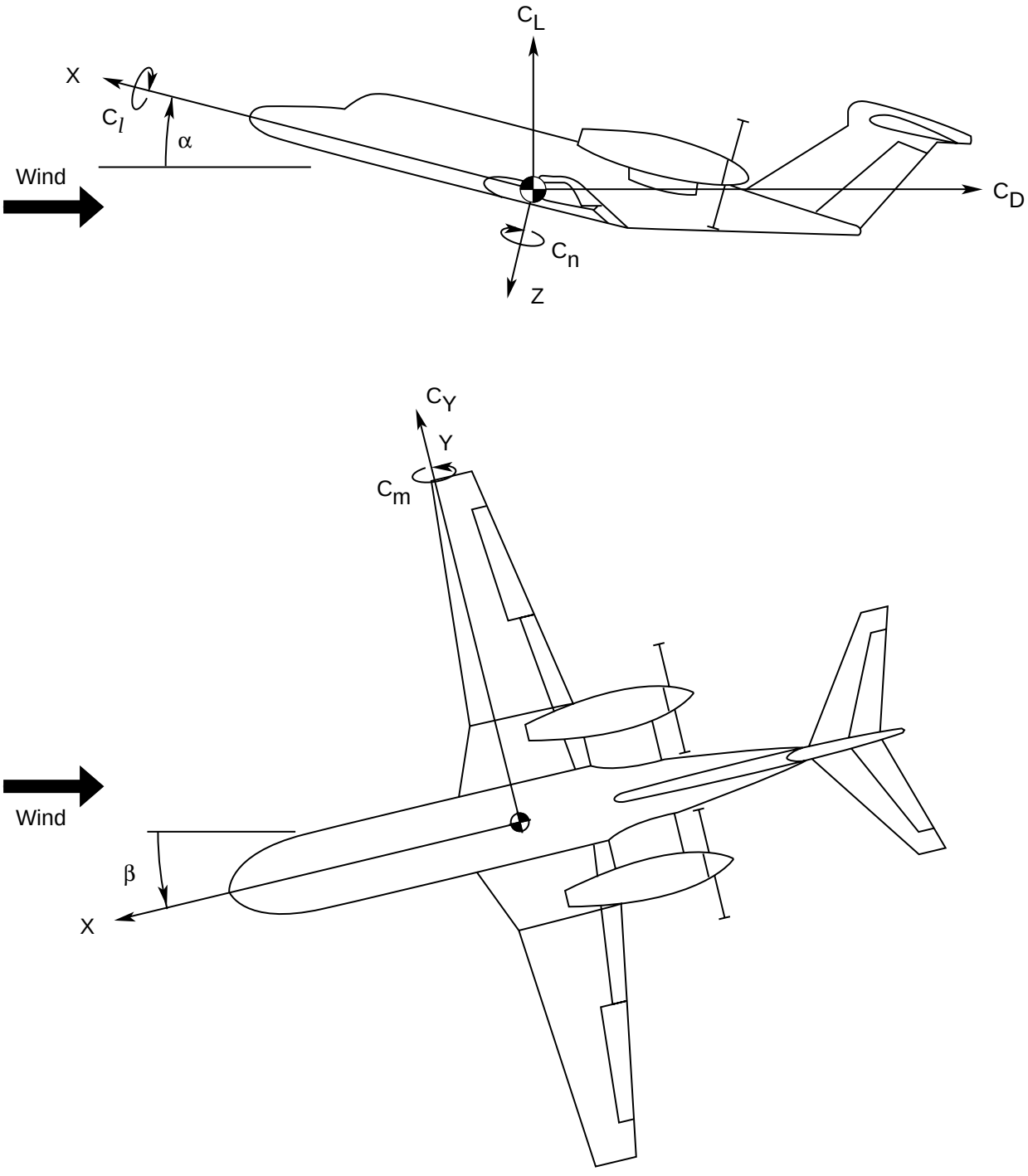

Figure 1. System of body axes.

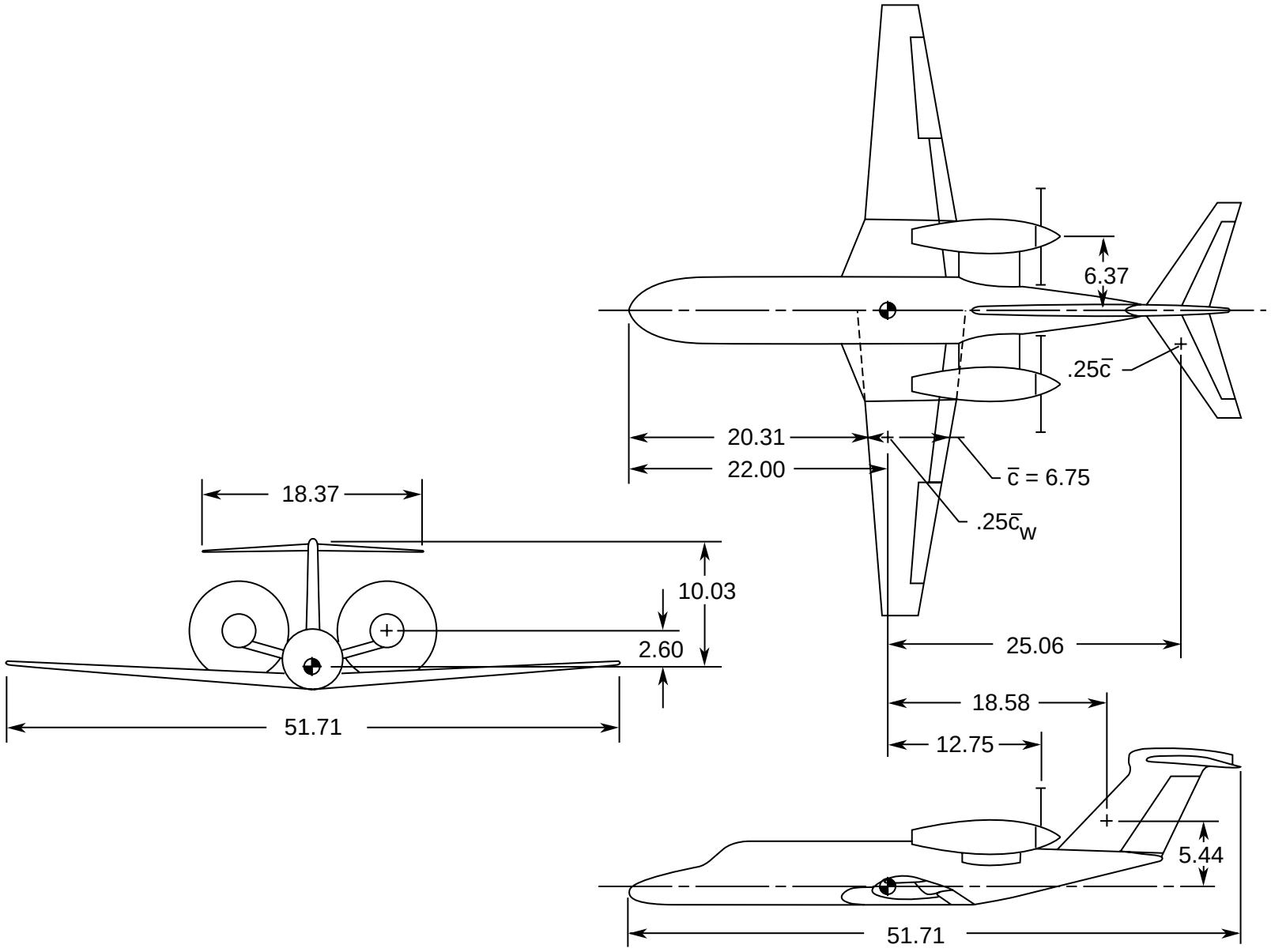

Figure 2. Three views of simulated aircraft. Dimensions are in feet.

Figure 3. Elements of the Langley General Aviation Simulation System.

L-86-360

Figure 4. Three-degree-of-freedom motion base and virtual image system.

L-84-13268

Figure 5. Simulation cockpit with instruments and controls.

$h \times 10^{-3}$: 0, 10, 15, 18, 21, 23, 25, 27, 29, 31, 35, 37, 39, 43
M: 0.1, 0.2, 0.3, 0.4, 0.45, 0.50, 0.55, 0.60, 0.65

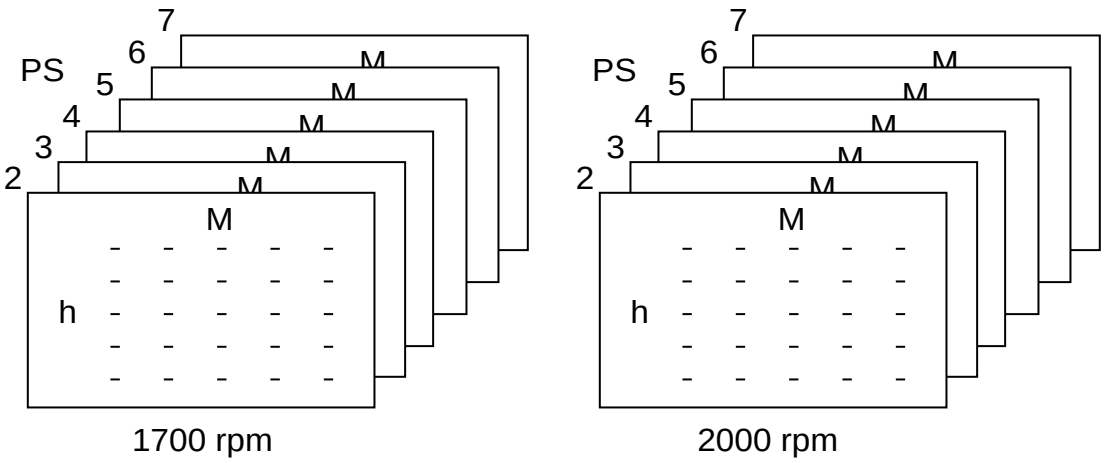

PS	Definition
2	Max continuous
3	Max cruise
4	Max climb/normal cruise
5	80-percent cruise
6	60-percent cruise
7	40-percent cruise
8	
9	
10	Off

Figure 6. Table format used for thrust, torque, and fuel flow data as a function of four variables.

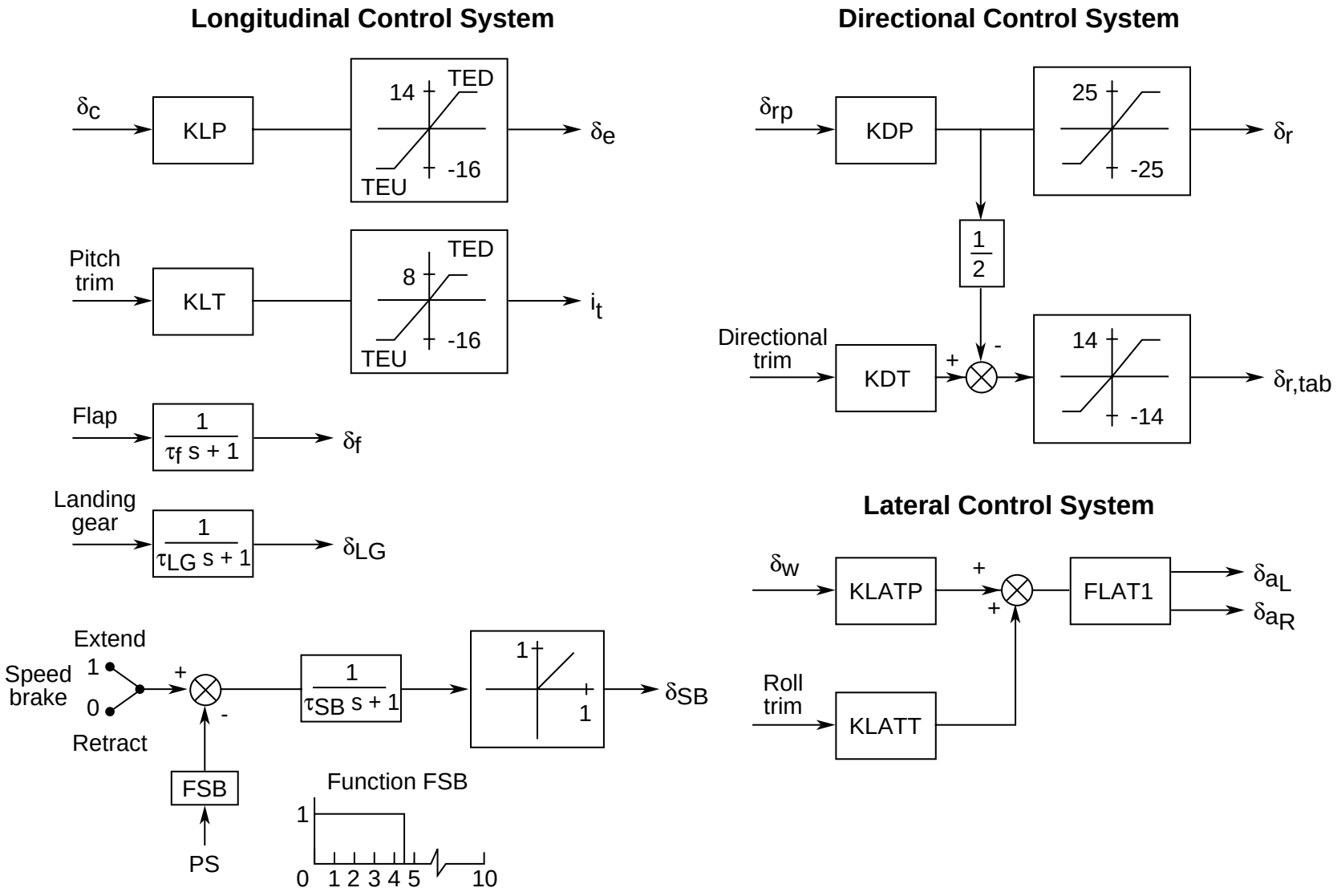

(a) Block diagrams.

Figure 7. Simulation control system.

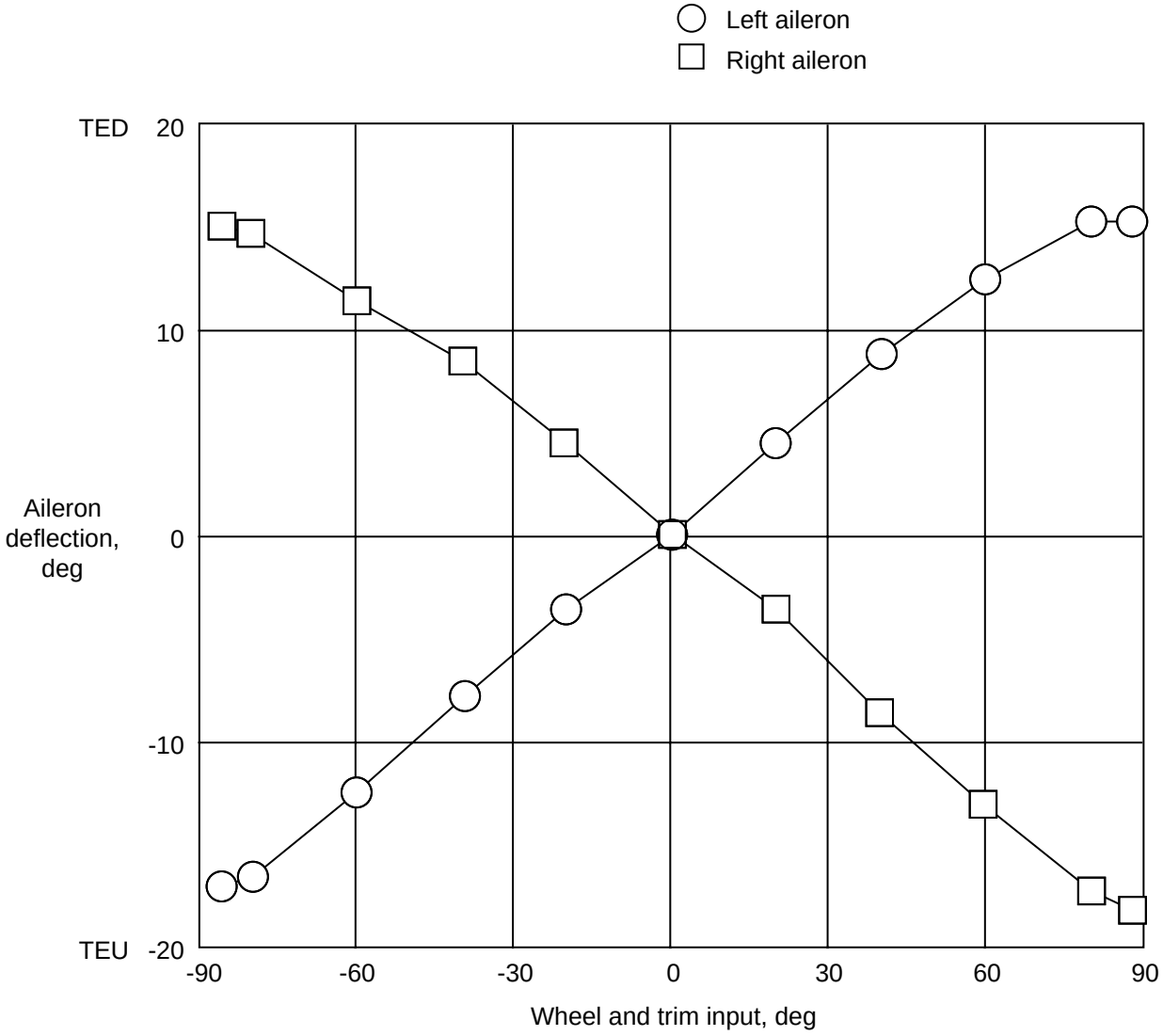

(b) Aileron scaling function FLAT1.

Figure 7. Concluded.

ATP Task Description

1. Initial conditions:
   Task starts a short distance (1/2 NM) before IAF with the airplane trimmed in straight and level flight on a course parallel to the runway at an altitude h of 1600 ft and an IAS of 150 knots

2. At IAF lower flaps to 20° and begin to reduce speed; fly ILS approach

3. At KNUTS lower landing gear; maintain 120 knots

4. At OM lower flaps to 35°; maintain 120 knots

5. Maintain 120 knots down the glideslope

6. At h = 200 ft if the runway is visible, the run is terminated and is considered a normal ILS approach

7. At h = 200 ft if the runway is not visible, execute a missed approach (i.e., full throttle, gear up, flap up, etc.)

8. Right turn to 180°; climb to and maintain h = 2000 ft

Figure 8. ILS task description given to each test subject at preflight briefing.

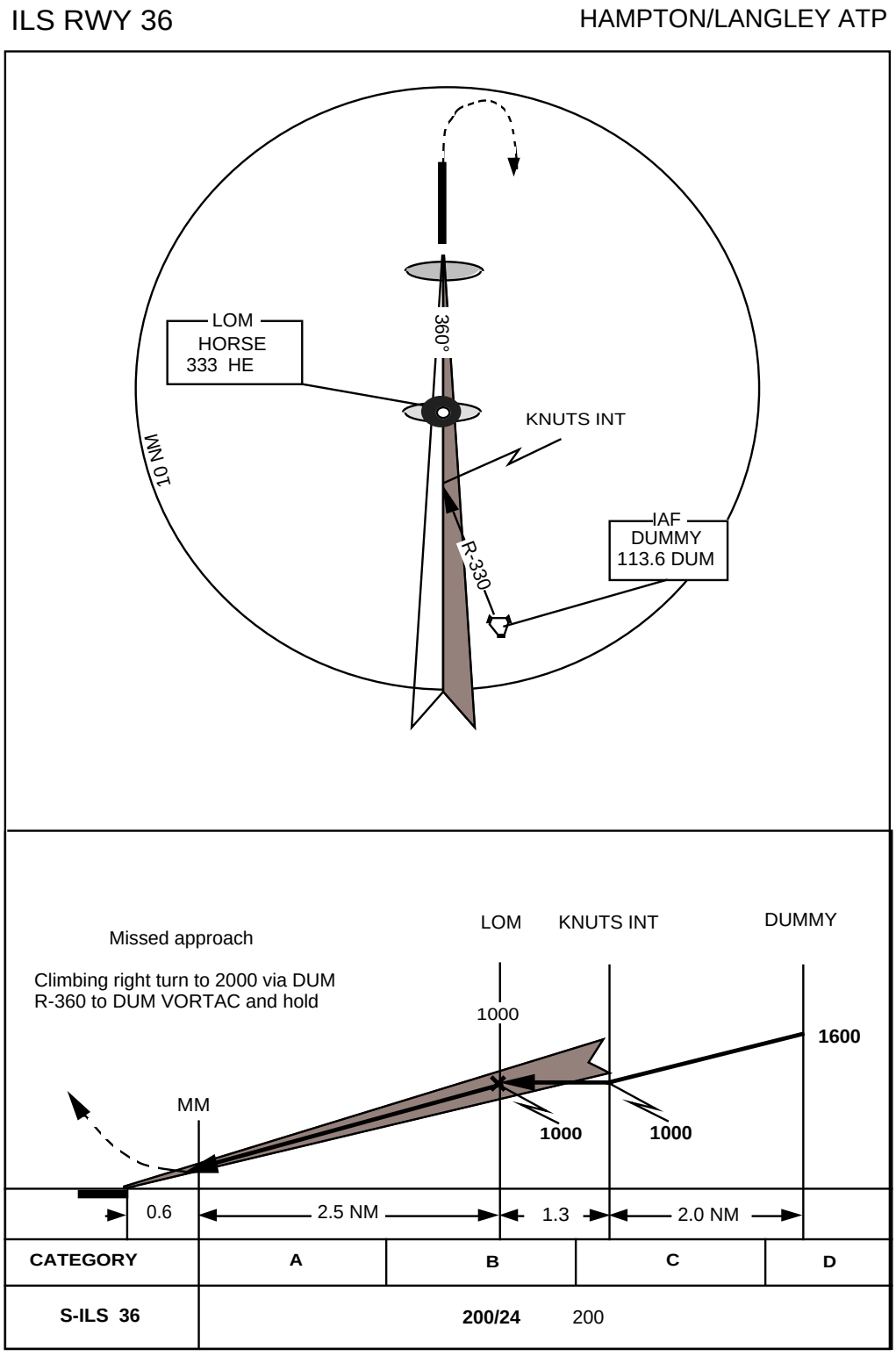

Figure 9. Airport terminal area and ILS approach task.

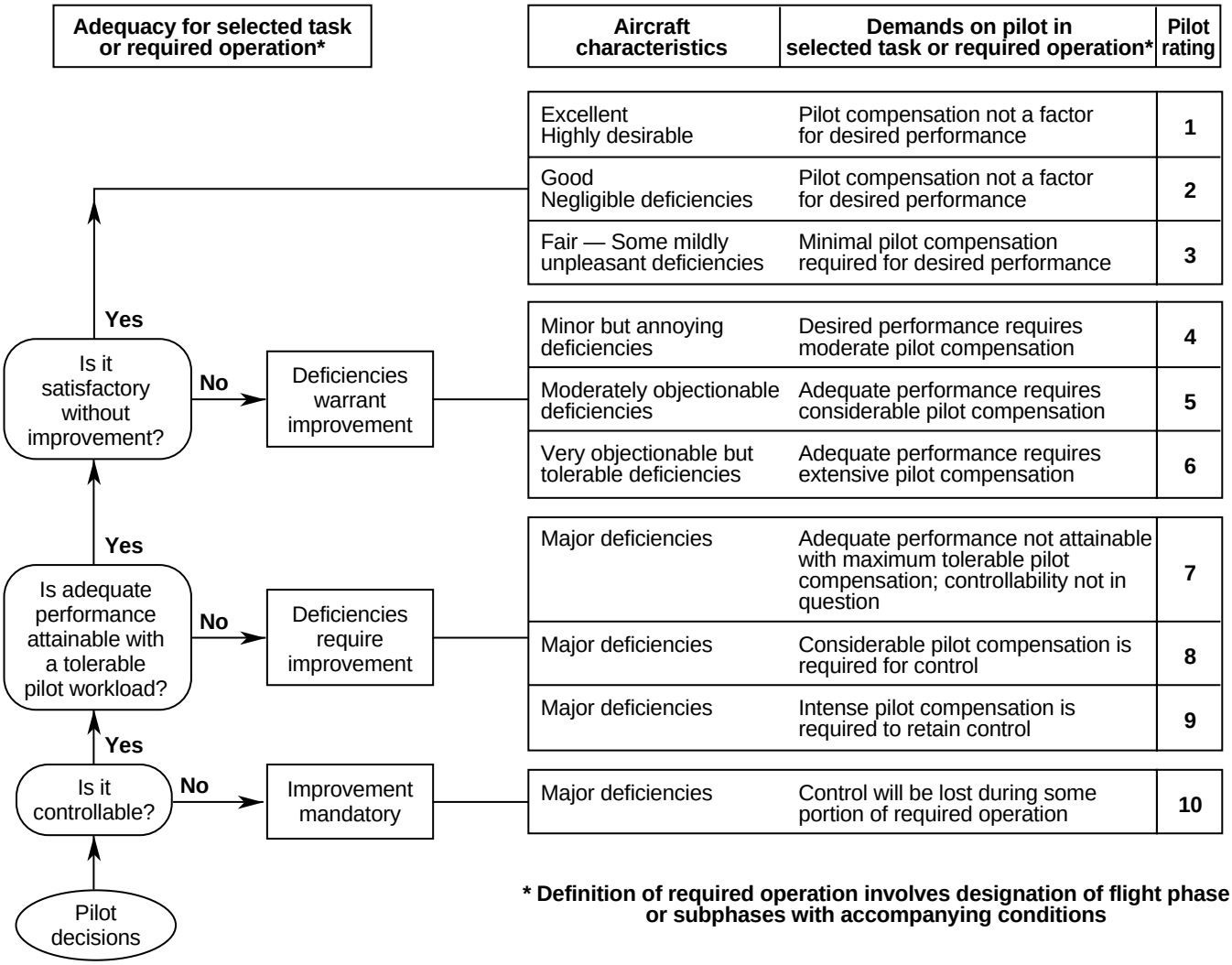

Figure 10. Cooper-Harper scale for rating handling qualities.

ATP Simulation Test Syllabus

Flight condition identification number	Task	Winds	Engine status	Failure location
1	ILS	Off	Both on	None
2	ILS/MA	Off	Both on	None
3	ILS/MA	Off	Left fail	MAP
4	ILS	Off	Right fail	1300 ft
5	ILS/MA	On	Both on	None
6	ILS	On	Left fail	1300 ft
7	ILS/MA	On	Left fail	MAP
8	ILS	On	Right fail	1300 ft
9	ILS/MA	Off	Left fail	1300 ft
10	ILS/MA	Off	Right fail	1300 ft
11	ILS/MA	On	Left fail	1300 ft
12	ILS	Off	Left fail	1300 ft
13	ILS/MA	On	Right fail	MAP
14	ILS/MA	Off	Right fail	MAP
15	ILS	On	Both on	None
16	ILS/MA	On	Right fail	1300 ft

Figure 11. Test conditions for ILS piloted task study.

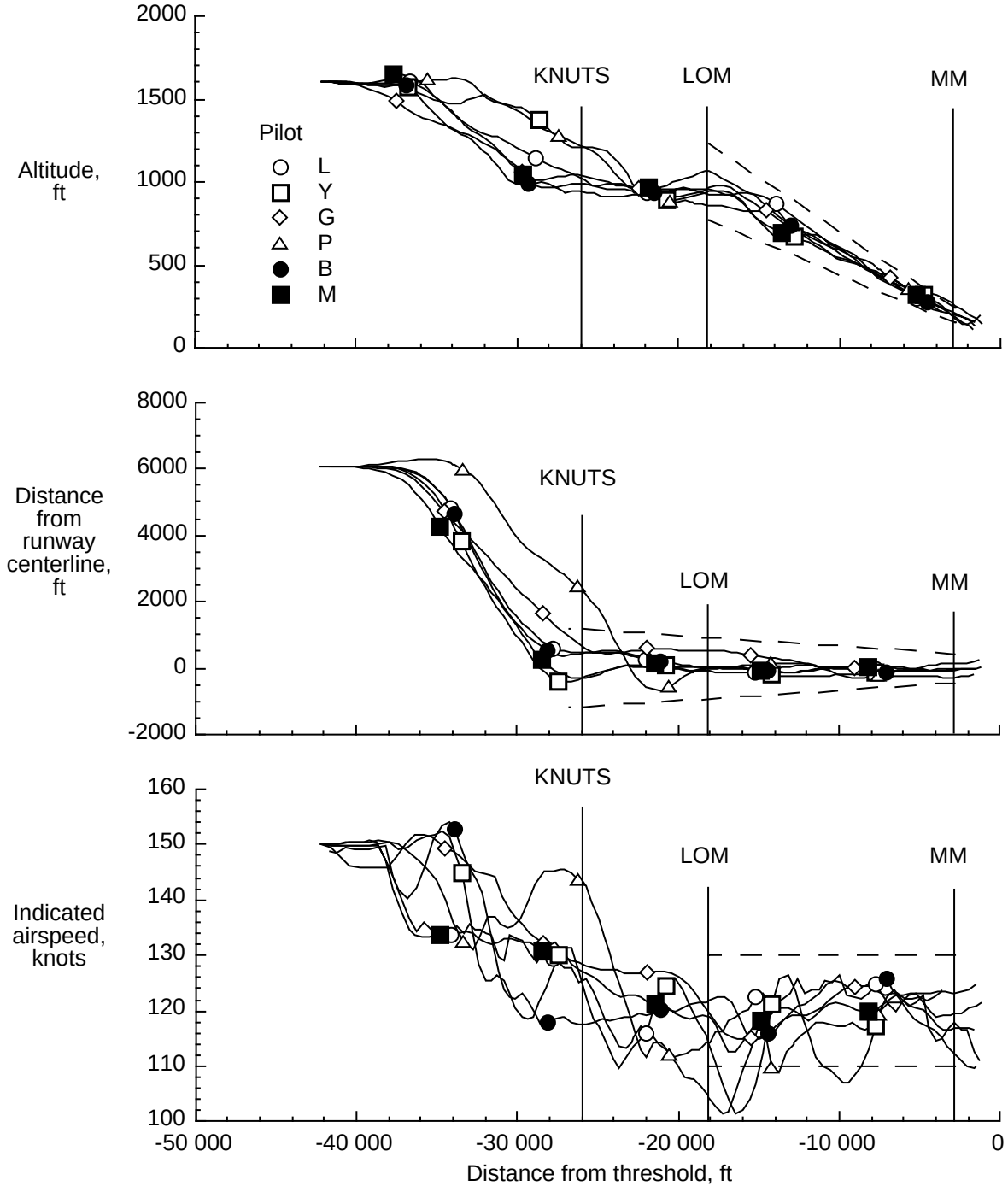

(a) Flight identification number 15. No engine failure, winds on, ceiling at 240 ft AGL.

Figure 12. ILS trajectories for runs with and without a failed engine. Dashed boundary lines represent twice desired target goal.

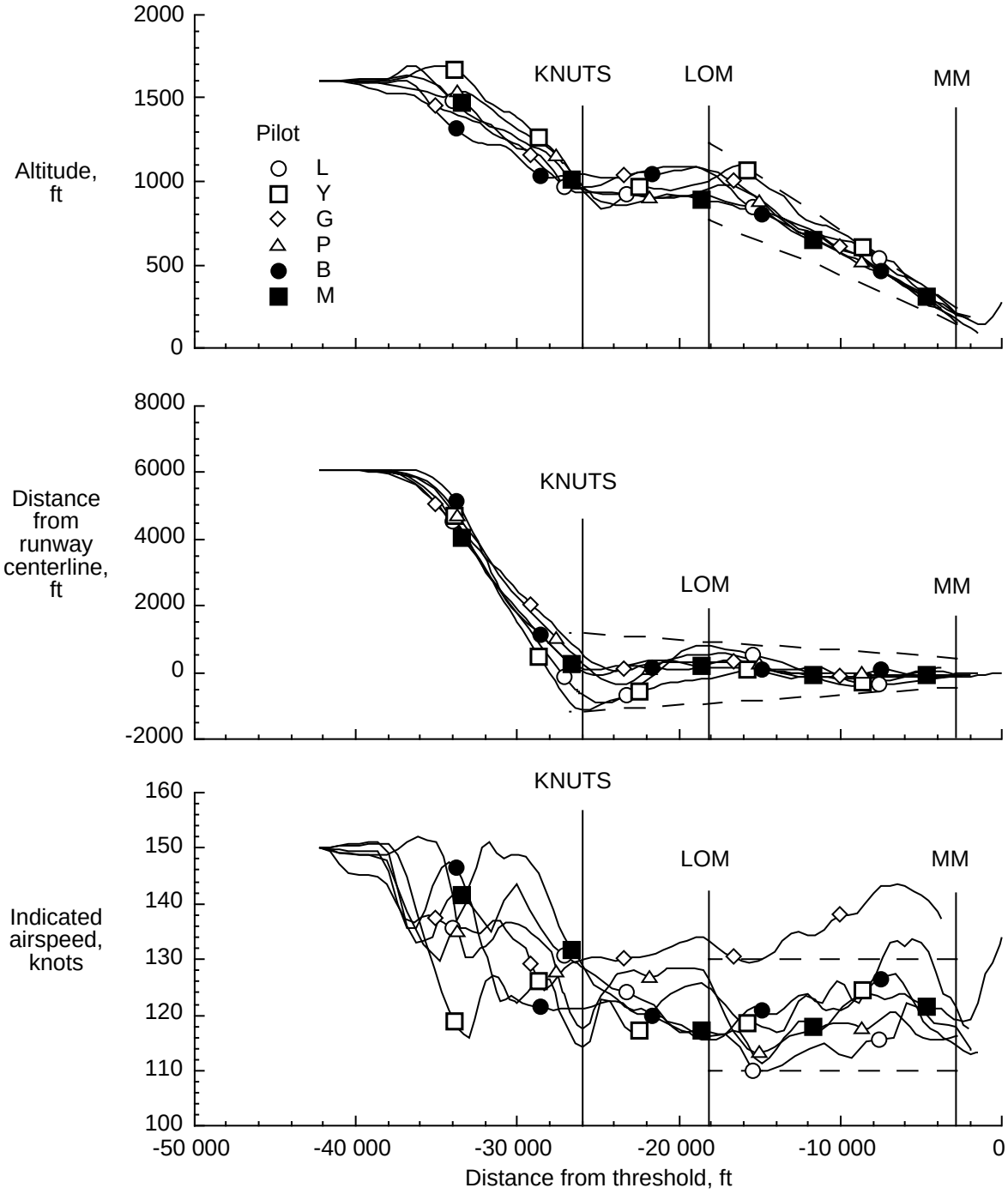

(b) Flight identification number 6. Left engine failure at 1300 ft AGL, winds on, ceiling at 240 ft AGL.

Figure 12. Continued.

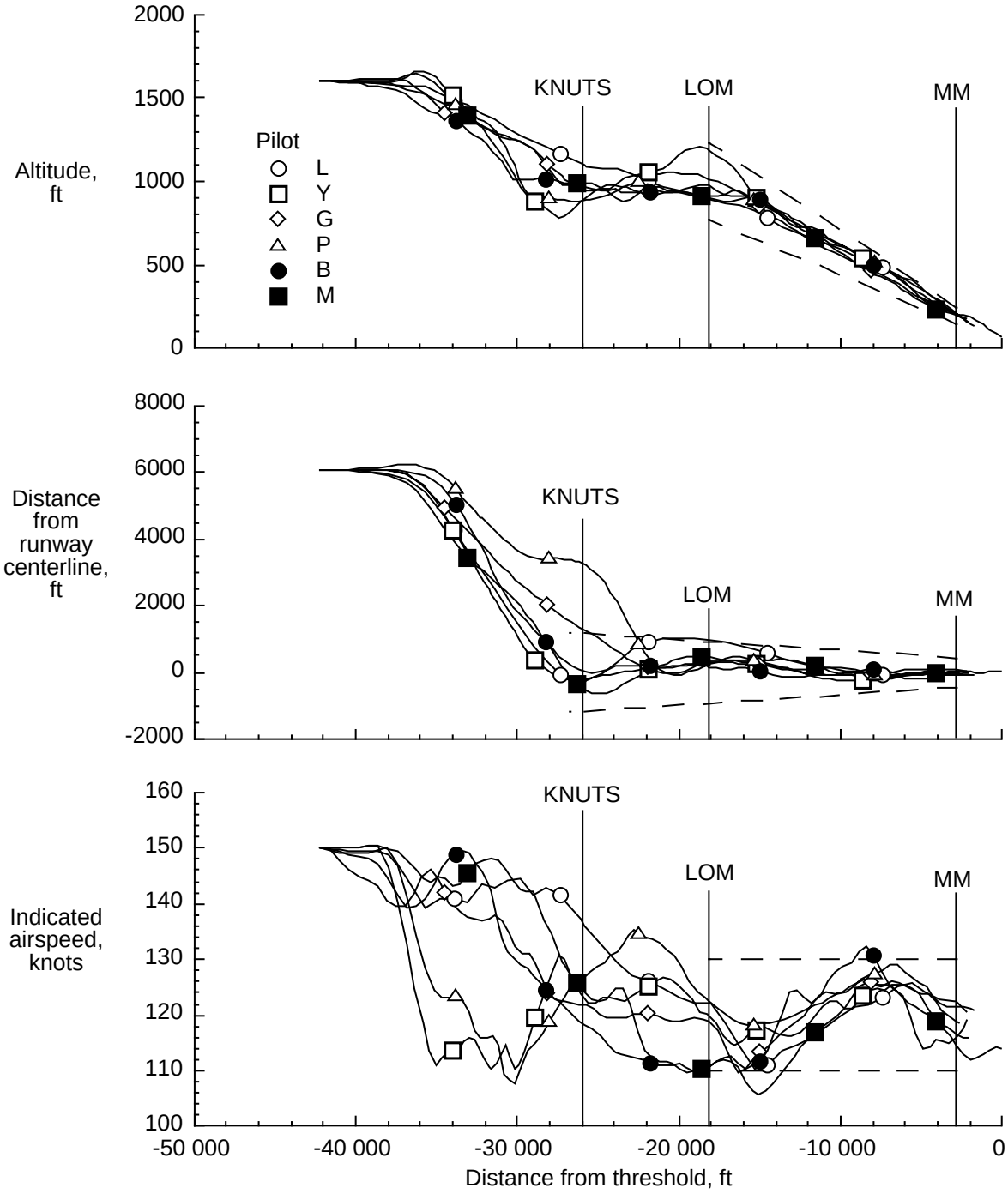

(c) Flight identification number 8. Right engine failure at 1300 ft AGL, winds on, ceiling at 240 ft AGL.

Figure 12. Concluded.

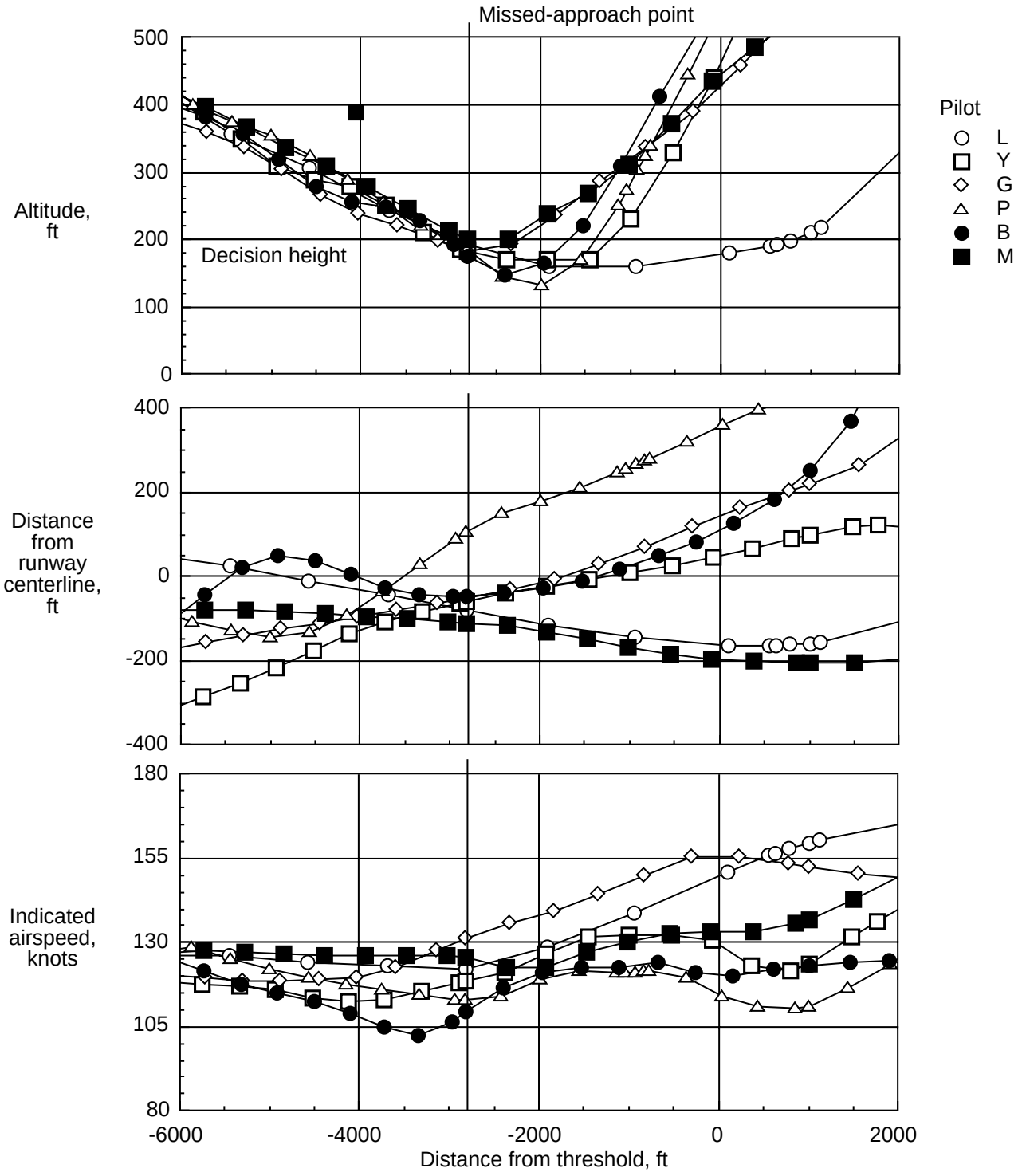

(a) Both engines operating, winds on.

Figure 13. Transition from instrument approach to missed-approach segment for six runs.

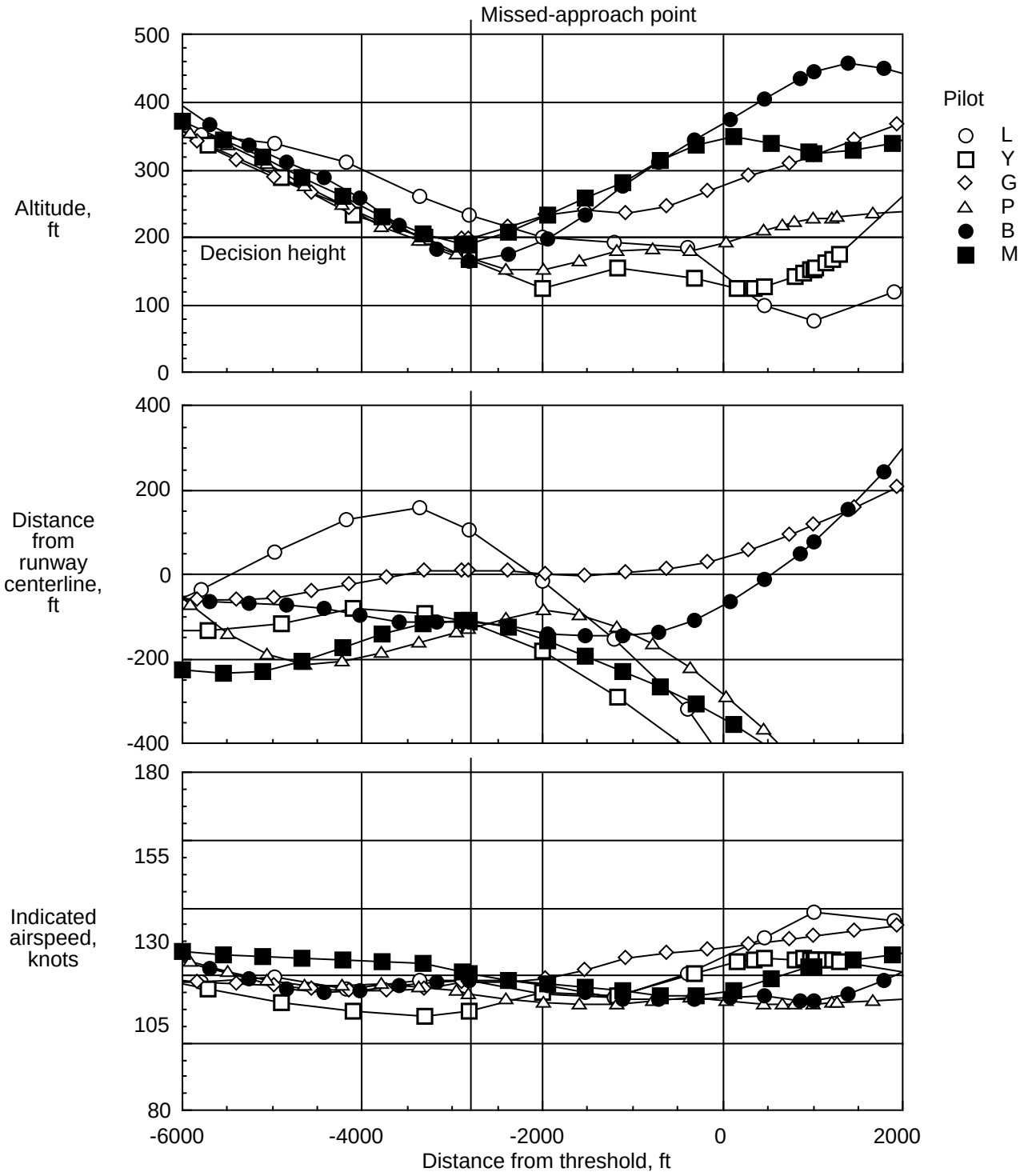

(b) Left engine failure at missed-approach point, winds on.

Figure 13. Continued.

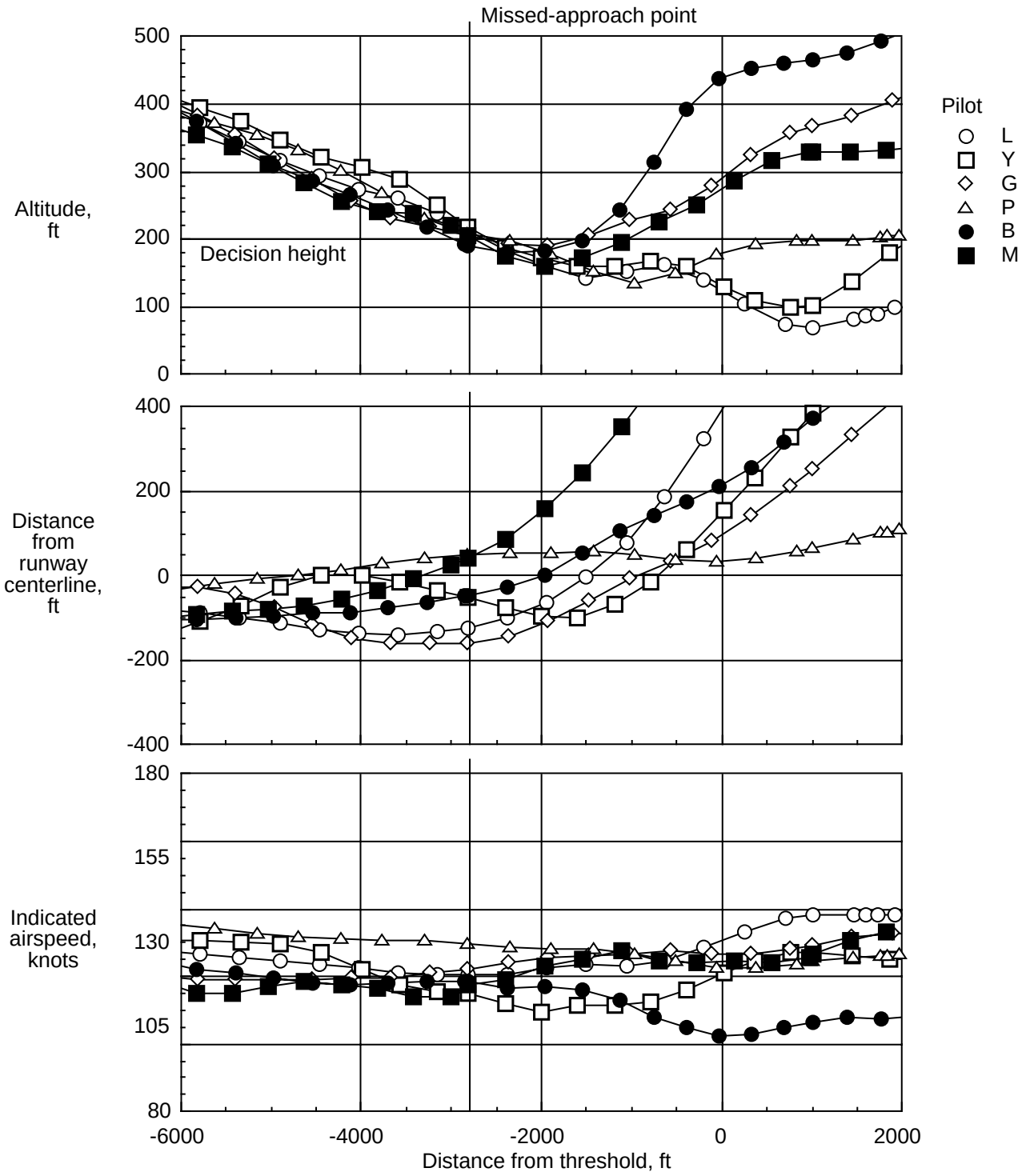

(c) Right engine failure at missed-approach point, winds on.

Figure 13. Concluded.

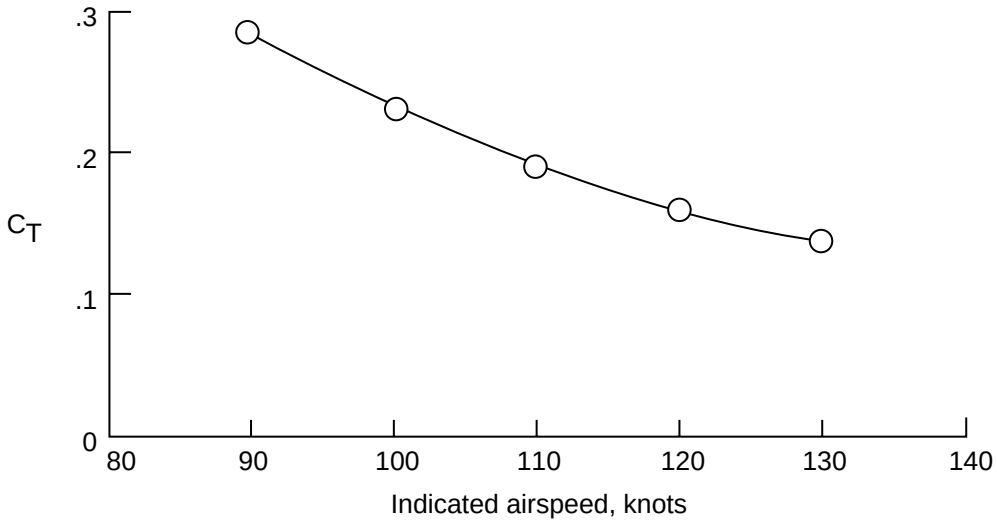

(a) Single engine at full power, PS = 2.

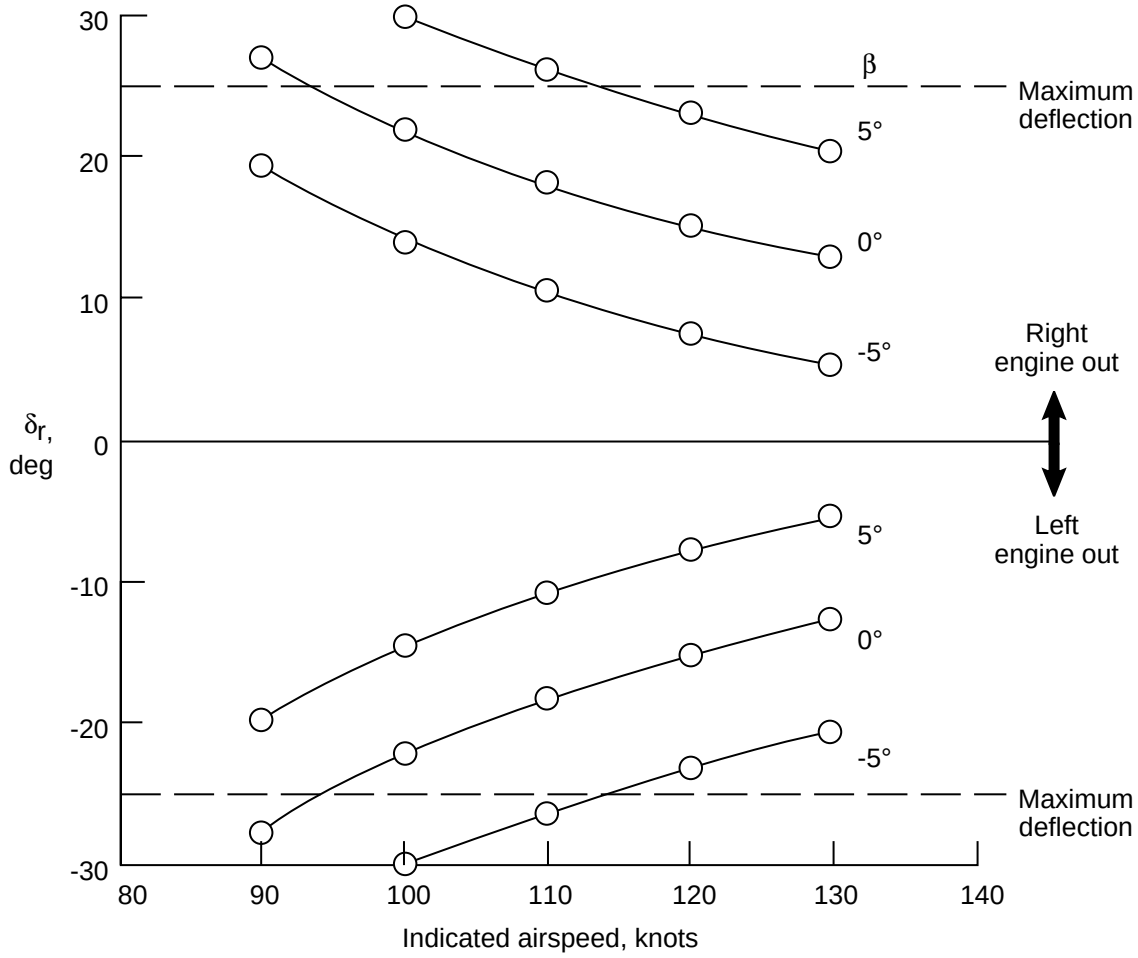

(b) Rudder deflection.

Figure 14. Rudder deflection required for an engine out with full power on operating engine.

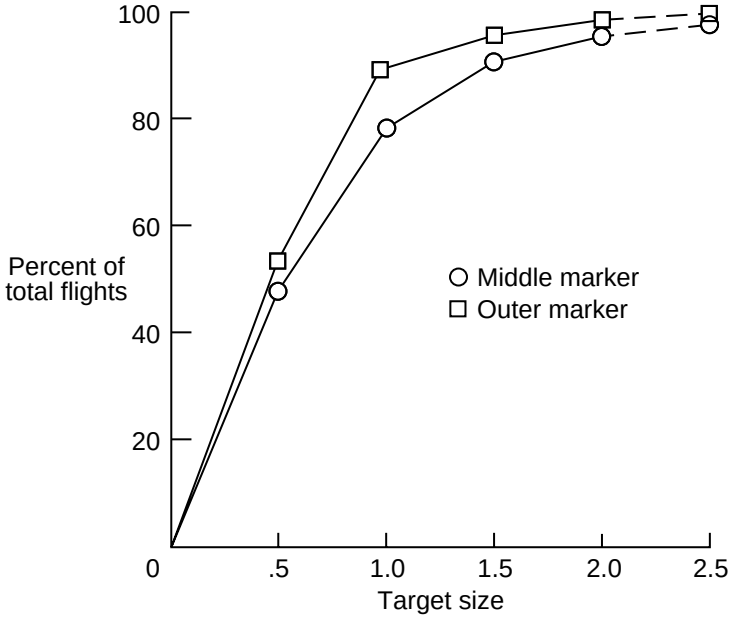

Target size	Δε, deg
0.5	±0.175
1.0	±0.350
1.5	±0.525
2.0	±0.700
2.5	±0.875

(a) Glideslope error.

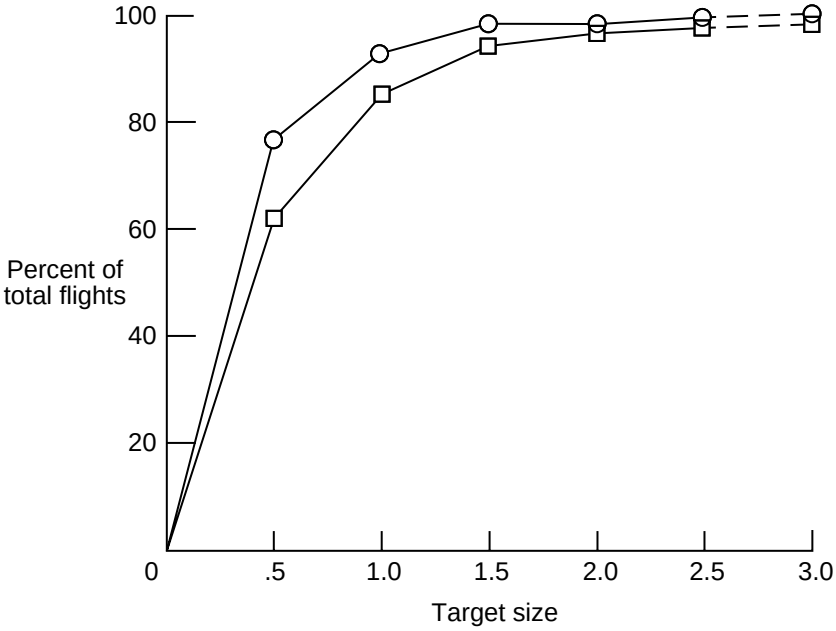

Target size	Δσ, deg
0.5	±0.455
1.0	±0.910
1.5	±1.365
2.0	±1.820
2.5	±2.275
3.0	±2.730

(b) Localized error.

Figure 15. Cumulative frequency distributions for position error and airspeed deviation at middle and outer markers for six pilots. Dashed line indicates when aircraft was beyond the range displayed on cockpit instruments.

Target size	ΔV, knots
0.5	±2.50
1.0	±5.00
1.5	±7.50
2.0	±10.00
2.5	±12.50
3.0	±15.00

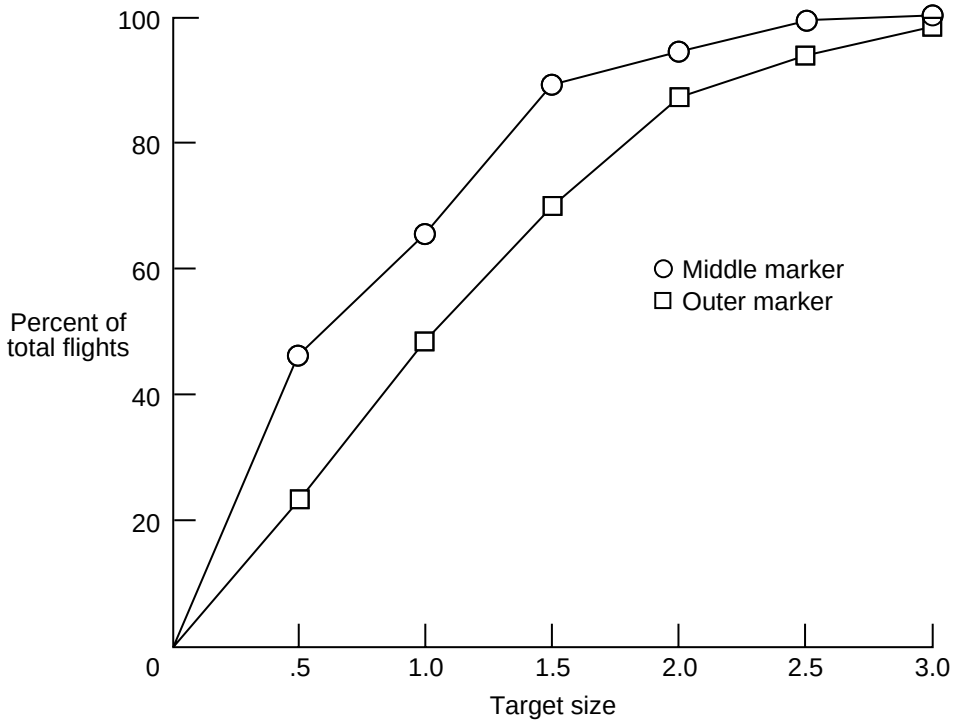

(c) Airspeed deviation.

Figure 15. Concluded.

Target size	$\Delta\varepsilon$, deg	$\Delta\sigma$, deg	ΔV, knots
0.5	±0.175	±0.455	±2.50
1.0	±0.350	±0.910	±5.00
1.5	±0.525	±1.365	±7.50
2.0	±0.700	±1.820	±10.00
2.5	±0.875	±2.275	±12.50
3.0	±1.050	±2.730	±15.00

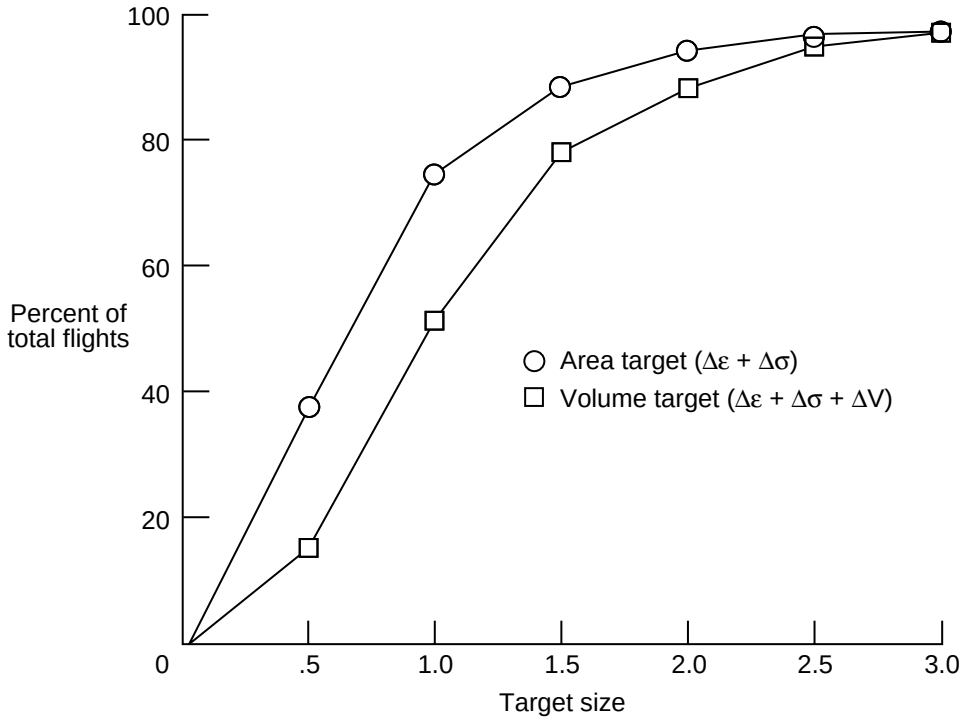

Figure 16. Cumulative frequency distribution for different combinations of position and airspeed errors at middle marker for six pilots.

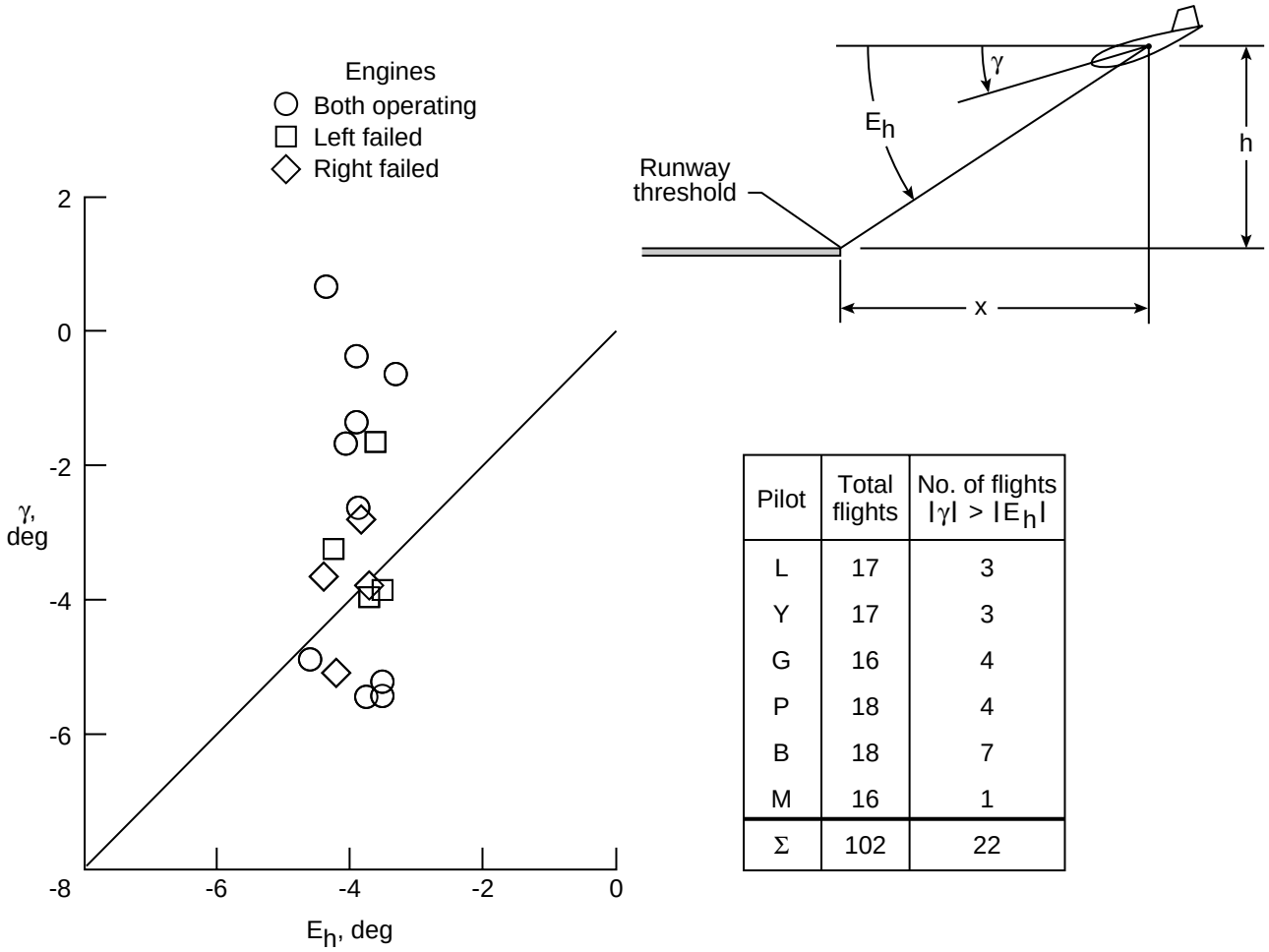

Pilot	Total flights	No. of flights $\lvert\gamma\rvert > \lvert E_h\rvert$
L	17	3
Y	17	3
G	16	4
P	18	4
B	18	7
M	16	1
Σ	102	22

Figure 17. Flight data at middle marker indicating number of flights requiring additional adjustments to rate of descent. Data for pilot B, $E_h = \left(\frac{h}{x}\right)_{MM}$.

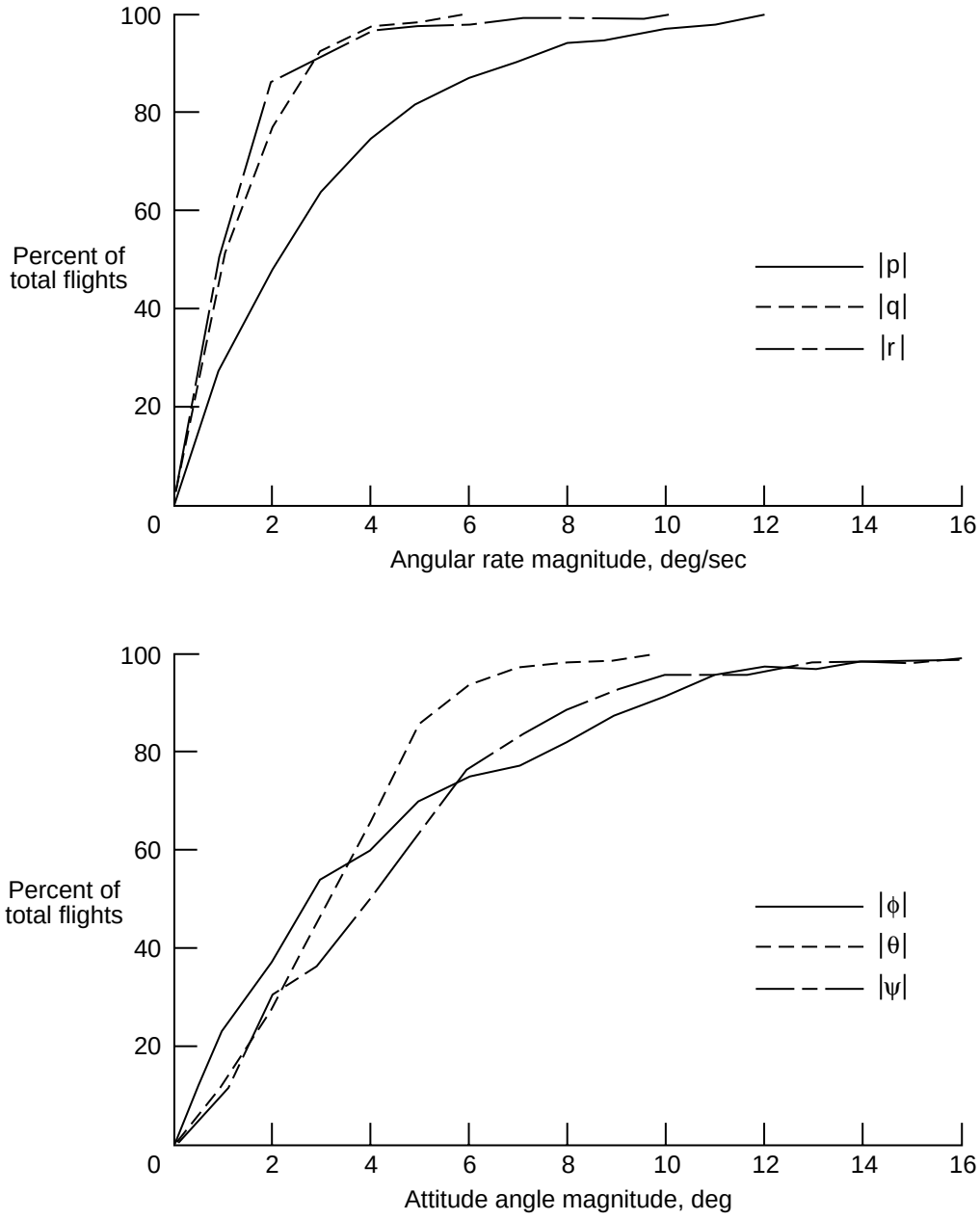

Figure 18. Cumulative frequency distribution of magnitudes of attitude angles and angular rates at middle marker for six pilots.

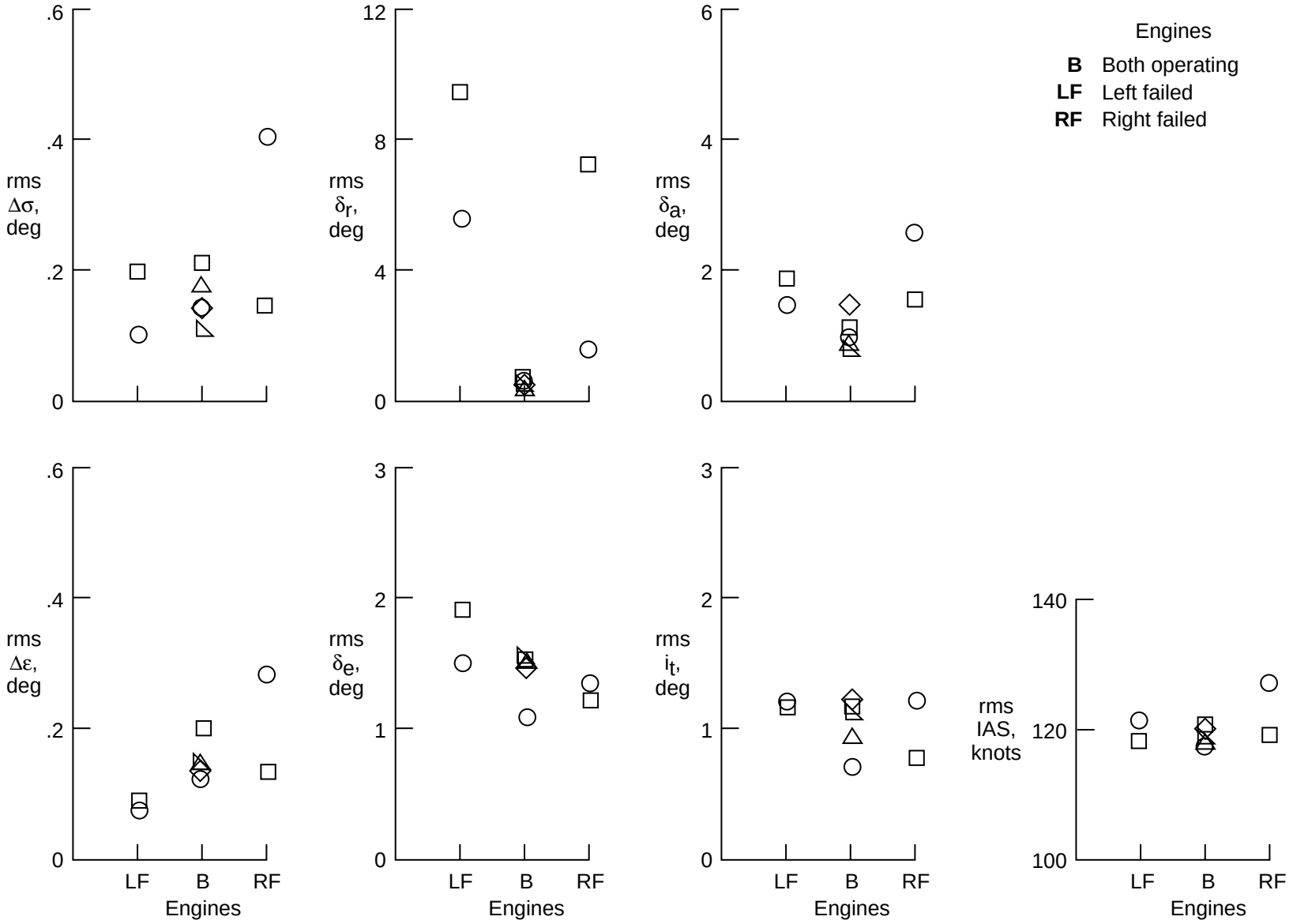

(a) Wind-off data.

Figure 19. The rms values of tracking error, control deflections, and airspeed for flights down glideslope made by pilot B. (Different symbols represent different flights.)

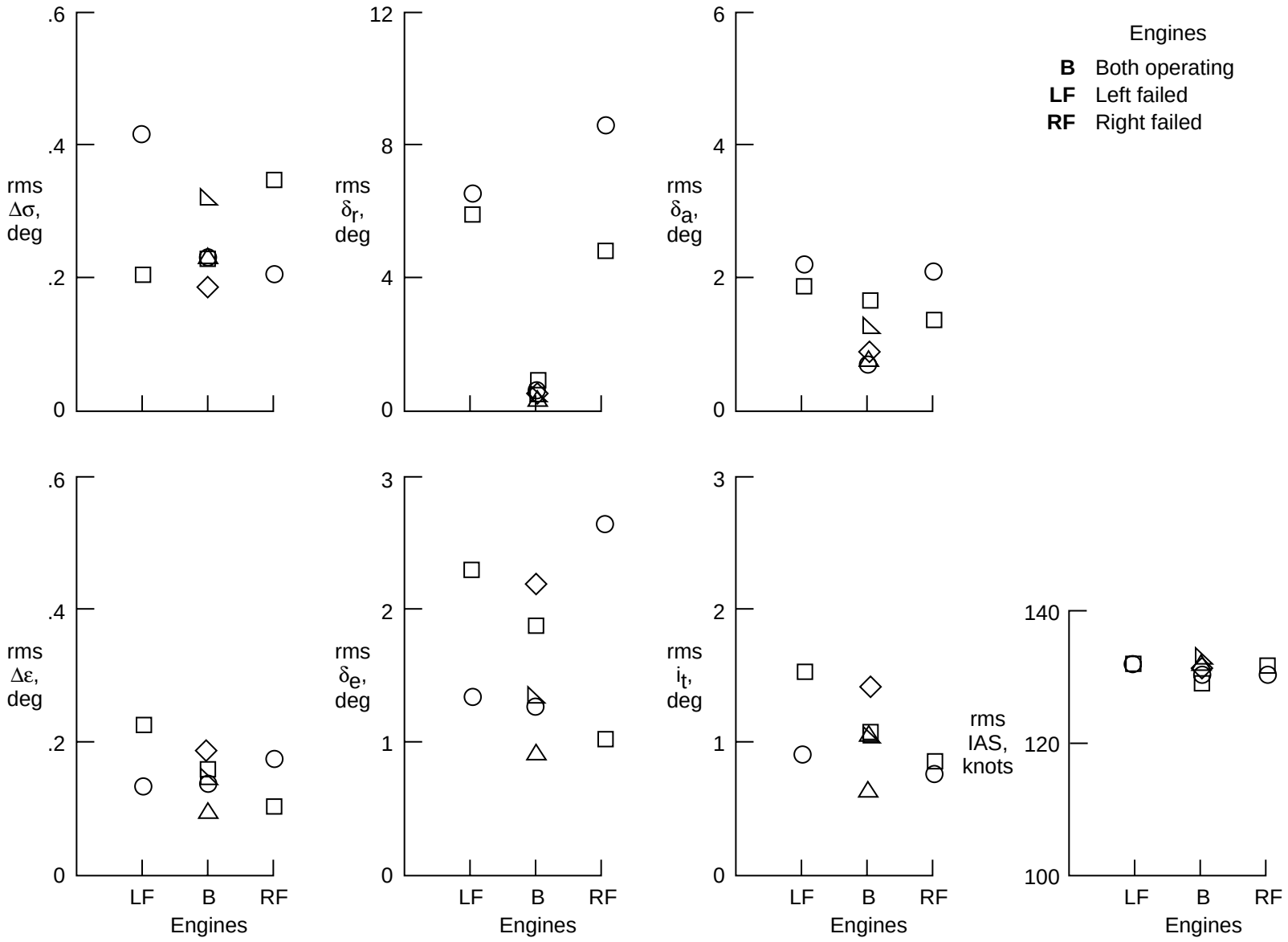

(b) Wind-on data.

Figures 19. Concluded.

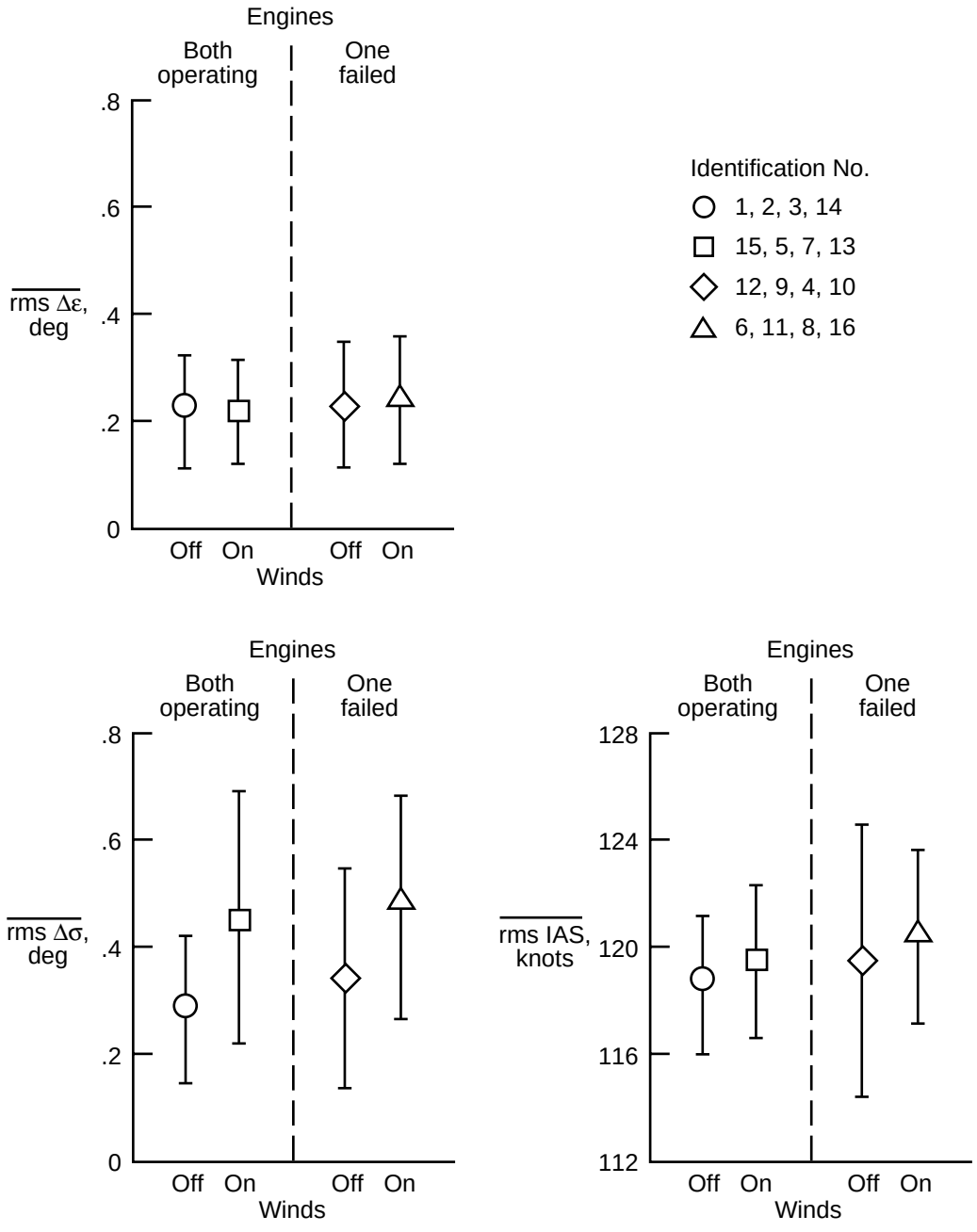

Figure 20. Effect of winds and failed engine on glideslope, localizer, and airspeed rms values for combined result of six pilots (symbols designate mean values, bars designate standard deviation values).

Failure location	Ratings		Identification No.		Ratings		Failure location
	Pilot P	Pilot Y	Wind off	Wind on	Pilot Y	Pilot P	
None	5	5	1	15	3	6	None
None	5	5	2	5	5	6	None
None	5	4	3	7	4	5	None
None	6	3	14	13	5	6	None
None		3	[a]1				None
Left engine out							
h = 1300 ft	5	4	12	6	6	5	h = 1300 ft
h = 1300 ft	6	5	9	11	4	7	h = 1300 ft
Right engine out							
h = 1300 ft	6	4	4	8	5	5	h = 1300 ft
h = 1300 ft	7	5	10	16	4	5	h = 1300 ft

[a]No turbulence.

(a) ILS approach runs.

Figure 21. Cooper-Harper pilot ratings for ILS approach and missed-approach data runs given by research pilots. (See fig. 10 for explanation of ratings.)

Failure location	Ratings		Identification No.		Ratings		Failure location
	Pilot P	Pilot Y	Wind off	Wind on	Pilot Y	Pilot P	
None	4	6	2	5	5	4	None
Left engine out							
MAP	6	5	3	7	4	5	MAP
h = 1300 ft	6	5	1	11	4	7	h = 1300 ft
Right engine out							
MAP	5	4	14	13	4	5	MAP
h = 1300 ft	7	4	10	16	4	5	h = 1300 ft

(b) Missed approach runs.

Figure 21. Concluded.

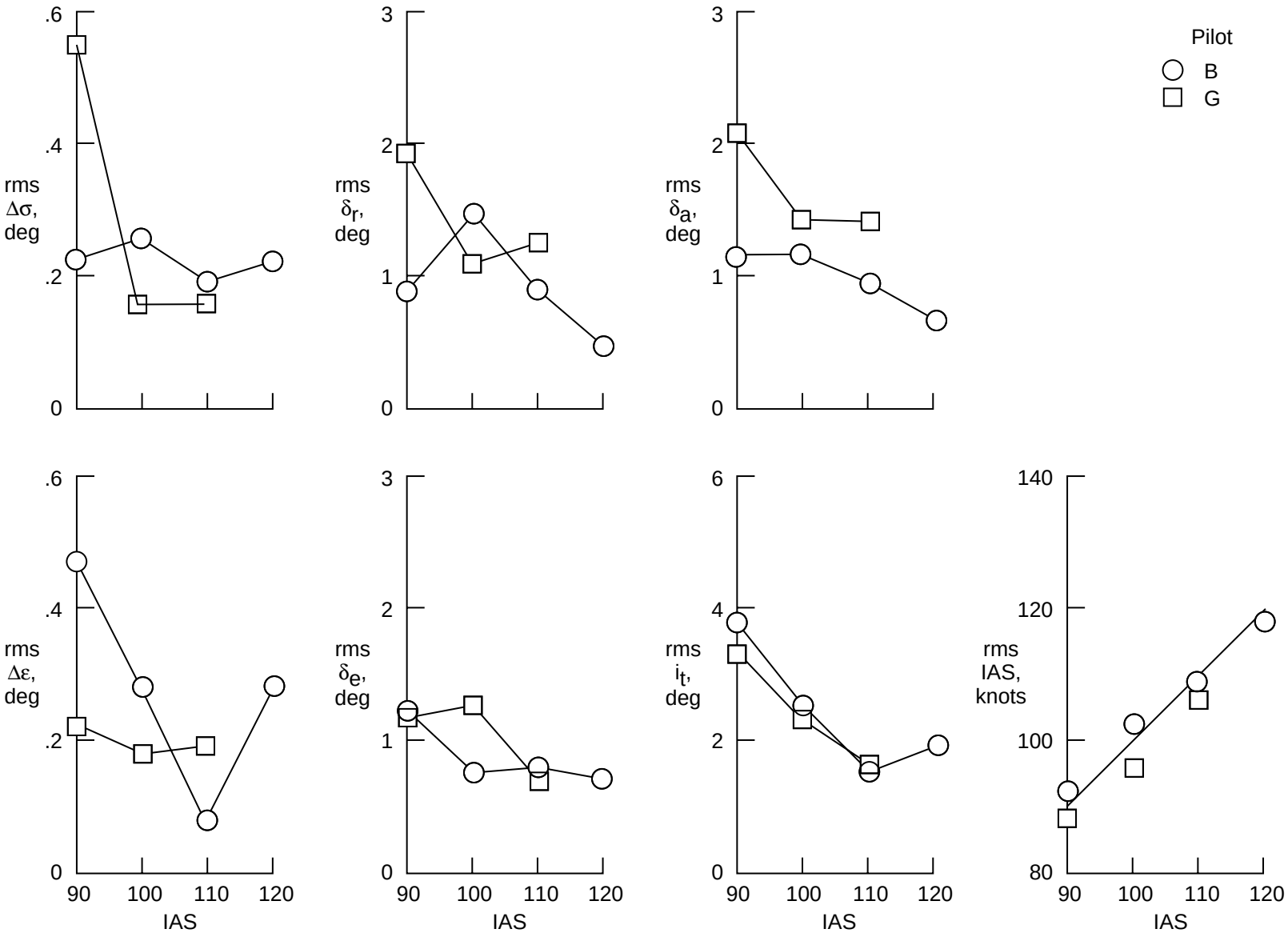

Figure 22. Effect of approach speed on rms performance measured down glideslope from outer marker to middle marker, no winds, no turbulence.

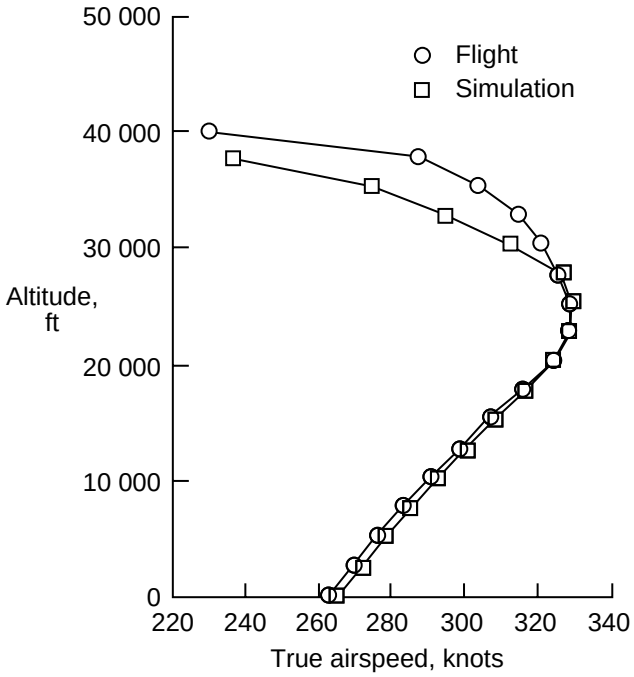

(a) Maximum true airspeed.

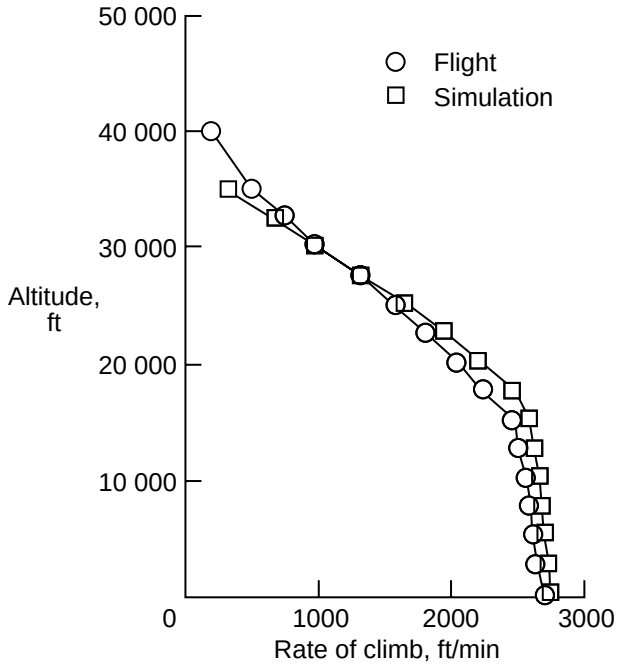

(b) Maximum rate of climb.

Figure 23. Simulation and flight derived values of two performance measures.

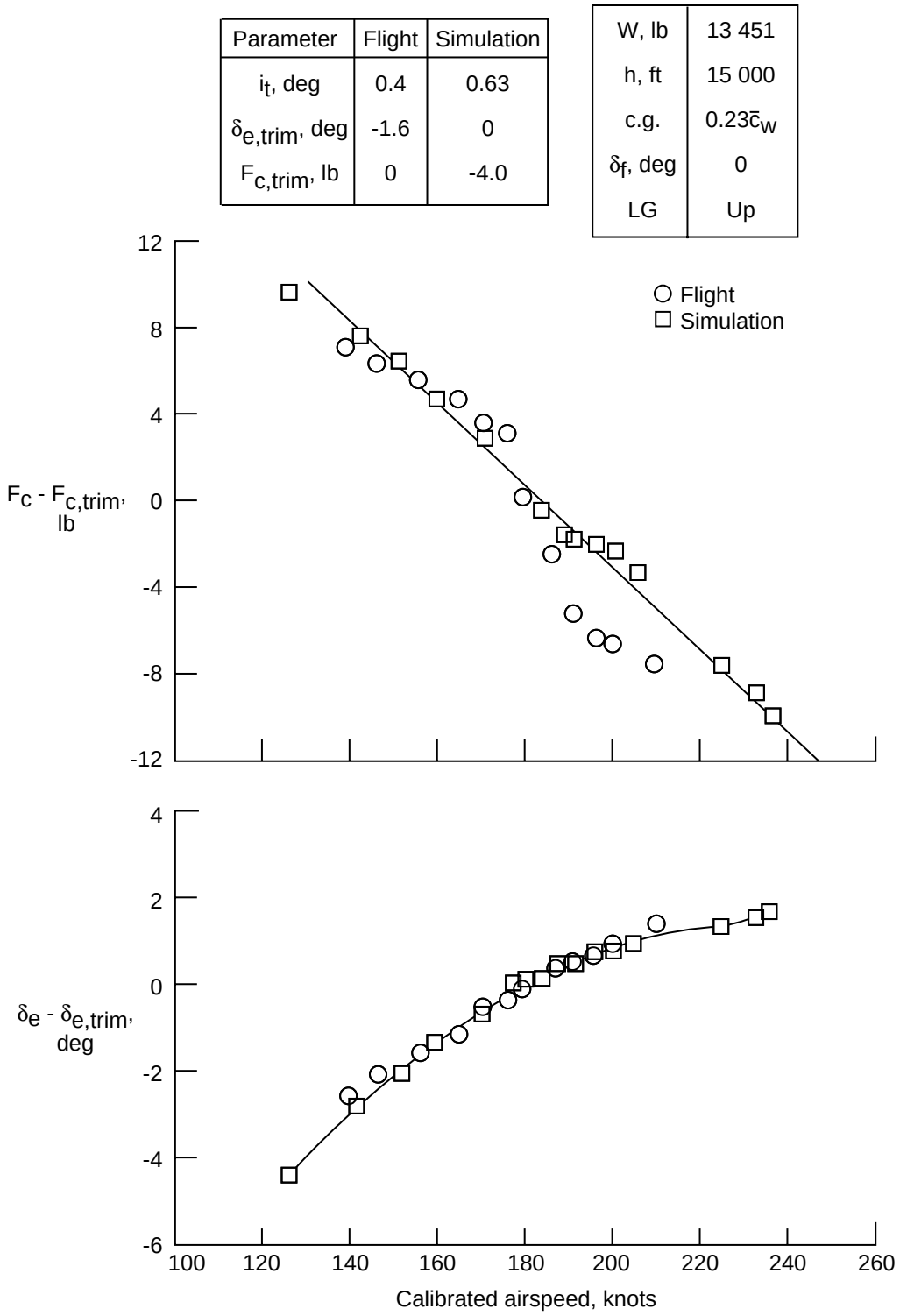

(a) Mid c.g. location, trim speed 180 knots.

Figure 24. Longitudinal stability comparison of flight test and simulator results for cruise configuration.

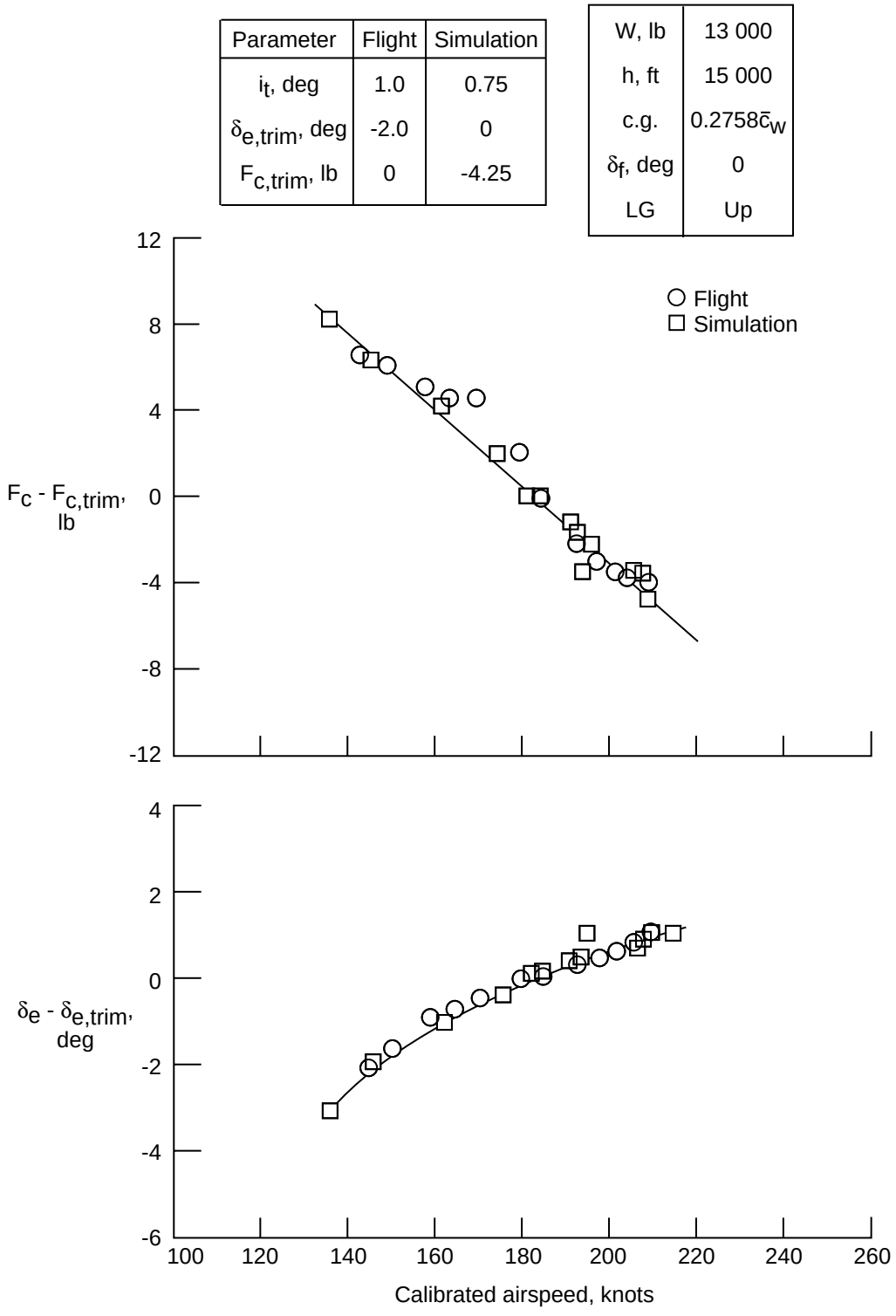

(b) Aft c.g. location, trim speed 185 knots.

Figure 24. Concluded.

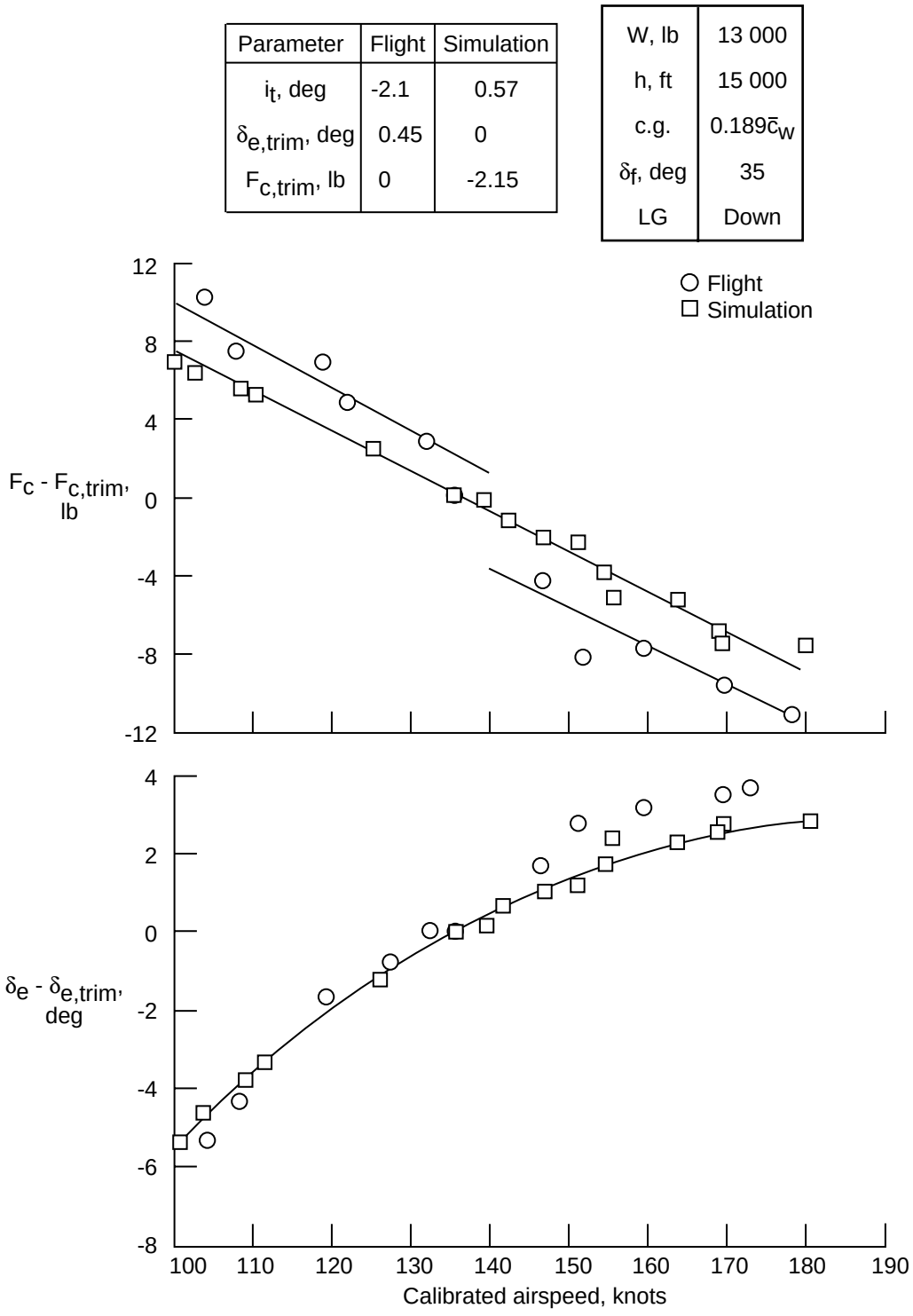

(a) Forward c.g. location, trim speed 136 knots.

Figure 25. Longitudinal stability comparison of flight test and simulator results for landing configuration.

Parameter	Flight	Simulation
i_t, deg	-1.3	0.28
$\delta_{e,trim}$, deg	0.4	0
$F_{c,trim}$, lb	0	-1.94

W, lb	13 451
h, ft	15 000
c.g.	$0.23\bar{c}_w$
δ_f, deg	35
LG	Down

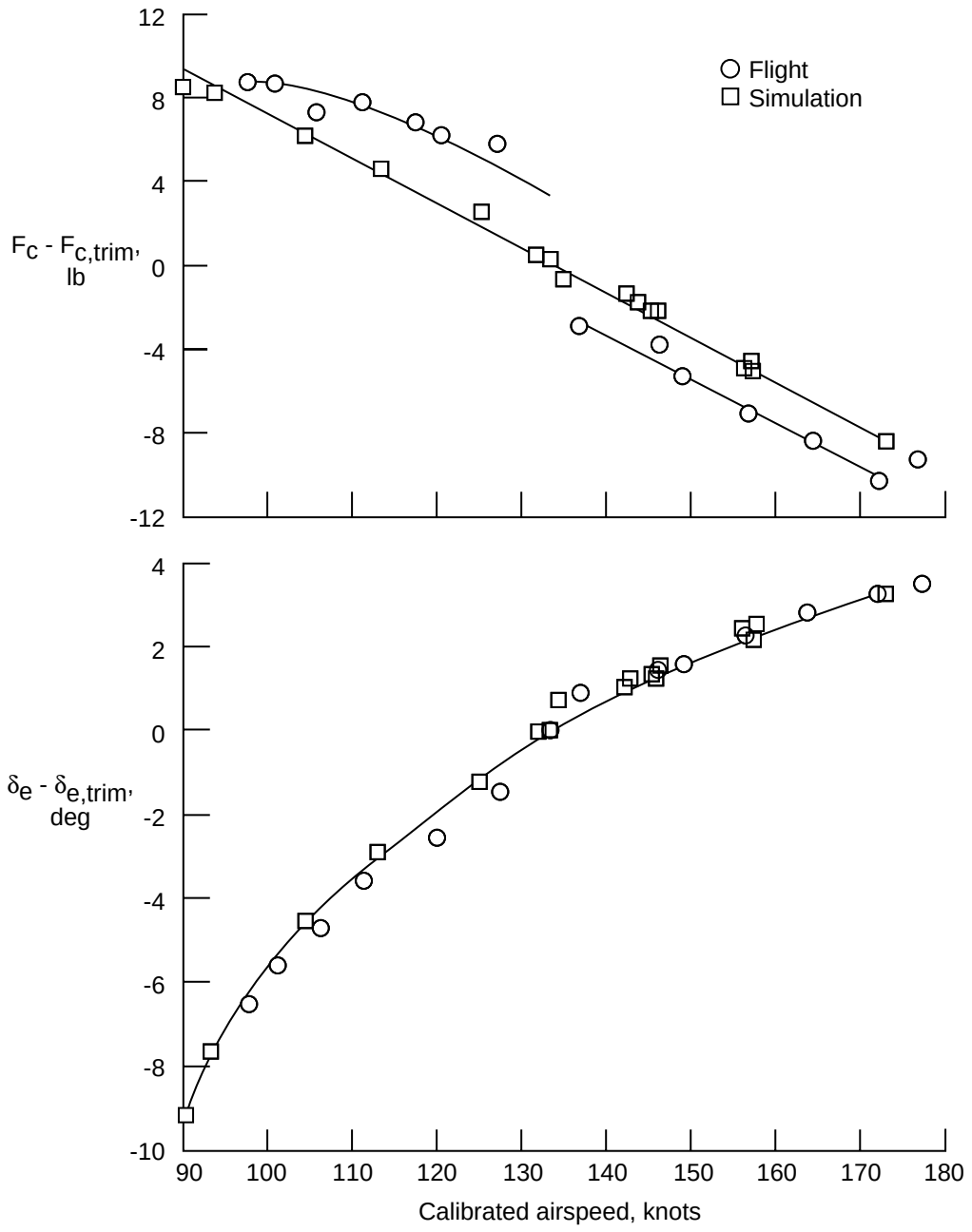

(b) Mid c.g. location, trim speed 133 knots.

Figure 25. Continued.

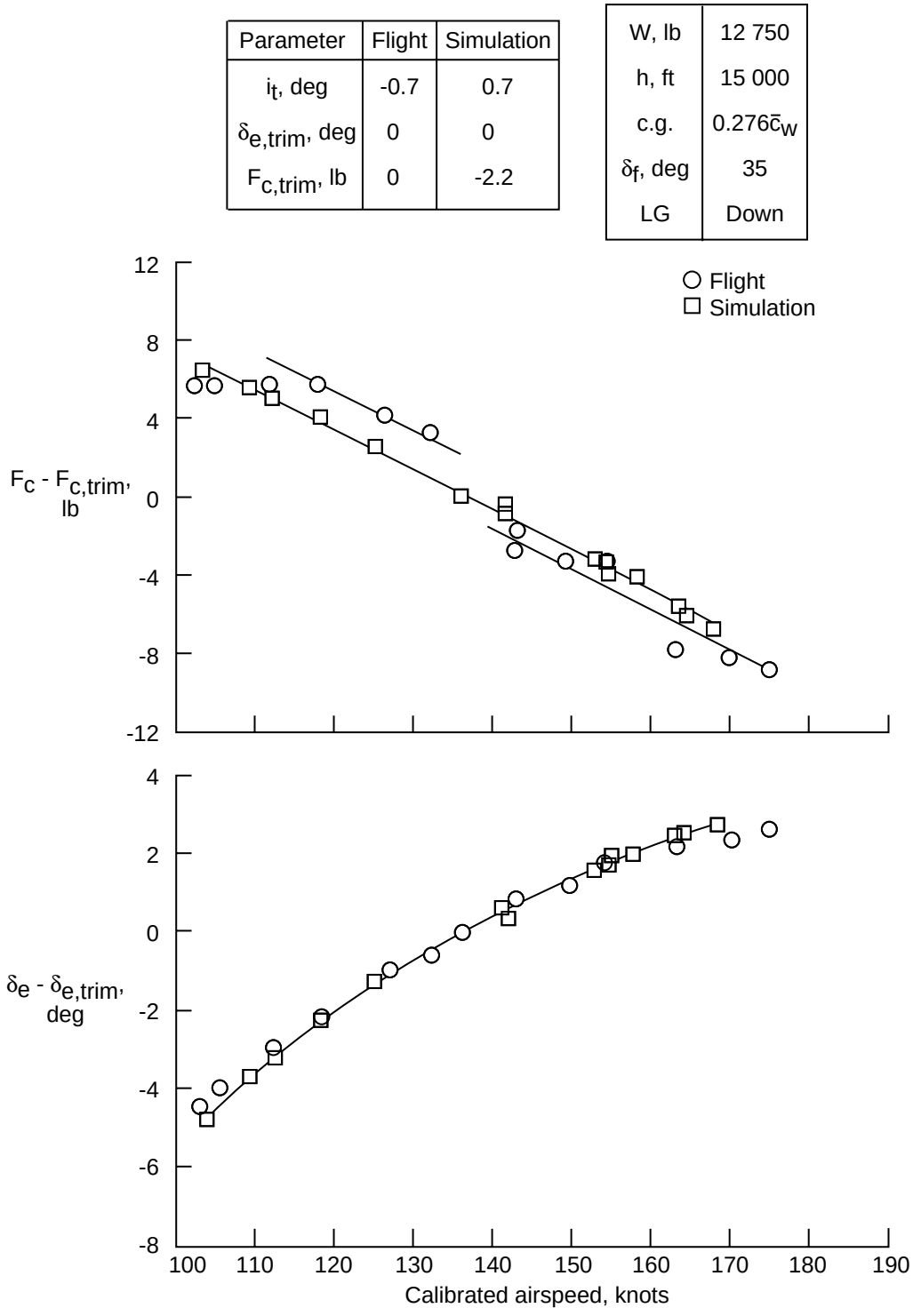

(c) Aft c.g. location, trim speed 136 knots.

Figure 25. Concluded.

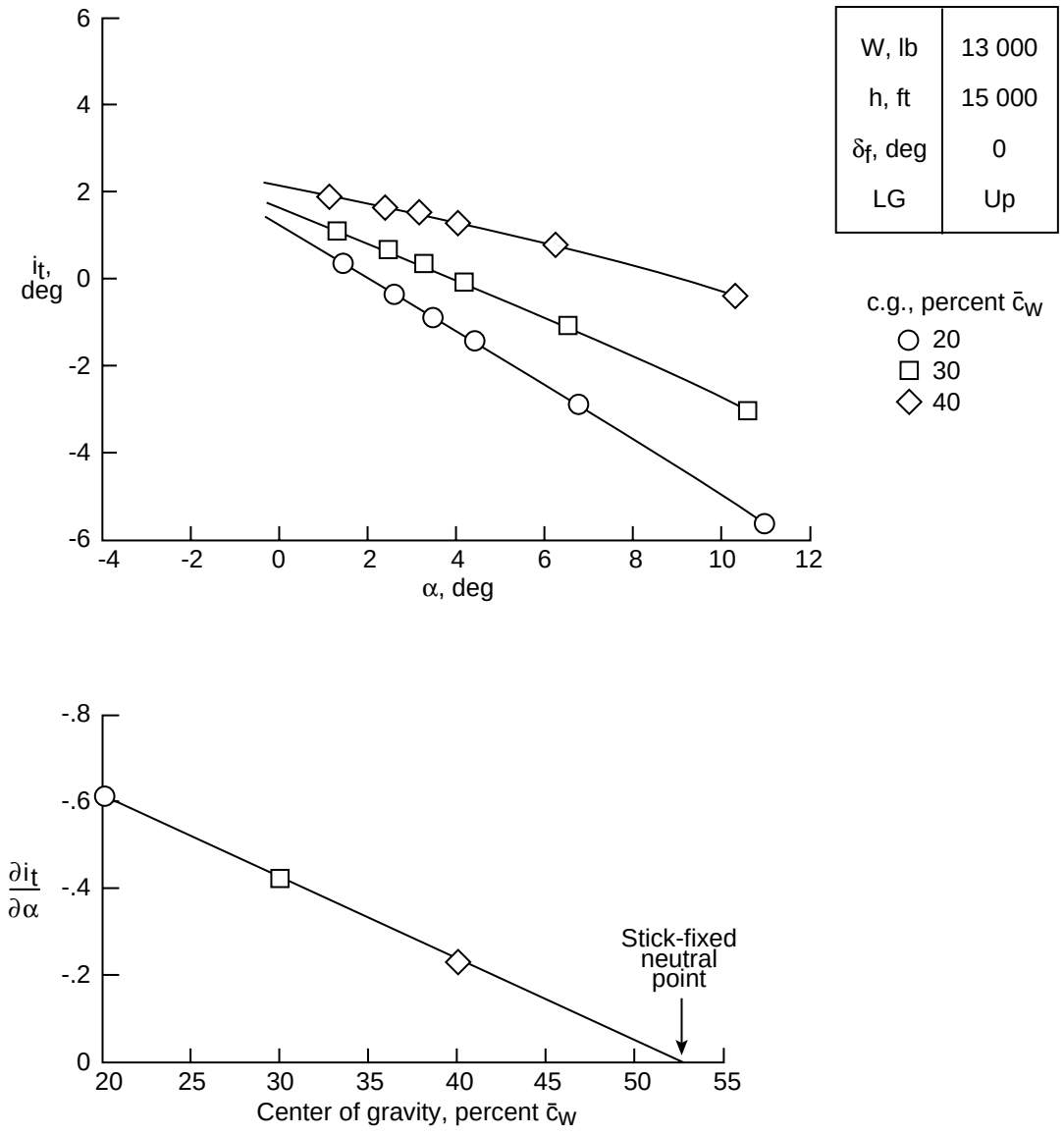

(a) Cruise configuration.

Figure 26. Stick-fixed neutral point determined from simulator trim conditions for straight and level flight.

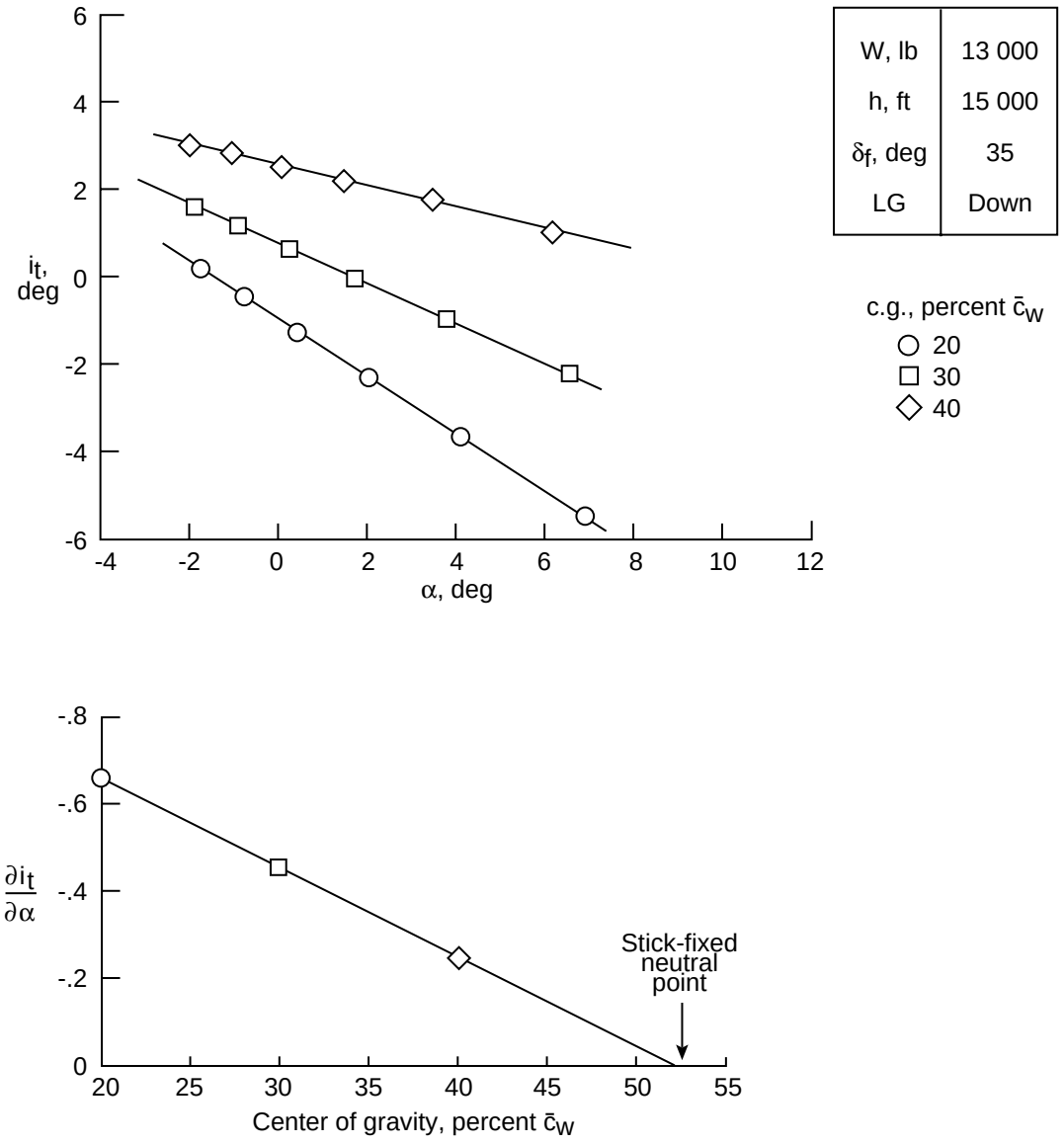

(b) Landing configuration.

Figure 26. Concluded.

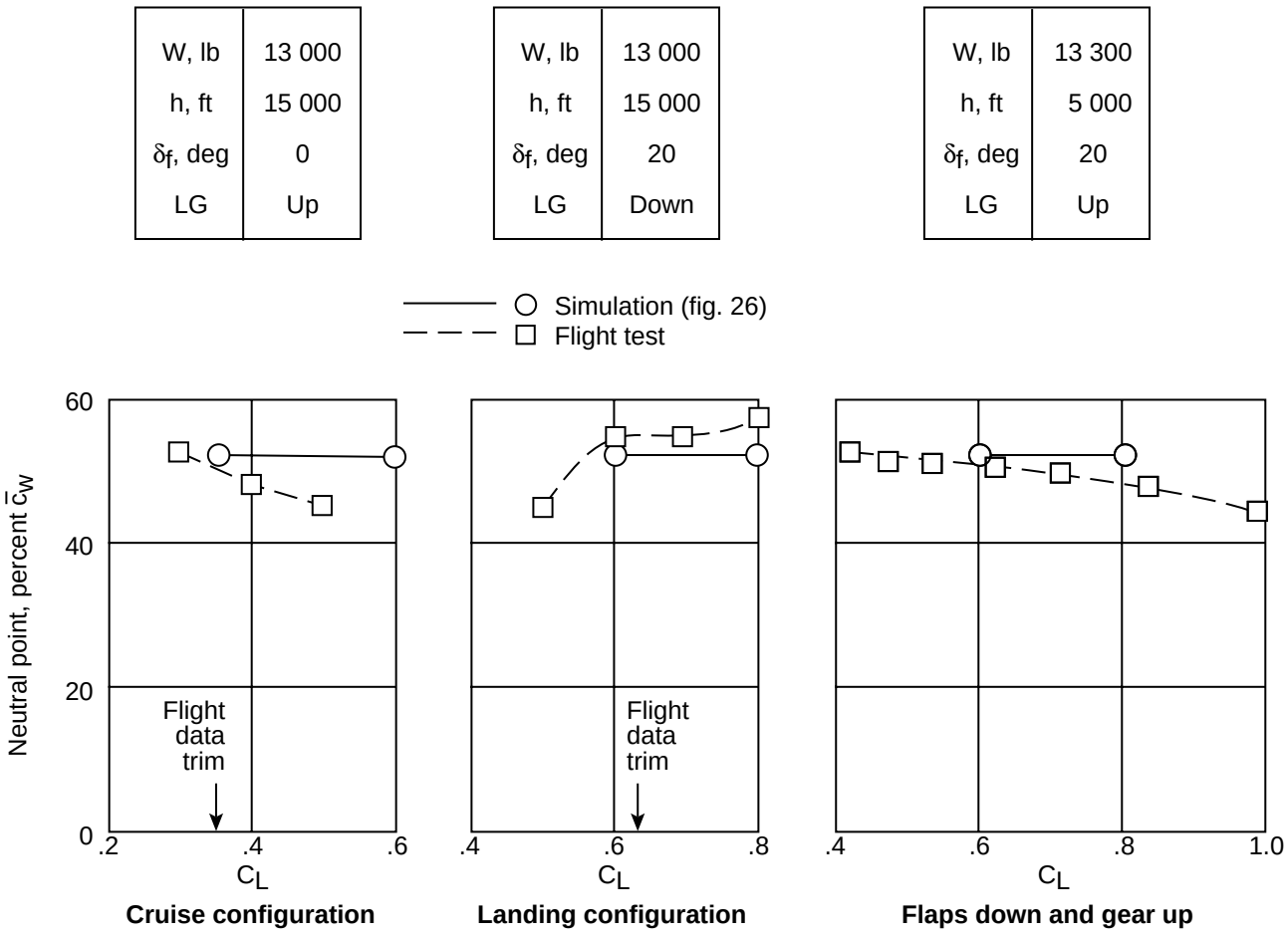

Figure 27. Stick-fixed neutral point values determined by simulator and flight test results.

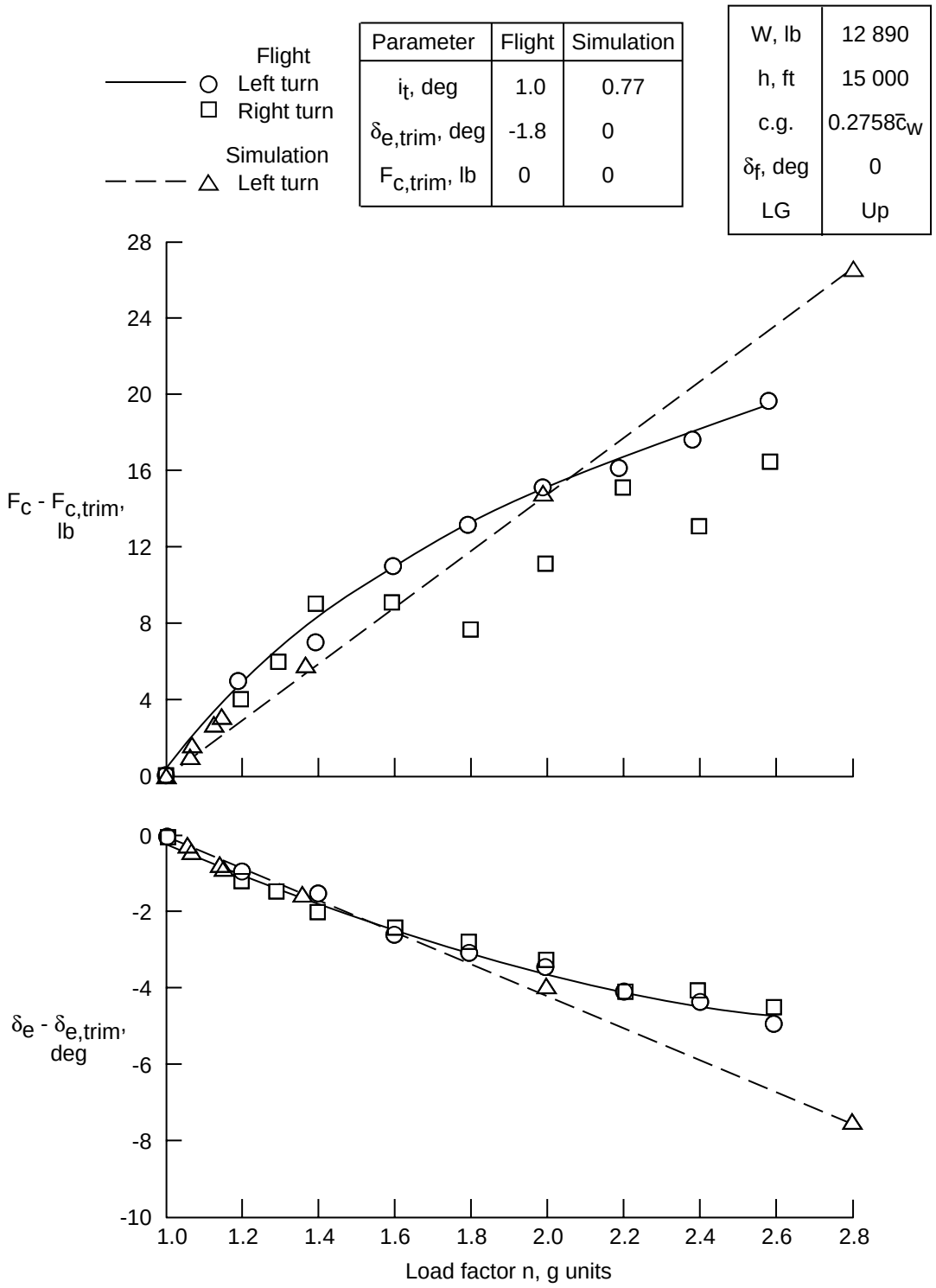

Figure 28. Maneuver stability of flight test and simulator results for cruise configuration, trim speed is 185 knots.

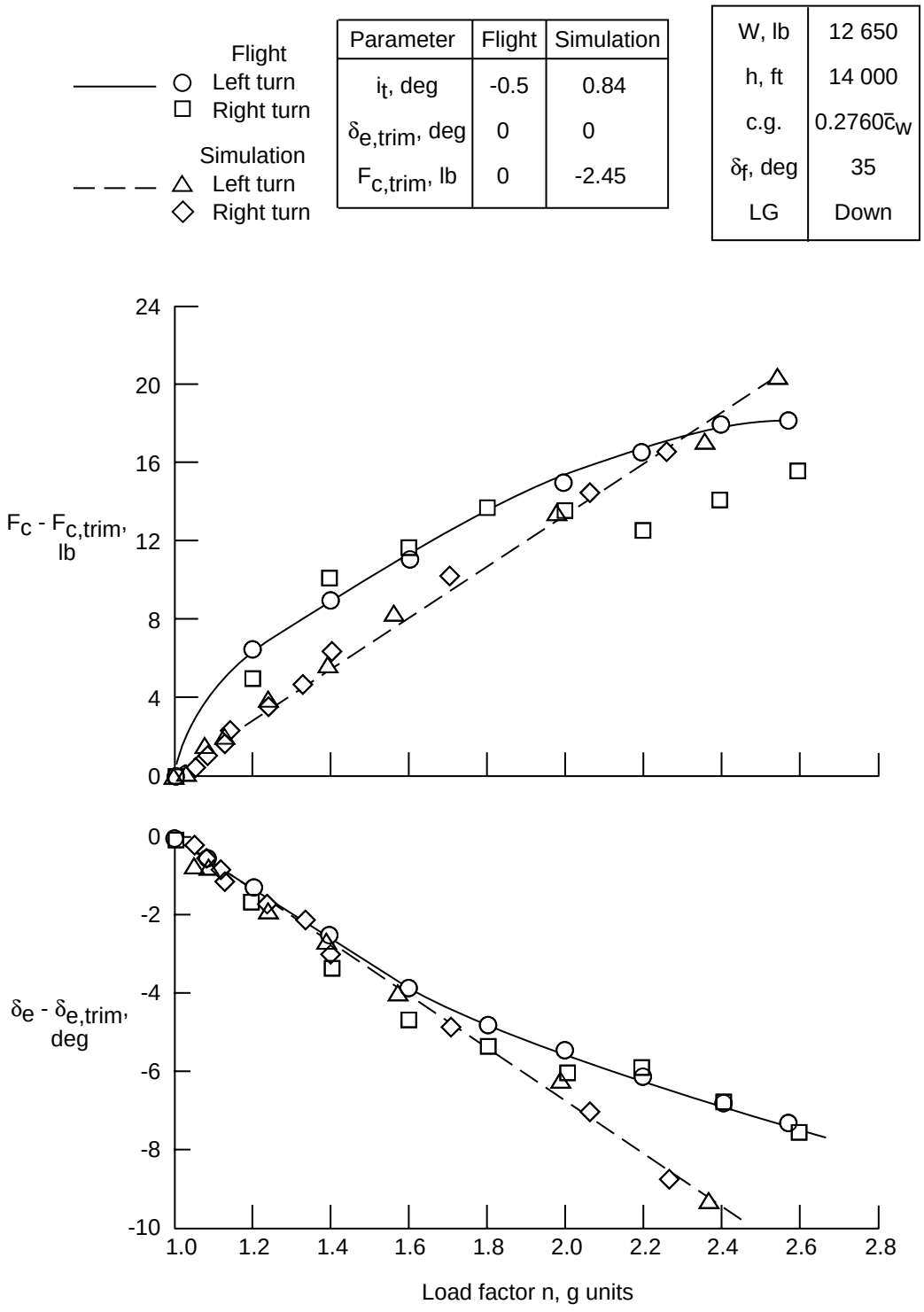

Figure 29. Maneuver stability of flight test and simulator results for landing configuration, trim speed is 140 knots.

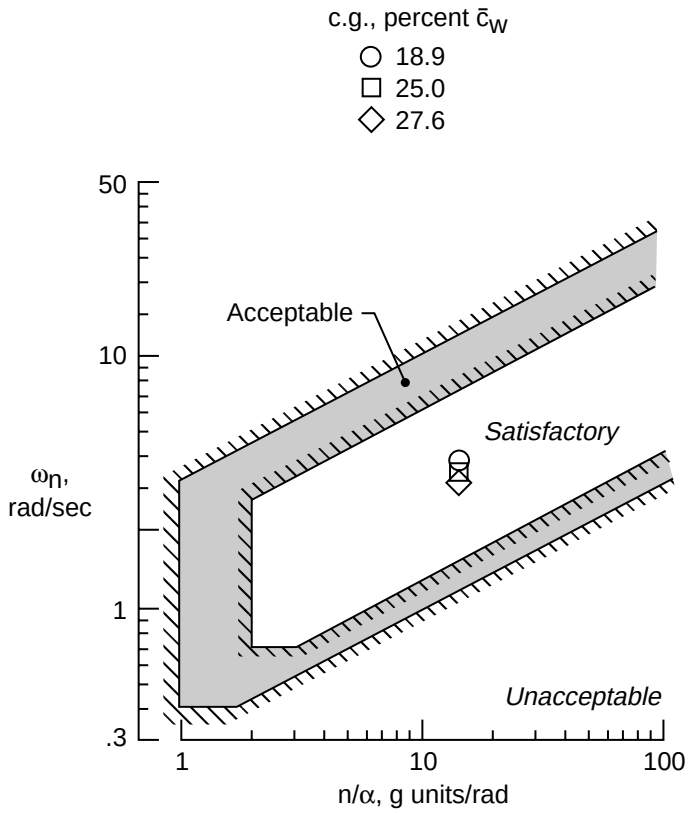

(a) Criterion from reference 20.

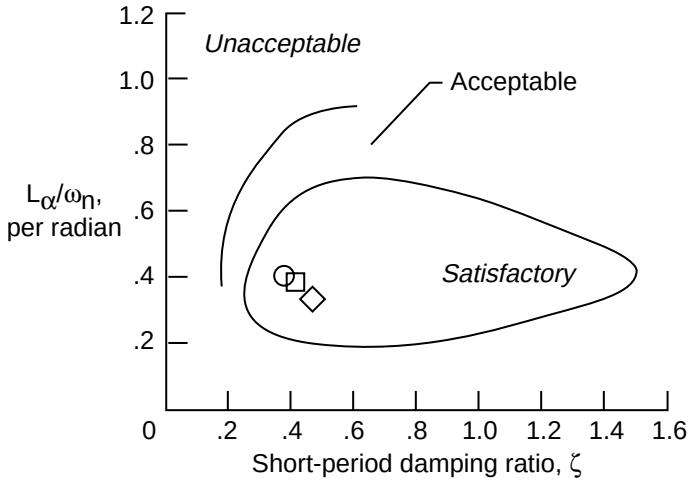

(b) Criterion from reference 21.

Figure 30. Short-period longitudinal flying qualities criteria for cruise configuration.

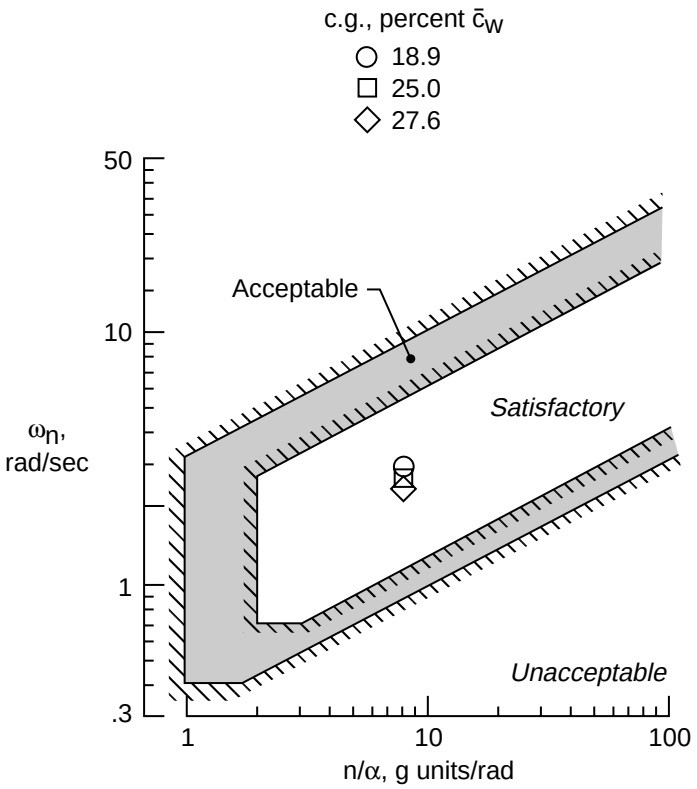

(a) Criterion from reference 20.

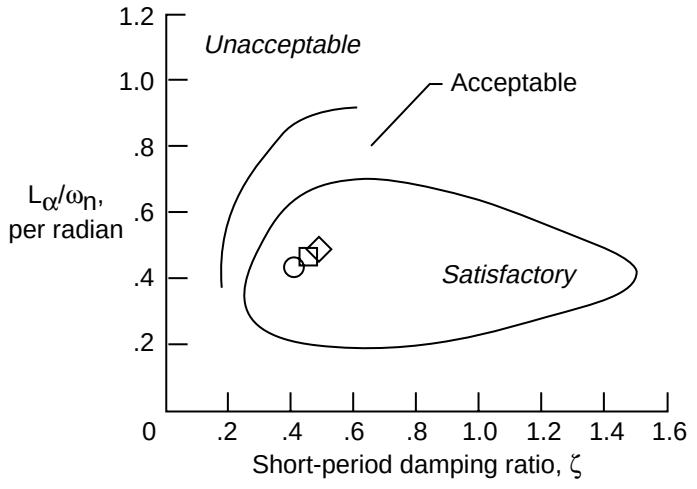

(b) Criterion from reference 21.

Figure 31. Short-period longitudinal flying qualities criteria for landing configuration.

Item	Flight	Simulation
W, lb	13 000	13 000
h, ft	35 000	35 000
c.g.	$0.278\bar{c}_w$	$0.278\bar{c}_w$
δ_f, deg	0	0
LG	Up	Up
CAS	175	171
Period	64	63.32
ω_n	0.0984	0.0994
ζ	0.057	0.0538

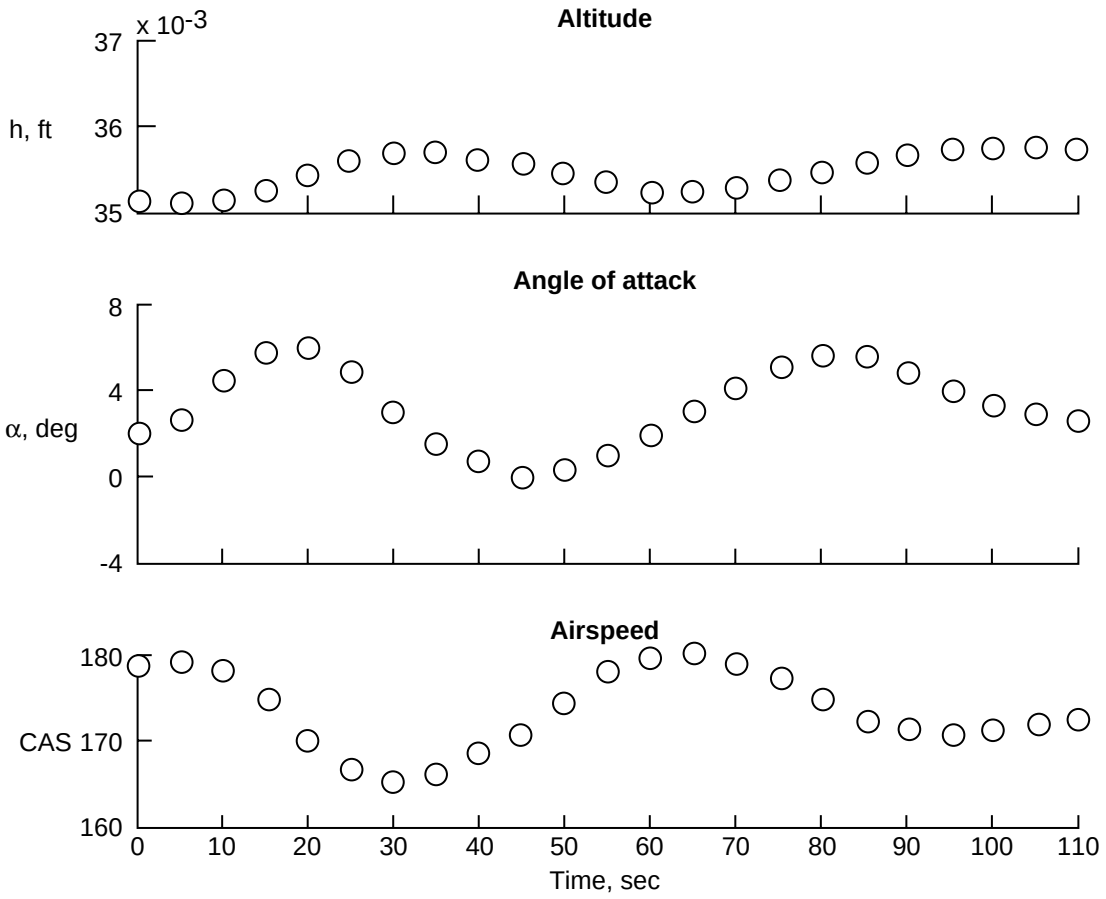

Figure 32. Time history of phugoid motion of ATPTB aircraft copied from flight records and a comparison of resulting flight values with those of simulation.

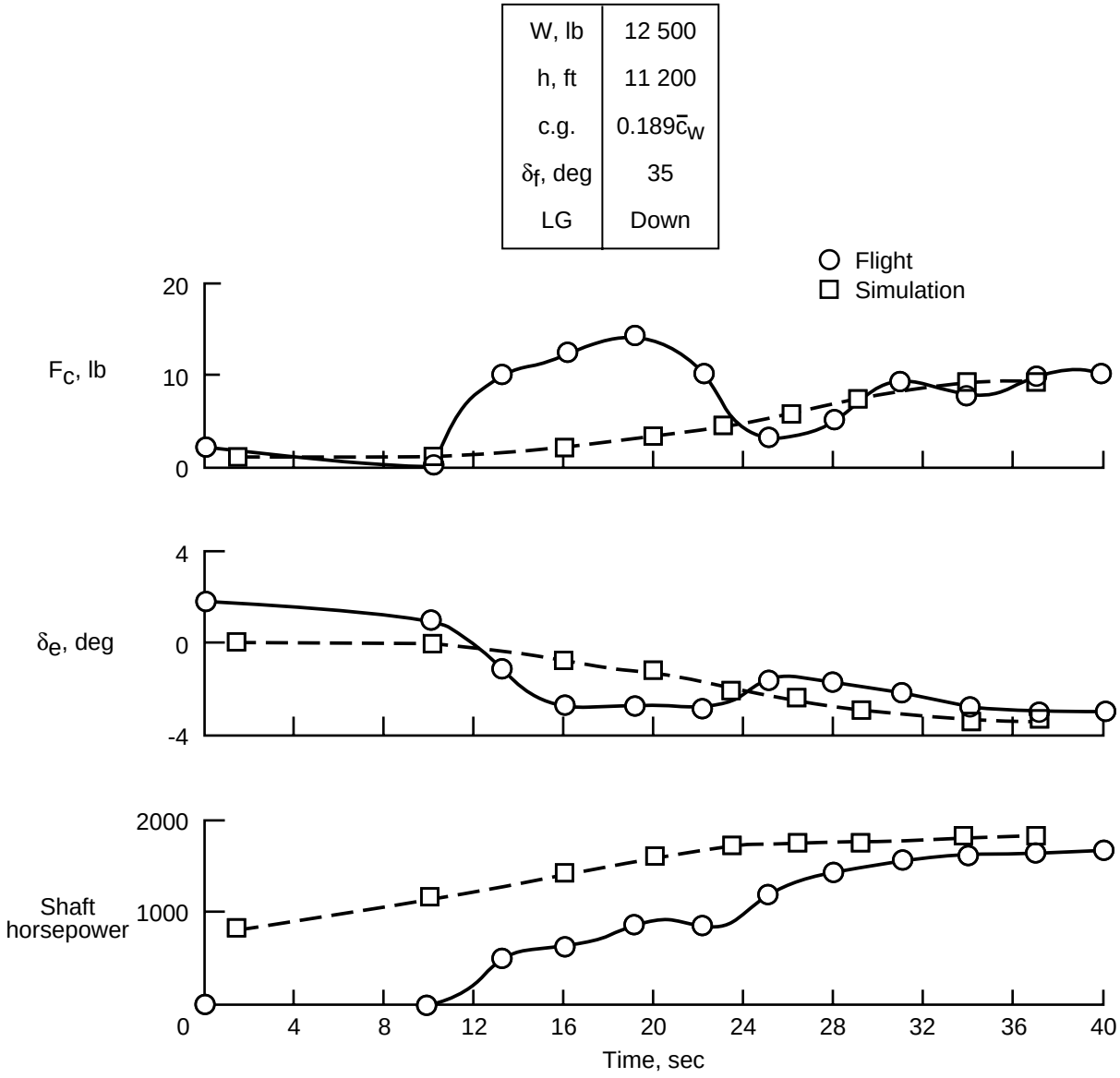

Figure 33. Simulator and flight test data for trim change with thrust application (115 CAS).

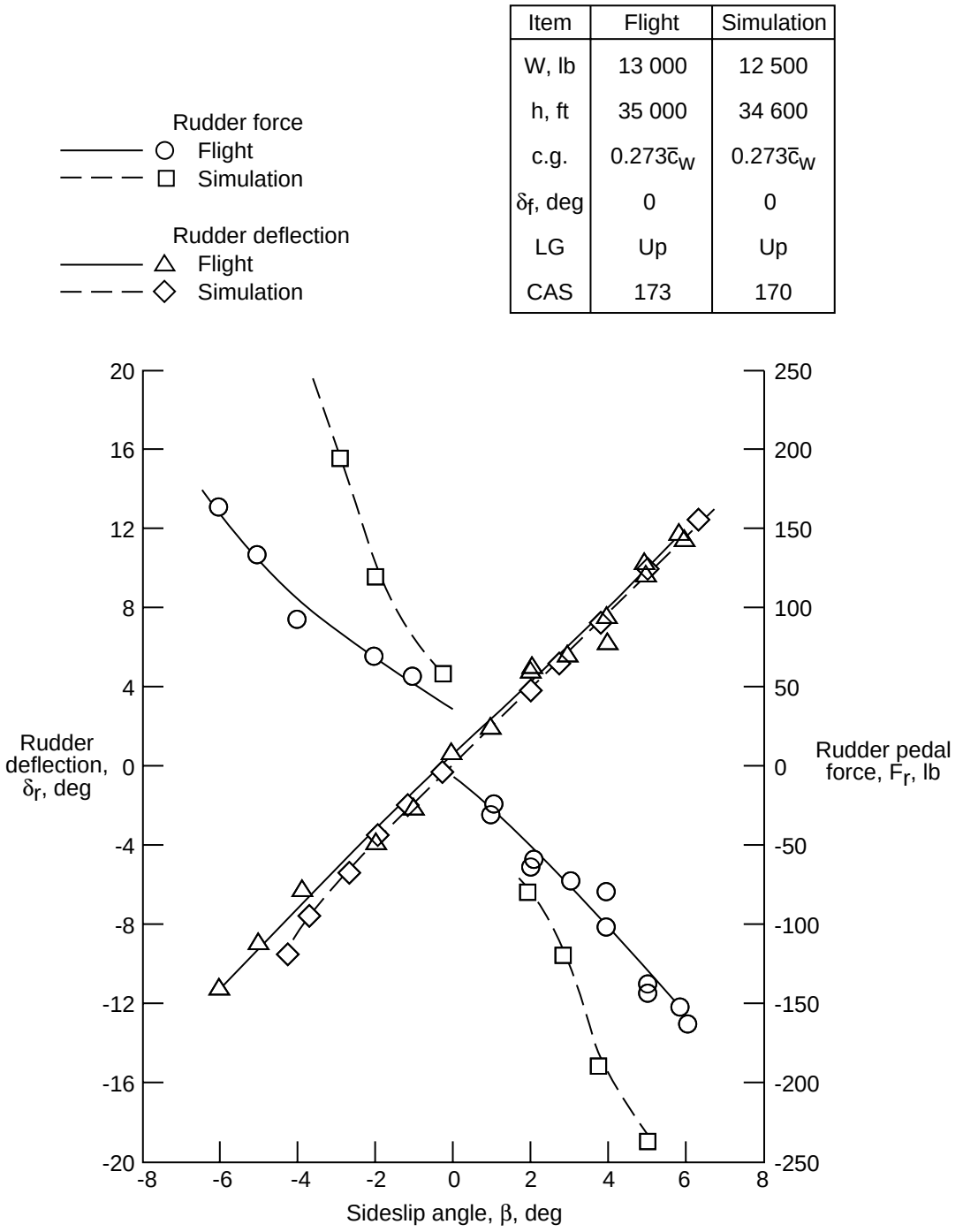

(a) Cruise configuration.

Figure 34. Directional stability data for simulator and flight tests.

Item	Flight	Simulation
W, lb	12 750	12 750
h, ft	14 700	14 700
c.g.	$0.276\bar{c}_w$	$0.276\bar{c}_w$
δ_f, deg	0	0
LG	Down	Down
CAS	138	138

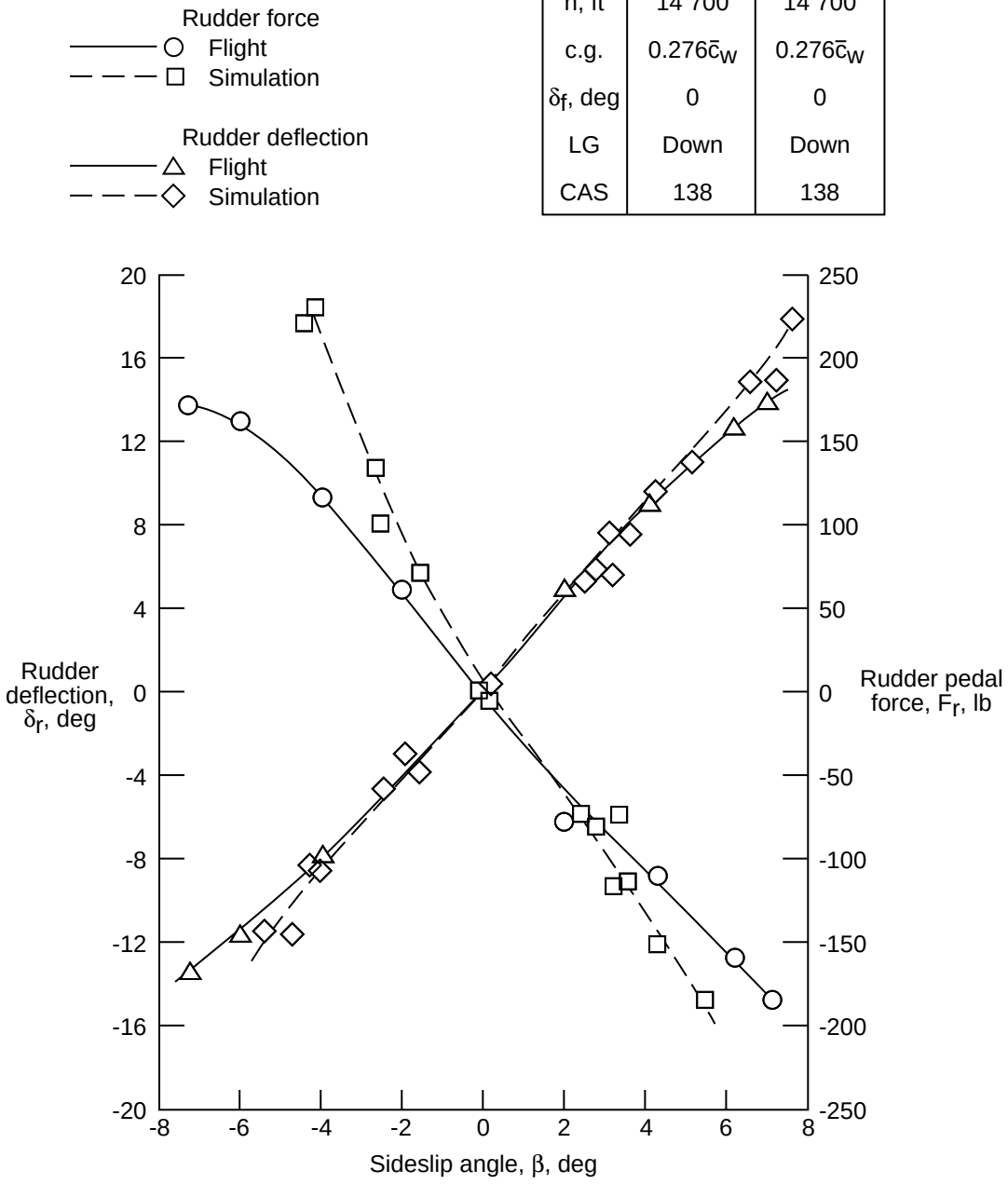

(b) Landing configuration.

Figure 34. Concluded.

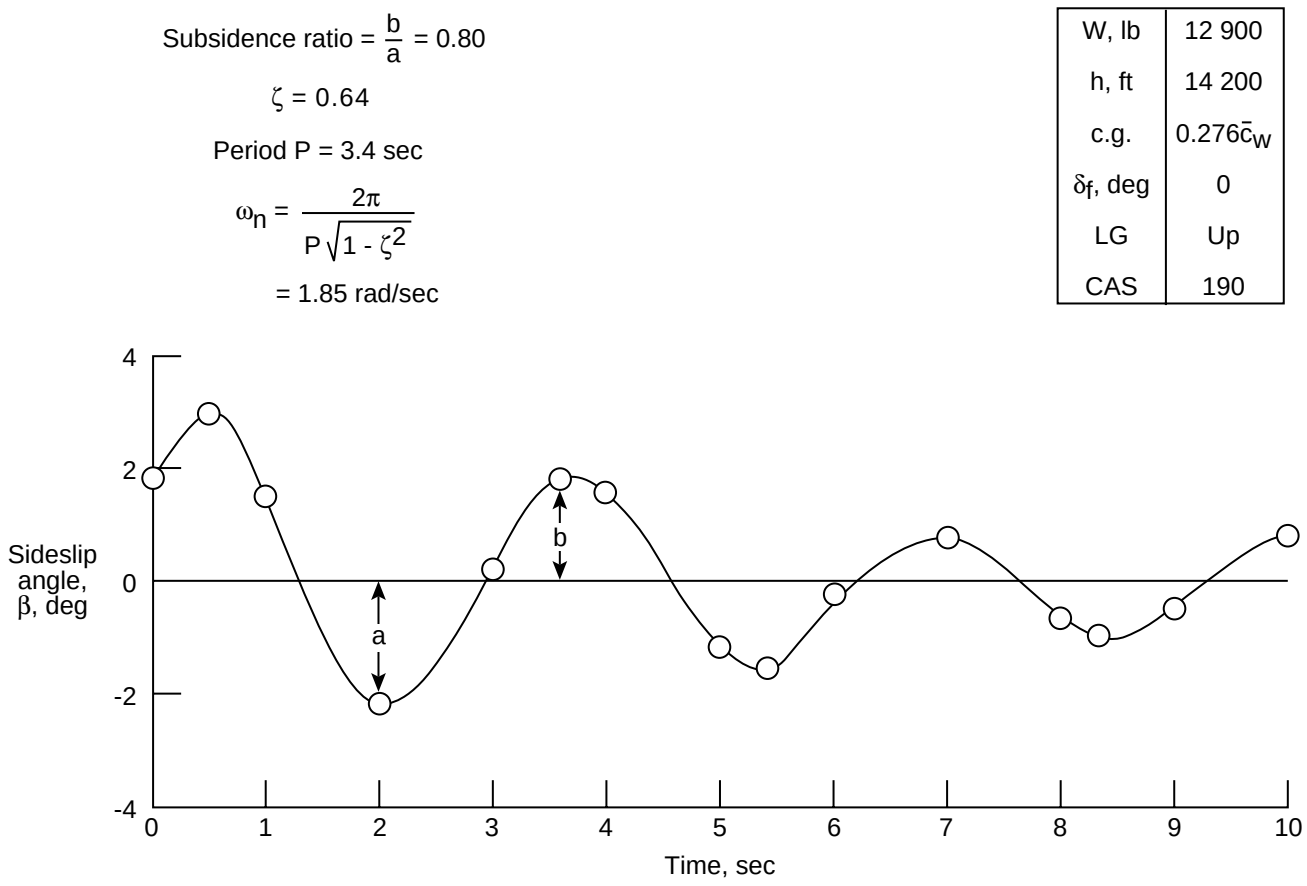

Figure 35. Typical sideslip angle trace constructed by Cessna from flight test data to evaluate Dutch roll characteristics, controls free.

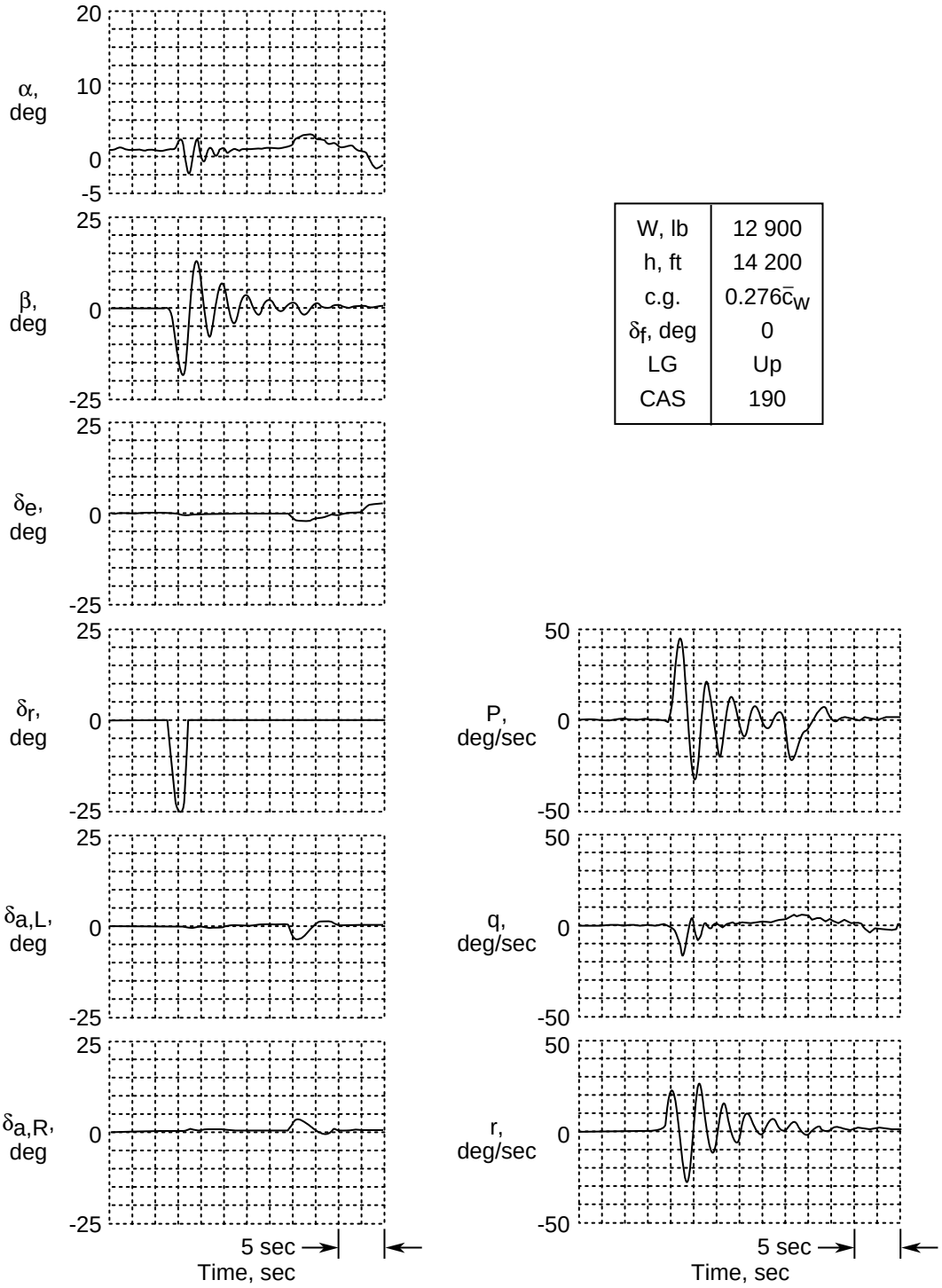

Figure 36. Typical simulation time-history traces for Dutch roll motion for cruise configuration, controls held fixed.

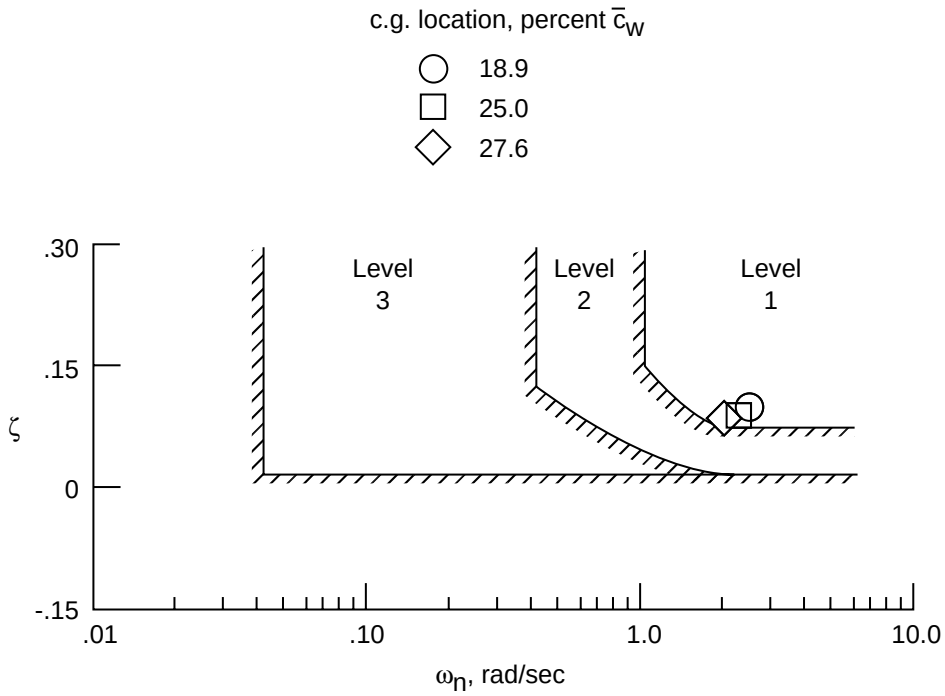

(a) Cruise configuration.

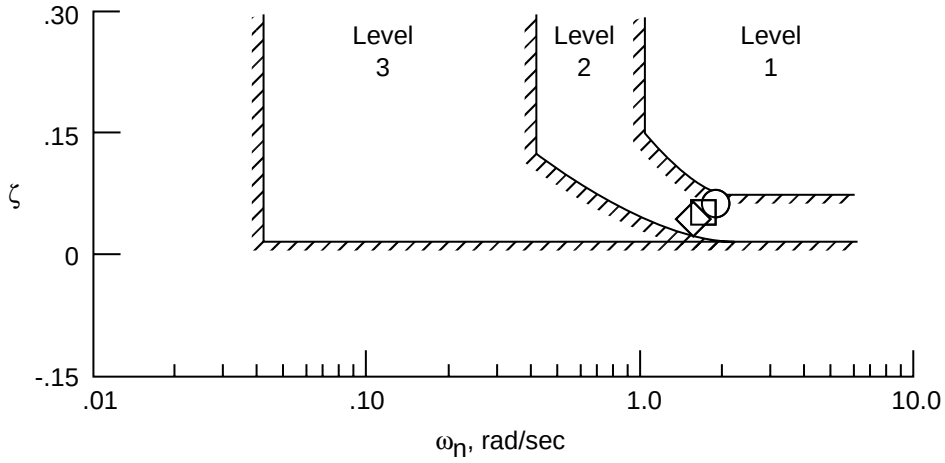

(b) Landing configuration.

Figure 37. Dutch roll flying qualities. Requirements from reference 20.

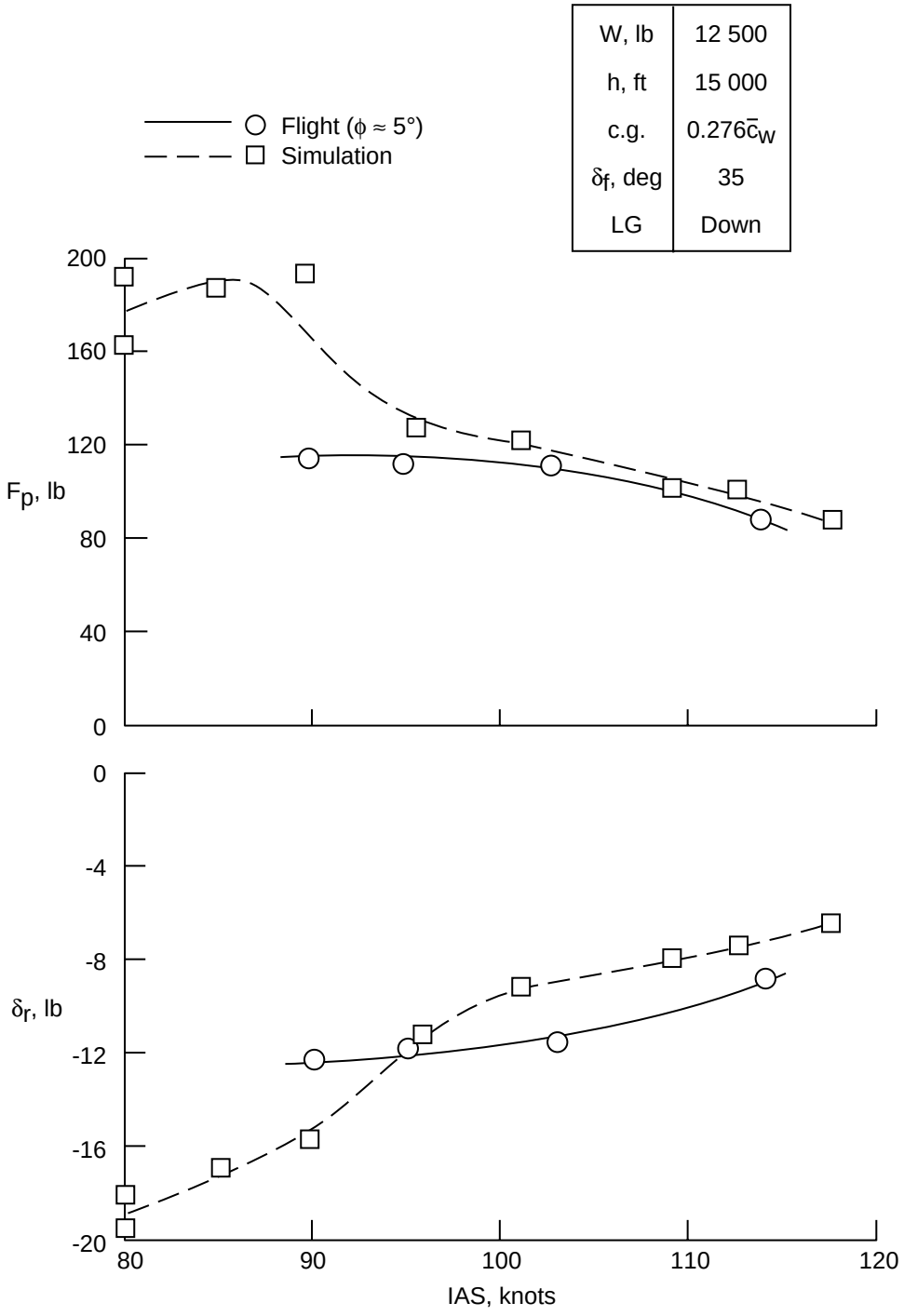

Figure 38. Simulation and flight test data for landing configuration with left engine failed, propeller feathered.

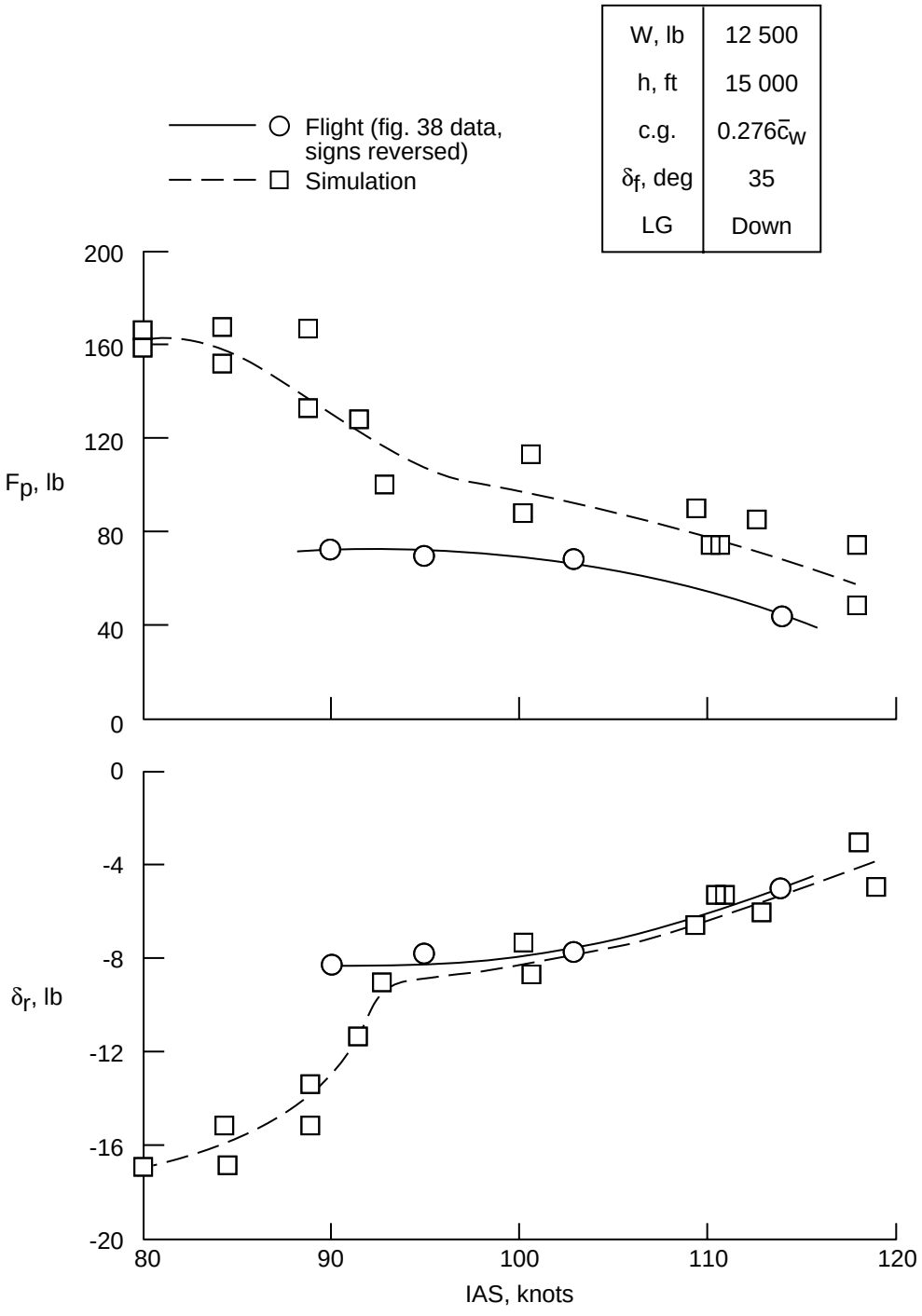

Figure 39. Simulation and flight test data for landing configuration with right engine failed, propeller feathered.

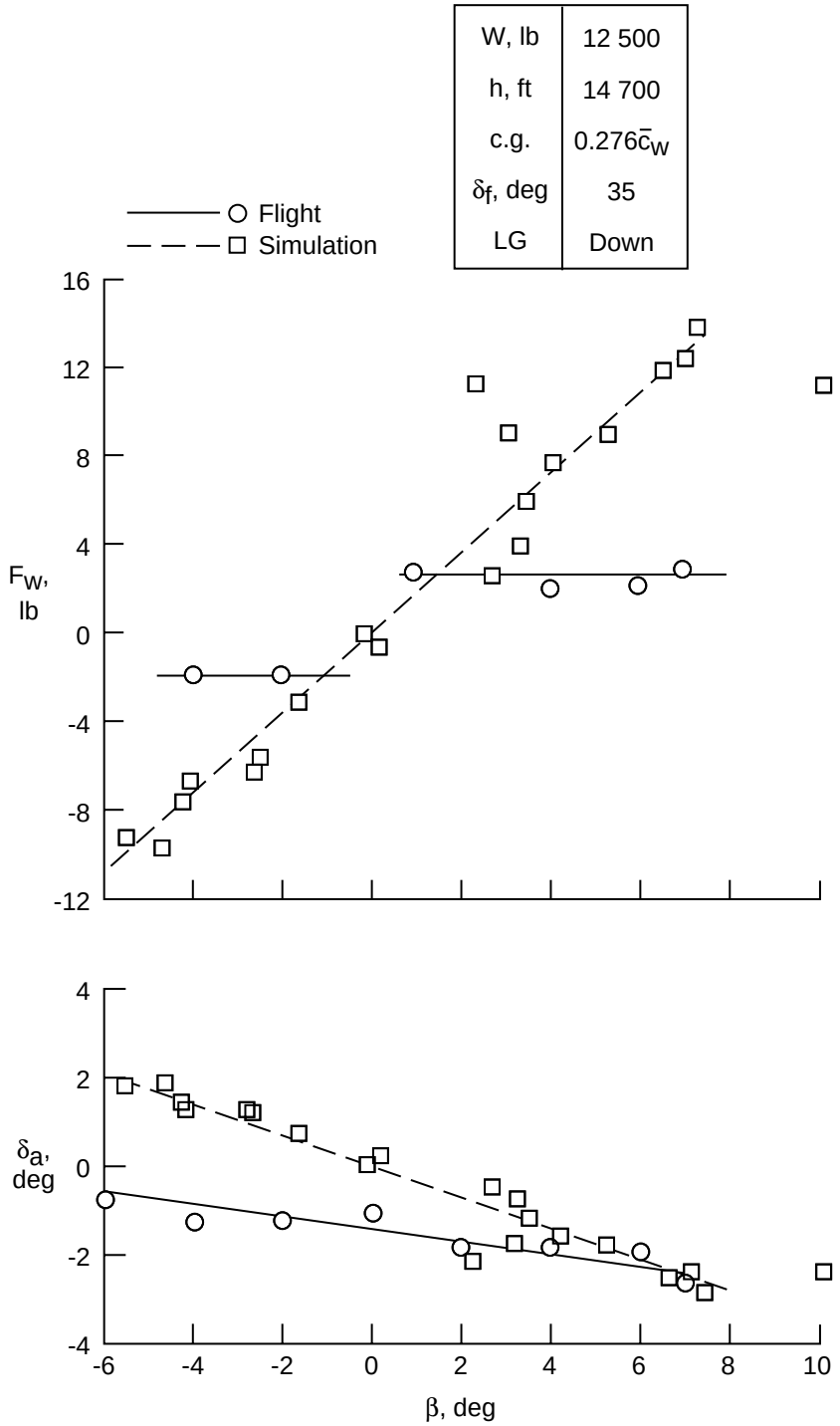

(a) Landing configuration.

Figure 40. Simulation and flight test data for variation of aileron deflection and wheel force with sideslip.

Flight	
W, lb	
h, ft	10 000
c.g.	$0.276\bar{c}_w$
δ_f, deg	0
LG	Up
IAS	145

Simulation	
W, lb	12 500
h, ft	14 700
c.g.	$0.276\bar{c}_w$
δ_f, deg	35
LG	Down
IAS	138

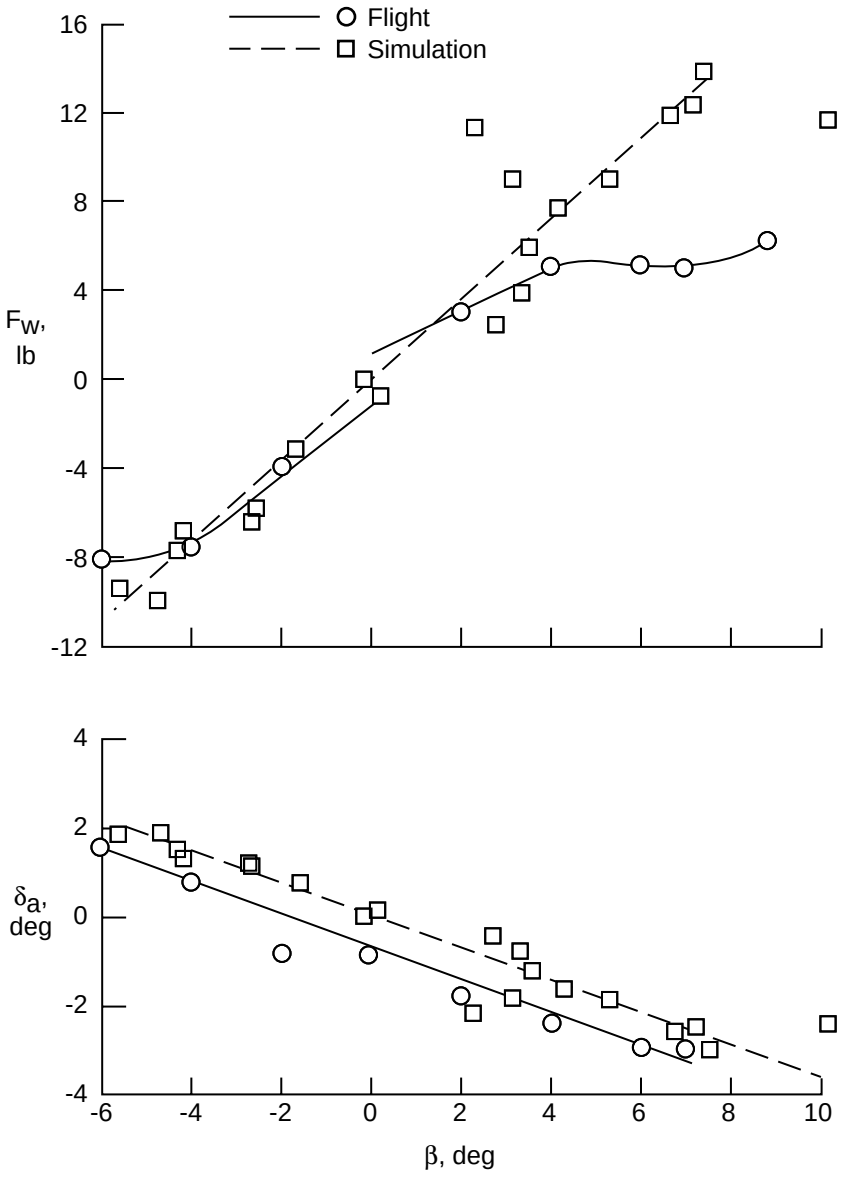

(b) Landing and cruise configuration.

Figure 40. Concluded.

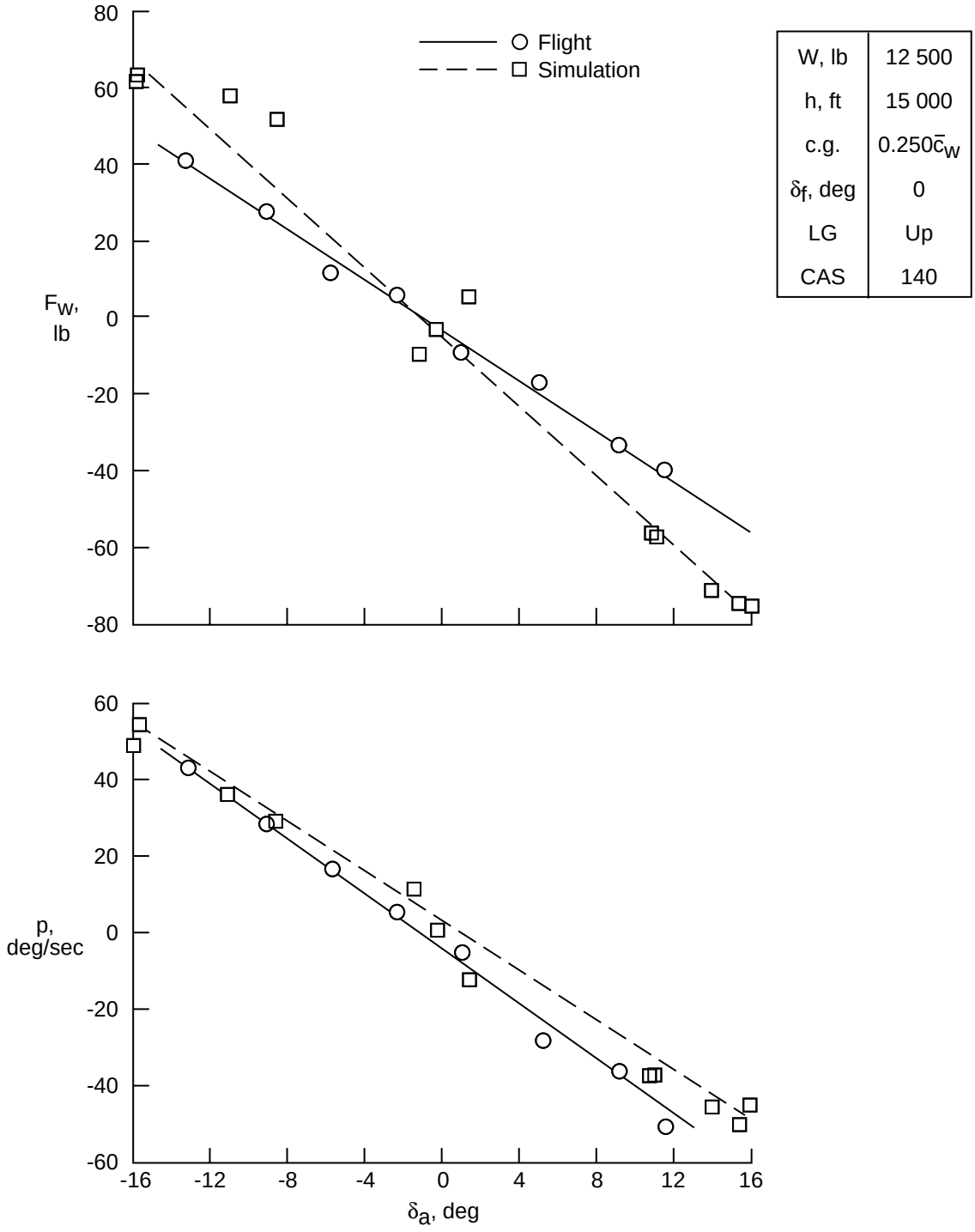

(a) Cruise configuration.

Figure 41. Simulation and flight test data for roll rate and wheel force as a function of aileron deflection; simulation data by pilot G.

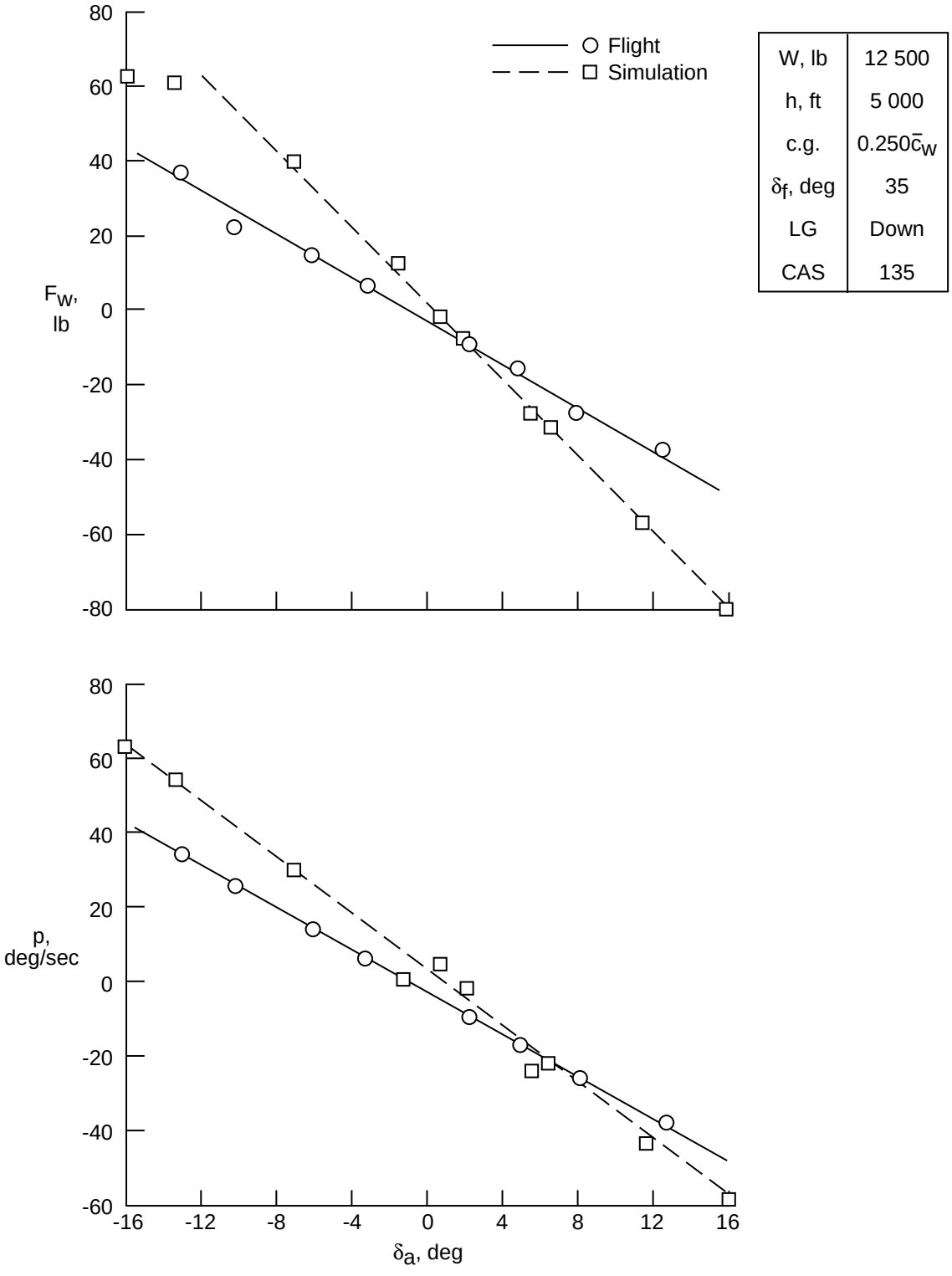

(b) Landing configuration.

Figure 41. Concluded.

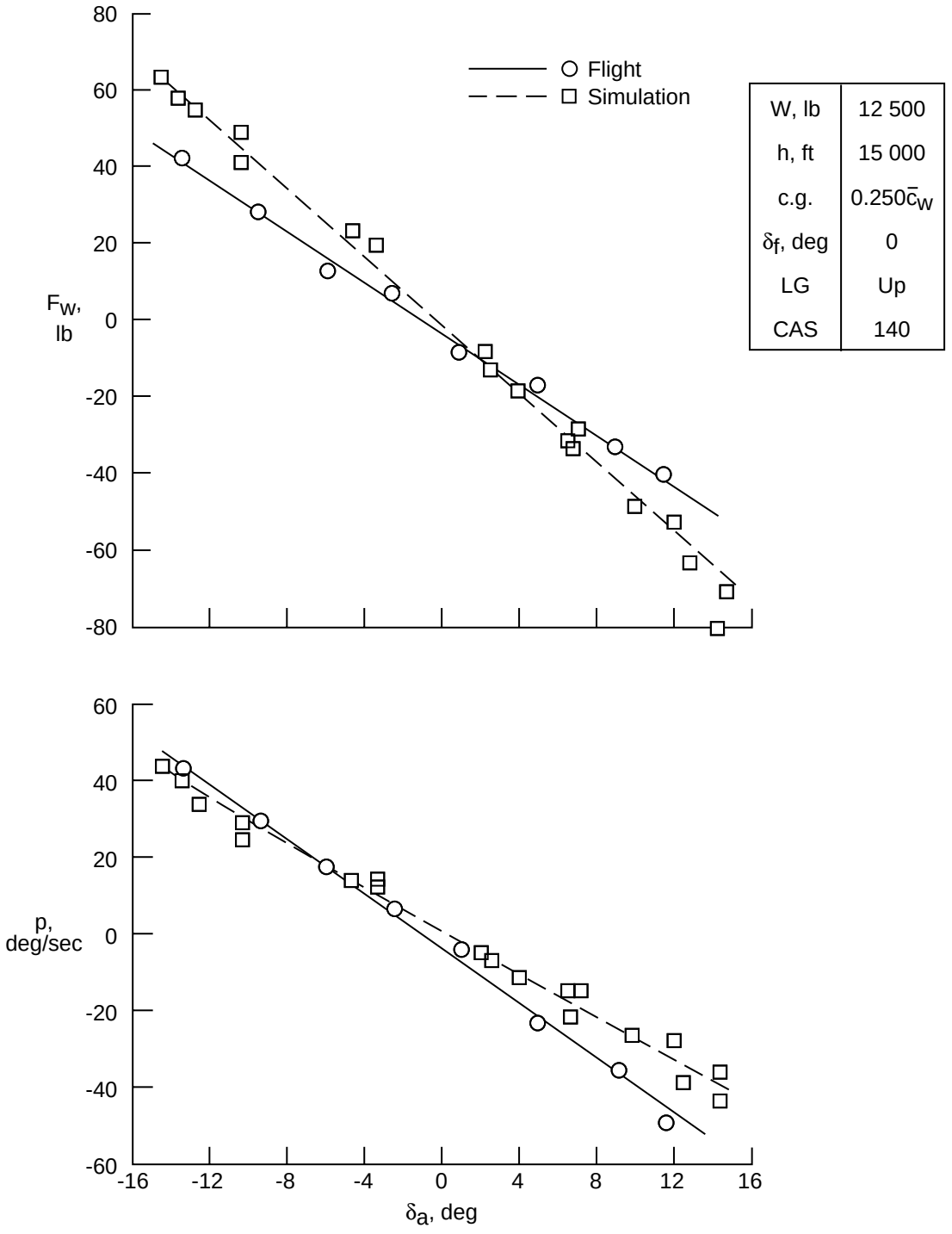

(a) Cruise configuration.

Figure 42. Simulation and flight test data for roll rate and wheel force as a function of aileron deflection; simulation data by pilot B.

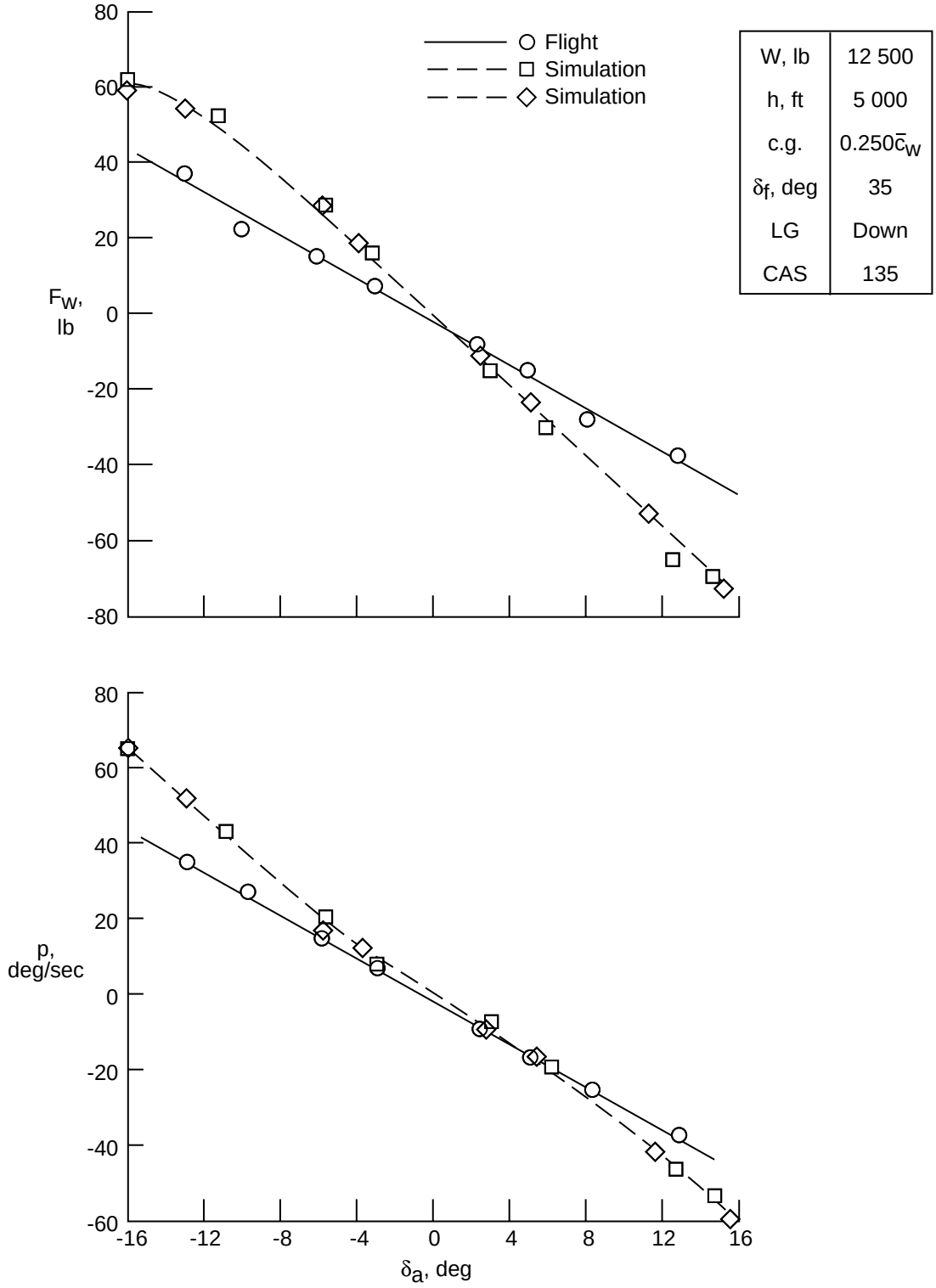

(b) Landing configuration.

Figure 42. Concluded.

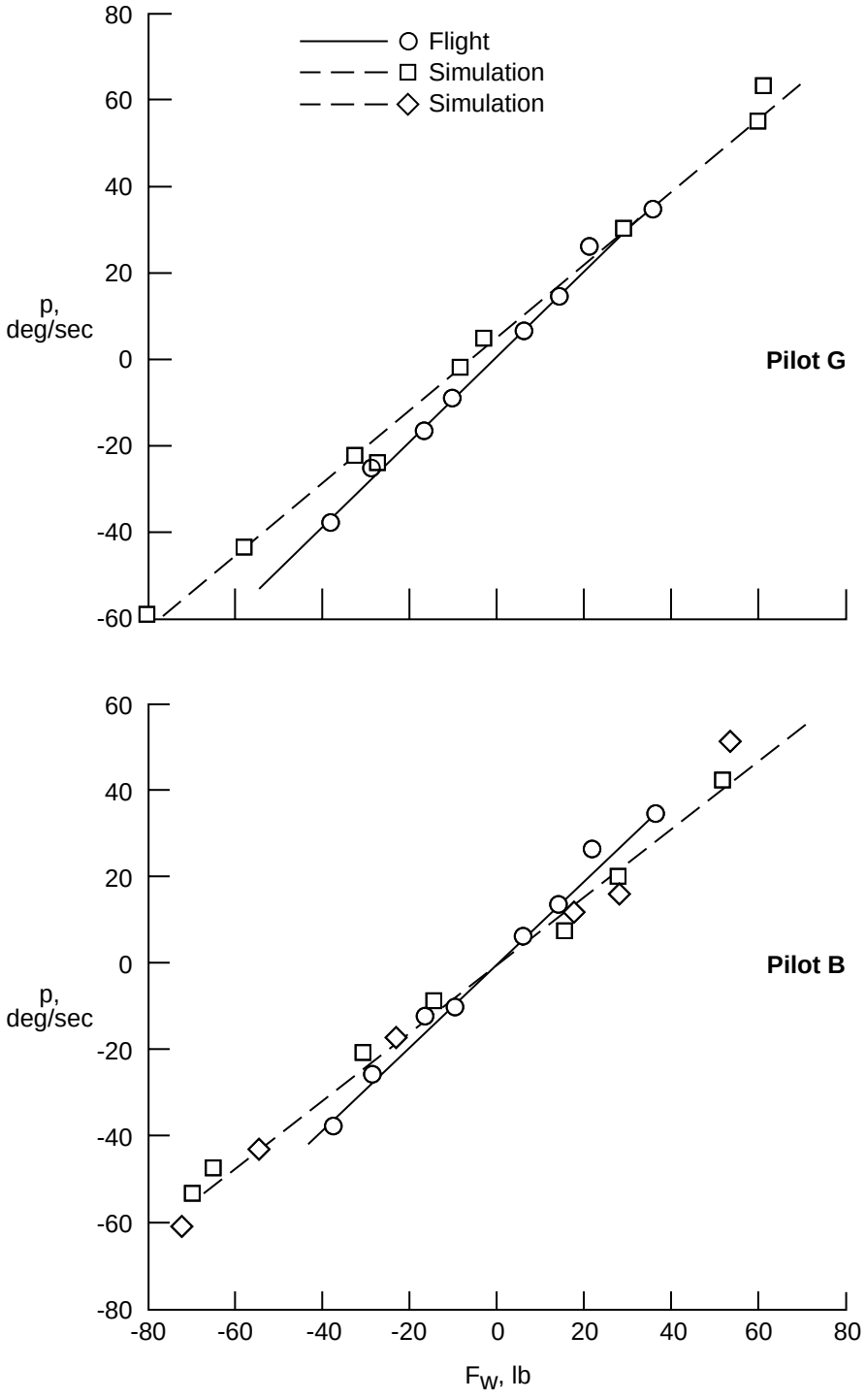

Figure 43. Simulator and flight test data for roll rate as a funtion of wheel force for both subjects with landing configuration.

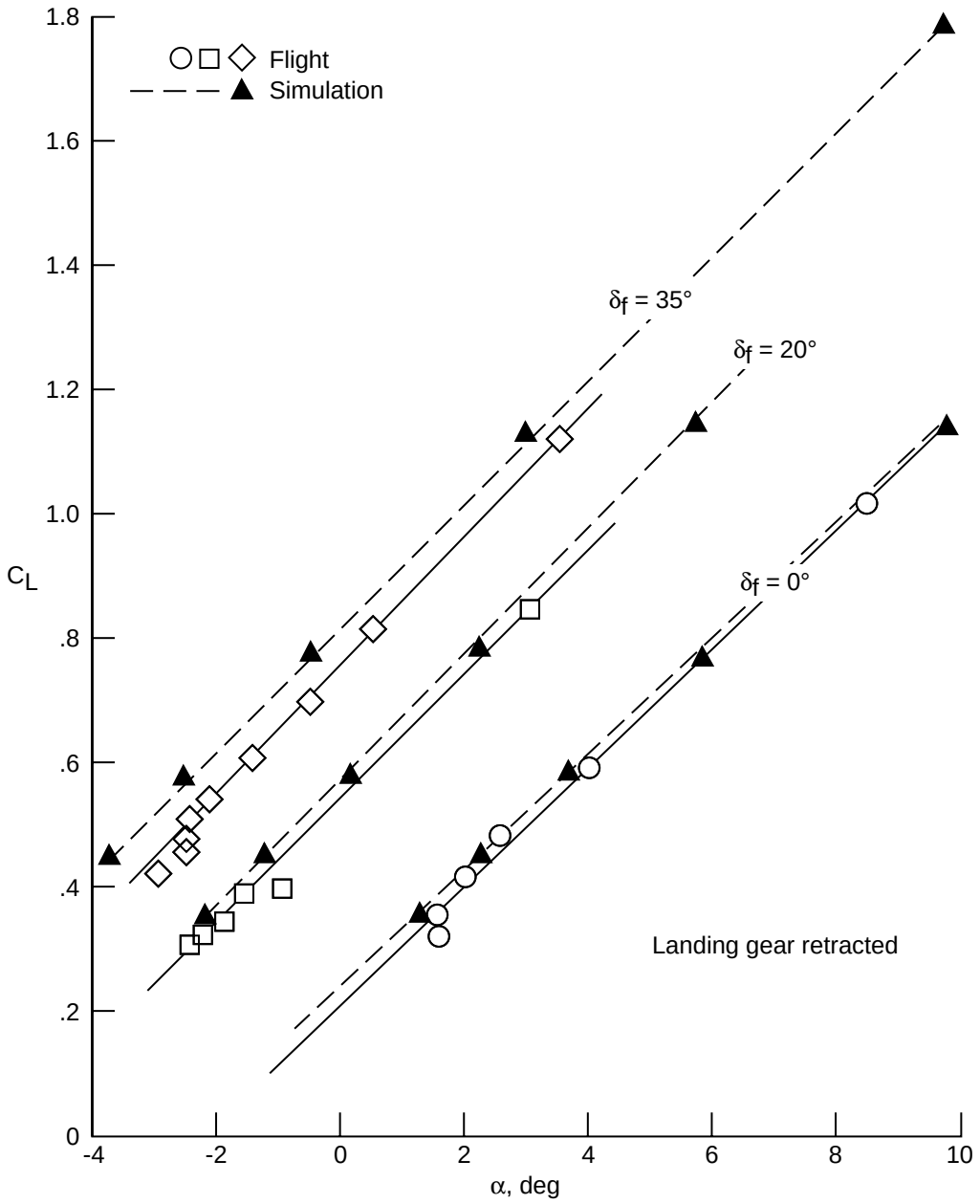

Figure 44. Flight test and simulator trim lift curves for three different flap deflection angles.

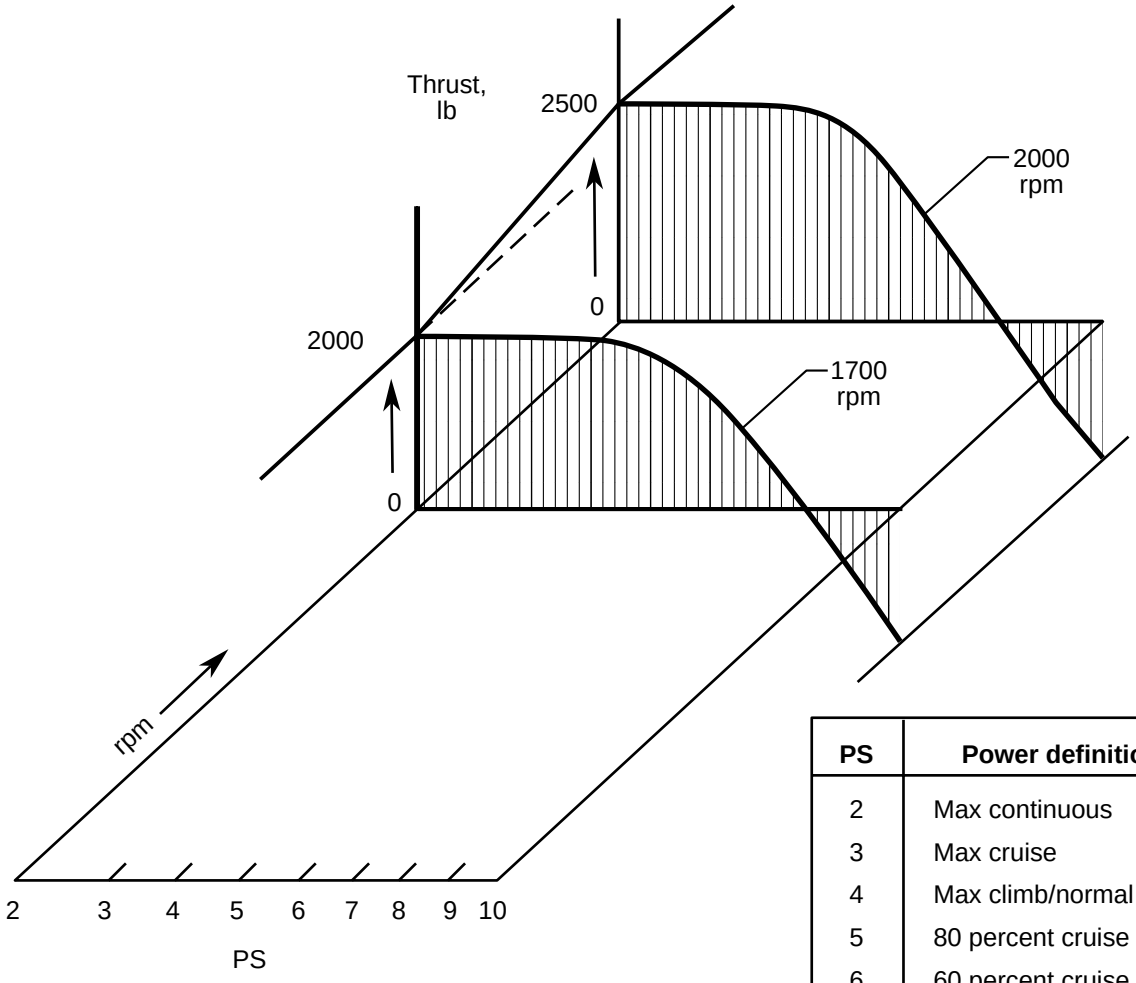

PS	Power definition
2	Max continuous
3	Max cruise
4	Max climb/normal cruise
5	80 percent cruise
6	60 percent cruise
7	40 percent cruise (flight idle)
10	Off

Figure 45. Sketch of thrust variation with power setting at two given rpm values for a single-turbine-engine and propeller combination operating at sea level and low Mach number.

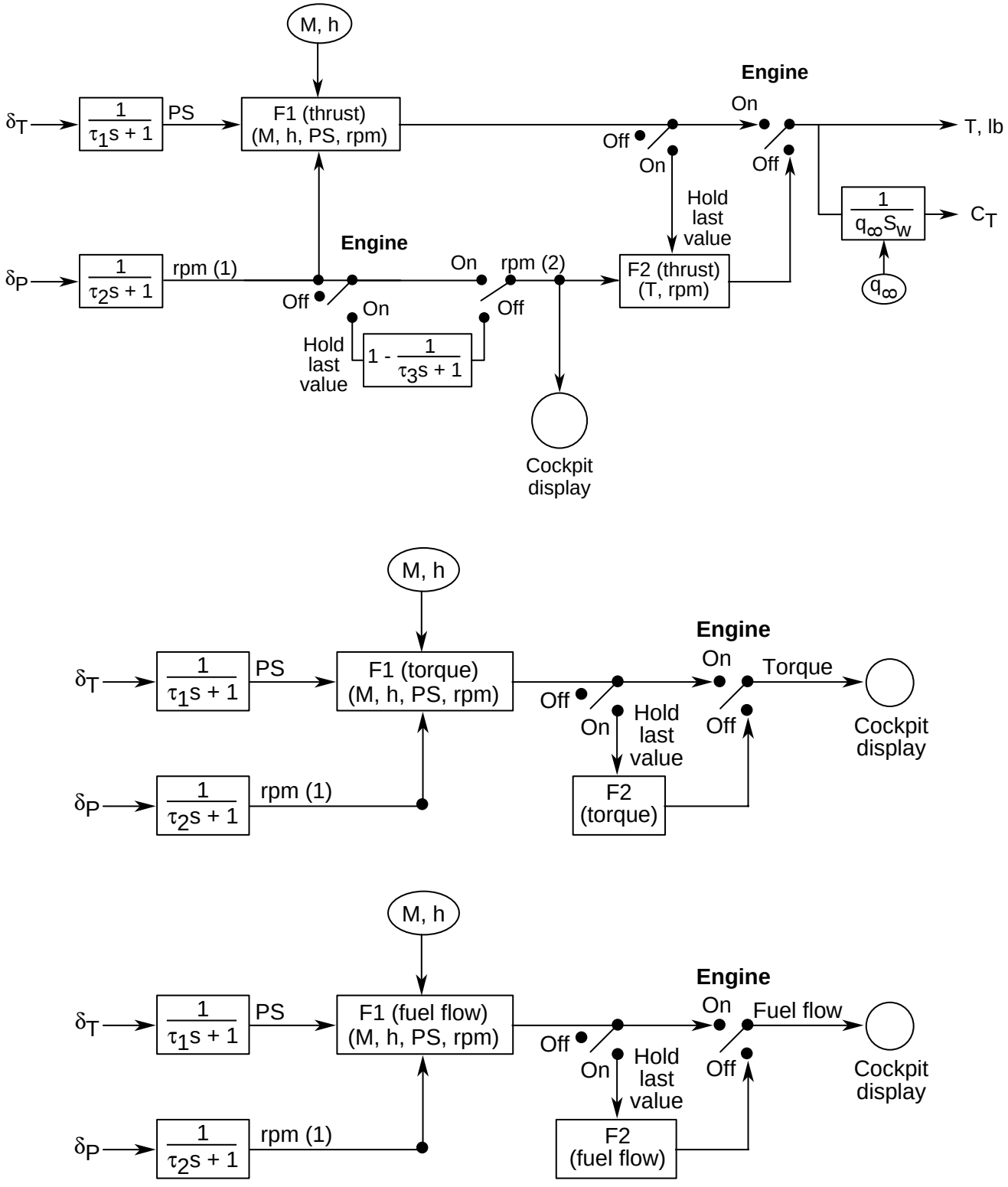

Figure 46. Block diagrams for thrust, torque, and fuel flow for a single power unit.

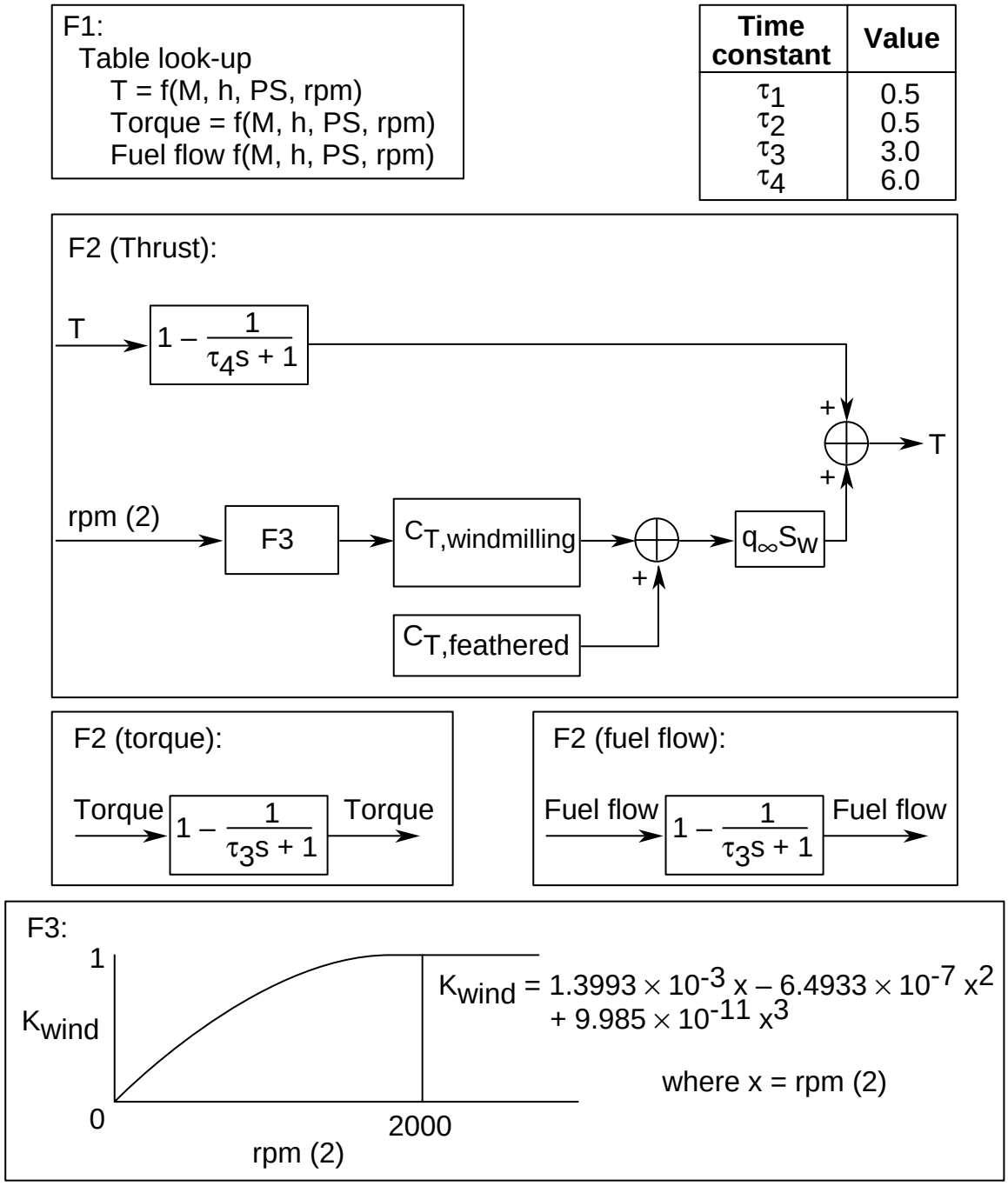

Note: $C_{T,windmilling}$ and $C_{T,feathered}$ are negative numbers

$C_{T,windmilling} = -(C_{D,windmilling} - C_{D,feathered}) = -0.0025$

$C_{T,feathered} = -(C_{D,feathered} - C_{D,prop\ off}) = -0.0050$

Figure 46. Concluded.

Figure 3. Elements of the Langley General Aviation Simulation System.

REPORT DOCUMENTATION PAGE

Form Approved
OMB No. 0704-0188

1. AGENCY USE ONLY *(Leave blank)*	2. REPORT DATE	3. REPORT TYPE AND DATES COVERED
	January 1994	Technical Memorandum

4. TITLE AND SUBTITLE
Piloted Simulation Study of an ILS Approach of a Twin-Pusher Business/Commuter Turboprop Aircraft Configuration

5. FUNDING NUMBERS
WU 535-03-01-03

6. AUTHOR(S)
Donald R. Riley, Jay M. Brandon, and Louis J. Glaab

7. PERFORMING ORGANIZATION NAME(S) AND ADDRESS(ES)
NASA Langley Research Center
Hampton, VA 23681-0001

8. PERFORMING ORGANIZATION REPORT NUMBER
L-17215

9. SPONSORING/MONITORING AGENCY NAME(S) AND ADDRESS(ES)
National Aeronautics and Space Administration
Washington, DC 20546-0001

10. SPONSORING/MONITORING AGENCY REPORT NUMBER
NASA TM-4516

11. SUPPLEMENTARY NOTES
Riley and Brandon: Langley Research Center, Hampton, VA; Glaab: Lockheed Engineering & Sciences Company, Hampton, VA.

12a. DISTRIBUTION/AVAILABILITY STATEMENT
Unclassified–Unlimited

Subject Category 02

12b. DISTRIBUTION CODE

13. ABSTRACT *(Maximum 200 words)*

A six-degree-of-freedom nonlinear simulation of a twin-pusher, turboprop business/commuter aircraft configuration representative of the Cessna ATPTB (Advanced turboprop test bed) was developed for use in piloted studies with the Langley General Aviation Simulator. This paper provides the math models developed, compares simulation predictions with with Cessna flight-test data for validation purposes, and presents results of a handling quality study during simulated ILS (instrument landing system) approaches and missed approaches. Simulated flight trajectories, task performance measures, and pilot evaluations are presented for the ILS approach and missed-approach tasks conducted with the vehicle in the presence of moderate turbulence, varying horizontal winds, and engine-out conditions. Six test subjects consisting of two research pilots, a Cessna test pilot, and three general aviation pilots participated in the study. This effort was undertaken in cooperation with the Cessna Aircraft Company.

14. SUBJECT TERMS	15. NUMBER OF PAGES
Simulation; Aircraft dynamics; Flying qualities; ILS landing approach	119
	16. PRICE CODE: A06

17. SECURITY CLASSIFICATION OF REPORT	18. SECURITY CLASSIFICATION OF THIS PAGE	19. SECURITY CLASSIFICATION OF ABSTRACT	20. LIMITATION OF ABSTRACT
Unclassified	Unclassified		